# Colloidal nanocrystals applied for short-wave infrared photodetectors with fast response

Hengyang Xiang

# Thèse de Doctorat

**Doctoral School Physique et Chimie des Matériaux (ED 397)**

**Laboratoire de Physique et d'Etude des Matériaux (LPEM),**

**ESPCI-ParisTech/CNRS/Sorbonne Université**

# *Colloidal Nanocrystals Applied for Short-Wave Infrared Photodetectors with Fast Response*

**In order to obtain the title of Philosophiae Doctor of Sorbonne Université**

**Specialty: Materials Physics and Chemistry**

**By**

**Hengyang Xiang**

**Directed by Zhuoying Chen and Lionel Aigouy**

**Publically defended on the 19/09/2019 in front of a jury composed by：**

| | | |
|---|---|---|
| Mr Stéphane Holé | President of the jury | Sorbonne Université |
| Mrs María Ujué González | Member of the jury | IMN-CNM, CSIC |
| Mr Christian Bergaud | Reviewer | LAAS-CNRS |
| Mrs Séverine Gomès | Reviewer | CETHIL, INSA de Lyon |
| Mr Lionel Aigouy | Ph.D. Supervisor | LPEM, ESPCI |
| Mrs Zhuoying Chen | Ph.D. Director | LPEM, ESPCI |

# Acknowledgement

First of all, I would like to thank my supervisors Lionel Aigouy and Zhuoying Chen, they gave me very patient guidance on physical optics, chemical synthesis and materials science. All these helped me build a complete scientific research system from basic knowledge to scientific application, which makes my path to science more smooth and interesting. Many thanks to them for their patience and carefulness in all these three years.

I would like to thank the science and technology resources sharing platforms from IPGG, ENS, and Paris 7. Thanks to Olivier Lesage in IPGG for the evaporation. Thanks to Jose Palomo in ENS for his help in photolithography. Thanks to Stephan Suffit in Paris 7 for his help in micro-fabrications. Thanks to Tingting Niu for her great contribution in gold nanorods' synthesis. Thanks to Xiangzhen Xu for her help in the transmission electron microscope (TEM) characterization.

I would like to thank my colleagues, Laurent Billot, Mathilde Schoenauer Sebag, Zhelu Hu, Xiangzhen Xu, Tingting Niu, Hungju Lin, Corentin Paillassard, Chenghao Xin, Sophie Demonchaux, Marie-Claude Theme, Francis Cassagne, Ricardo Lobo and all the others for their help in LPEM.

I would like to thank all the friends in France, Zhenyu Yang, Liqiong Yang, David Becker-Koch, Xiaojiao Yuan and all the other friends for their help.

I would like to thank my family for their support all the time.

I would like to thank all for the time I spent in France.

# Résumé en français

L'infrarouge à ondes courtes (SWIR) désigne généralement les photons dans la plage de longueurs d'onde allant de 1 à 3 microns. Les applications dans cette fenêtre de longueur d'onde exploitent divers avantages tels que la grande longueur de pénétration dans le tissu biologique, la couverture spectrale pour la vision nocturne atmosphérique et l'énergie d'excitation caractéristique de certains modes de vibration moléculaire. Les photodétecteurs SWIR sont donc les composants technologiques essentiels pour la communication optique, la détection de gaz dans l'environnement, le biodiagnostic et la vision nocturne passive. Les technologies SWIR actuelles reposent principalement sur des semi-conducteurs composés à faible bande interdite tels que InGaAs, InSb, PbS et HgCdTe. Alors que les photodétecteurs SWIR classiques présentent une excellente détectivité, ils sont coûteux (en raison de la croissance requise par l'épitaxie) et / ou présentent un risque environnemental car impliquant des éléments hautement toxiques. Par conséquent, des efforts continus de recherche et de développement concernant des systèmes de matériaux alternatifs et des méthodes de fabrication permettant d'élargir le champ d'application de la photodétection SWIR, notamment le phosphore noir (black phosphorus), le graphène, le $MoS_2$, les nanocristaux de PbS colloïdal et les nanostructures plasmoniques.

Les matériaux bidimensionnel, parfois appelés matériaux monocouche, sont des matériaux cristallins constitués d'une seule couche d'atomes. Ces matériaux peuvent trouver des applications dans le domaine du photovoltaïque, les photodétecteurs, les électrodes et la purification de l'eau. Par exemple, le phosphore noir, le graphène et le $MoS_2$ ont démontré un potentiel énorme pour les applications optoélectroniques. Le graphène, en tant que matériau à deux dimensions le plus étudié, a été largement utilisé dans la photodétection à large bande et dans de nombreuses autres applications optoélectroniques.

Les nanocristaux semi-conducteurs colloïdaux tels que le PbS constituent également un excellent choix de matériaux pour la photodétection SWIR à faible coût en raison de leurs avantages en termes de capacité de traitement en solution, d'absorption spectrale ajustable en taille et de compatibilité de substrat flexible. Les dispositifs hybrides, tirant parti à la fois de

la grande mobilité des matériaux bidimensionnels et de la grande section efficace d'absorption des nanocristaux colloïdaux, sont également très prometteurs.

Outre les matériaux semi-conducteurs susmentionnés, les nanostructures plasmoniques à base de métal noble représentent une autre classe de nouveaux matériaux permettant la photodétection SWIR. Les photodétecteurs plasmoniques actuels reposent sur l'extraction de "porteurs chauds" (c'est-à-dire des porteurs hautement énergétiques qui ne sont pas en équilibre thermique avec les atomes de métal) produits lors de la désexcitation des plasmons de surface localisés d'une nanostructure métallique. Sur la base de ce principe, divers photodétecteurs à porteurs chauds ont été fabriqués à l'aide de nanostructures définies par lithographie, présentant une photorésistance allant de quelques nA / W à quelques dizaines de mA / W.

Ces matériaux sont très prometteurs pour le fonctionnement à des fréquences de modulation élevées ou une sensibilité élevée. Cependant, certains inconvénients les éloignent toujours d'une éventuelle commercialisation: processus de production rigoureux (reproductibilité médiocre), non-adaptabilité à la fabrication à l'échelle, préoccupations de sécurité de l'usine (en raison de l'utilisation d'éléments en métaux lourds hautement toxiques). Alternativement, les nanoparticules colloïdales obtenues en solution, telles que les nanobâtonnets d'or colloïdal (Au nanorods) et les nanoparticules onctionnant par up-conversion (UCNP), présentent des caractéristiques intéressantes permettant de surmonter ces inconvénients: capacité de synthèse à l'intensification, capacité de fabrication à faible coût en solution, haute stabilité, faible toxicité biologique et bonne absorption optique des photons SWIR. Cette thèse a pour objectif d'appliquer ces nanoparticules colloïdales à la fabrication de photodétecteurs SWIR et de vérifier leurs possibilités concrêtes dans ce domaine.

Ce manuscrit de thèse est organisé en quatre chapitres. Le premier chapitre est consacré à une introduction générale dans le domaine des technologies de photodétection SWIR, et présente l'état de l'art et la perspective technologique des photodétecteurs SWIR. Deux chapitres sont ensuite consacrés à la présentation des principaux résultats de nos stratégies de photodétection SWIR. Le deuxième chapitre comprend les travaux de synthèse des nanobatonnets d'Au colloïdaux avec des dimensions ajustables (et notamment le rapport longueur/largeur), de l'effet photothermique obtenu sur ces nanobatonnets, ainsi que la fabrication et la caractérisation des photodétecteurs à base de thermistors couplés à des nanobatonnets. Le

troisième chapitre décrit les résultats de la synthèse de nanocristaux de NaYF4: $Er^{3+}$ colloïdaux en solution de taille ajustable, l'architecture de dispositif hybride choisie et la photoréponse de photodétecteurs composés de ces UCNP et de composés organiques hybrides. Le quatrième chapitre est une conclusion de la thèse et décrit quelques perspectives.

Tout d'abord, une série de nanocristaux colloïdaux de taille homogène a été synthétisé au début de mon projet.

1) Au NR: Nous avons synthétisé une série de nanorods d'or colloïdaux de taille homogène et de différents rapports d'aspect (AR) ayant une résonance plasmon longitudinale (LSPR en anglais) ajustable de 900 nm à 1,3 µm. La fabricationa été réalisée en contrôlant la quantité relative de quatre paramètres: nitrate d'argent ($AgNO_3$), grain d'Au, acide chlorhydrique (HCl), oléate de sodium (NaOL). Le processus de préparation détaillé est décrit dans la section expérimentale du chapitre 2.2. Alors que la plupart des NR Au colloïdauxl fabriqués et décrits dans la littérature présentent une LSPR longitudinale (L-LSPR) dans la gamme de longueur d'onde inférieure à 1200 nm, nous avons réussi, en augmentant le rapport longueur/largeur des NR Au jusqu'à 10,96, à observer un pic d'absorption L-LSPR atteignant 1300 nm.

2) UCNPs: Une série de cristaux de $NaYF_4$ colloïdaux de taille homogène et contenant 15% d'$Er^{3+}$ (UCNPs) ont été synthétisé pour la première fois par une voie hydrothermale améliorée. Pour ajuster la taille de ces nanoparticules, différentes quantités molaires de citrate de sodium tribasique dihydraté ont été utilisées pour réagir avec une quantité fixe de $Ln^{3+}$ (contenant 85% de $Y^{3+}$ et 15% de $Er^{3+}$) et de NaF. Le processus de préparation détaillé est décrit dans la section expérimentale du chapitre 3.2. Le reste des paramètres de la synthèse étant identiques, la quantité de citrate de sodium tribasique déshydraté a permis d'ajuster la dimension des particules UCNP de 150 nm à 1000 nm.

De par leur résonance plasmon de surface (SPR), les NR Au ont un effet photothermique important, qui peut être appliqué à la détection optique et au domaine biomédical. Ainsi, de nombreuses recherches sur les propriétés photothermiques et optoélectroniques de nanostructures d'Au ont été réalisées ces dernières années. Cependant, il y a encore peu d'expériences sur l'analyse quantitative de la capacité de nano-chauffage d'un seul NR, en particulier sur les NR à rapport d'aspect élevé, même s'il a déjà été établi que ce type de NR possède des propriétés photothermiques intéressantes. Ainsi, dans ce travail, une étude de l'augmentation de la température des Au NR excités à 1,537 µm est présentée pour prouver

que l'effet photothermique des Au NR est très efficace. Nous montrerons que quelques NR peuvent produire une augmentation de température locale de plusieurs dizaines de degrés, ce qui en fait des nanostructures chauffantes très efficaces dans cette plage de longueurs d'onde. L'élévation de la température est mesurée en utilisant un nanocristal (NC) de $NaYF_4$ dopé par $Er^{3+}$ fluorescent unique comme nanothermomètre. Un aspect intéressant de cette configuration est que le laser proche infrarouge (NIR) utilisé pour chauffer les NR d'Au est le même que celui qui excite la fluorescence des ions $Er^{3+}$. Ce mode de fonctionnement très simple fait de la combinaison Au-NRs / $NaYF_4$: $Er^{3+}$ NC un dispositif de chauffage / capteur de température très puissant et polyvalent. Une simulation numérique de l'élévation de la température par l'effet photothermique de Au NR a été réalisée. Il confirme l'existence d'une élévation de température et prédit néanmoins un effet plus important que ce qui est mesuré. Ceci est du au fait que nous ne connaissons pas vraiment la section efficace d'absorption des nanorods déposés sur une surface, notamment lorsqu'ils peuvent être en intéraction comme c'est le cas de nitre étude. Des calculs plus rigoureux prenant en compte les effets de couplages devraient être pris en compte, mais ce type de calcul dépasse les limites de cette étude.

L'effet photothermique des Au NR étant efficace, un dispositif hybride, composée de nanobatonnets d'Au déposés à la surface d'un thermistor NTC, a été proposé comme approche alternative à faible coût pour la détection dans le spectre SWIR. Sous une illumination monochromatique d'intensité relativement faible (< 1 mW / $cm^2$), les dispositifs hybrides Au-NRs / thermistances présentent une photoréponse très nette sous la forme d'une chute de résistance photo-induite dans la fenêtre de longueur d'onde de 1,0 µm à 1,8 µm. Cela contraste avec le dispositif de contrôle (thermistance seule sans Au NR), dont la photoréponse est négligeable dans les mêmes conditions d'éclairage. La photosensibilité du dispositif hybride atteint une valeur maximale de $2,06\times10^7$ Ω / W à 1,3 µm, longueur d'onde conforme au maximum L-LSPR des NR Au appliqués. Pour des intensités d'éclairements supérieures (de 6,7 mW / $cm^2$ à 4464,3 mW / $cm^2$) obtenues par un laser (λ = 1,5 µm) focalisé sur le dispositif, en raison de la photoréponse chauffante induite par le laser, tant dans le dispositif témoin que dans le dispositif hybride. Néanmoins, dans ce cas, les dispositifs hybrides ont présenté une amélioration de la photoréactivité plus de 5 fois supérieure à celle du dispositif de contrôle. Ainsi, ces résultats suggèrent que l'effet photothermique induit par l'absorption de Au NRs (i) active la capacité de détection dans une structure hybride Au-NRs / thermistance sous un éclairement relativement faible et (ii) amplifie la photo-réponse du dispositif hybride lorsque l'intensité d'éclairementest élevée. Le temps de réponse du

dispositif hybride Au-NRs / thermistance est aussi court que 2 secondes, et est limité par le temps de réponse du thermistor lui-même. La détection optique dans le spectre SWIR est une tâche ardue. L'approche actuelle qui exploite l'effet photothermique des Au NR colloïdaux obtenus en solution représente donc une nouvelle voie vers la détection SWIR à faible coût.

Pour améliorer la vitesse de réponse de ces photodétecteurs SWIR à base de Au-NRs, nous avons ensuite proposé une nouvelle structure de photodétecteur SWIR hybride basée sur le couplage entre un micro-fil résistif en platine (Pt) et des Au NR plasmoniques colloïdaux. Le but est de réduire le temps de réponse photoélectrique aux quatre ordres de grandeur par rapport à nos travaux antérieurs sur les thermistors. Le Pt a été choisi ici en raison de la forte dépendence en température de sa résistivité (coefficient thermique élevé), de sa plage de température de fonctionnement étendue, de sa stabilité élevée et de sa répétabilité. La combinaison de ces caractéristiques a conduit aux nombreuses applications du Pt en tant que détecteur résistif de température (RTD). Ici, une série de micro-fils de Pt de différentes dimensions a été fabriquée et utilisée pour mesurer l'effet photothermique de nanobatonnets d'Au dans un dispositif hybride Au-NRs / Pt. Dans un photodétecteur Au-NRs / Pt optimisé, nous avons mesuré un temps de réponse de 97 µs sous l'éclairement d'un laser $\lambda$ = 1,5 µm avec son ON / OFF modulé à 120 Hz. Nous avons aussi observé que, même à une fréquence de modulation de 50 kHz, de tels photodétecteurs Au-NRs / Pt sont toujours capables de générer une commutation de photorérésistive claire. Ces photodétecteurs hybrides Au-NRs / Pt, capables de convertir rapidement les photons SWIR, la chaleur et la résistance à une fréquence pouvant atteindre plusieurs dizaines de kHz, constituent donc une stratégie totalement nouvelle pour les alternatives de photodétection SWIR, répondant aux besoins des technologies émergentes, ces applications exigeant un coût de fabrication réduit et une vitesse de fonctionnement élevée.

Une autre stratégie possible pour la photodétection SWIR consiste à utiliserle phénomène d'upconversion, phénomène permettant de convertir les photons à basse énergie en des photons à haute énergie. Divers systèmes de nanoparticules colloïdales possédant des propriétés d'up-conversion (NP) ont été synthétisés, principalement basés sur le dopage de cations de lanthanides trivalents dans des hôtes à faible énergie de phonons et fonctionnant par up-conversion par un mécanisme à deux ou plusieurs photons. Depuis lors, ils ont été appliqués dans de nombreuses applications, notamment l'ingénierie biomédicale, la détection thermique, la récupération d'énergie solaire et la photodétection. En fait, la plupart de ces

applications utilisat l'up-conversion de photons est basée sur des systèmes co-dopés $Yb^{3+}$ et $Er^{3+}$ capables de convertir vers le haut la lumière proche infrarouge avec une longueur d'onde maximale de 1,0 µm (par exemple en excitant à 808 nm ou 975 nm et en émettant des photons visibles à 540 nm). Les systèmes capables de convertir en amont les photons SWIR restent rares. Dans ce travail, par une architecture de photodiodes, nous proposons des photodétecteurs flexibles hautes performances, exempts de métaux lourds et sensibles aux photons $\lambda$ = 1,5 µm, basés sur la formation d'un hybride organique / inorganique et composé de polymère conjugué / petite molécule avec des nanoparticules dopées au $Er^{3+}$ (UCNP). Une série de nanocrsitaux de $NaYF_4$ inorganiques colloïdaux de taille homogène, dopés $Er^{3+}$ et de différentes dimensions ont été synthétisées par des voies hydrothermales, permettant une conversion efficace de photons $\lambda$ = 1,5 µm en photons visibles. Un hôte organique contenant un mélange de copolymère à base de dicétopyrrolopyrrole (DPP) et d'ester méthylique d'acide [6,6]-phényl-C71-butyrique ($PC_{70}BM$) a été utilisé. Cet hôte organique présente une forte absorption optique couvrant les spectres visibles et proches infrarouges jusqu'à $\lambda$ = 1 µm et est ainsi capable de récolter efficacement la plupart des photons visibles convertis en amont par les nanoparticules. Sous éclairement par des photons SWIR $\lambda$ = 1,5 µm, les photodétecteurs hybrides BHJ / UCNP présentent une photoréactivité de 0,73 mA / W et 0,44 mA / W pour les dispositifs élaborés sur des substrats en verre et sur des substrats souples en polyéthylène téréphtalate (PET), respectivement. De manière remarquable, une vitesse de fonctionnement rapide caractérisée par un temps de montée du photocourant égal à 80 µs a été observée sous l'illumination de photons $\lambda$ = 1,5 µm, ce qui est plus rapide de plus d'un ordre de grandeur par rapport aux précédentes études sur des photodétecteurs utilisant des systèmes à dopage $Er^{3+}$. Cette valeur est aussi et de deux à quatre ordres meilleures que la plupart des autres photodétecteurs à semi-conducteur non-avalanche à des longueurs d'onde SWIR. Présentant des avantages tels que l'adaptabilité aux substrats flexibles, la capacité de fabrication en solution, l'absence de métaux lourds toxiques et des performances supérieures, les photodétecteurs hybrides organique / inorganique développés dans ce travail peuvent constituer un concurrent sérieux pour la prochaine génération à faible coût et à haute performance photodétecteurs SWIR.

En résumé, dans cette thèse, nous avons présenté deux approches alternatives pour les capteurs SWIR, toutes deux reposant sur les nanocristaux colloïdaux fabriqués en solution. Quelques photodétecteurs SWIR (Au-NRs / Thermistance, photodétecteur Au-NRs / Pt et photodétecteur UCNPs / organique) ont été développés dans mon travail, montrant une

sensibilité élevée. De plus, la préparation est un processus peu coûteux et évolutif permettant une fabrication en série à la fois au niveau de la synthèse des matériaux et de la fabrication des dispositifs eux-mêmes.

Mots clés: infrarouge à ondes courtes, nanocristaux colloïdaux, nanoparticules plasmoniques, effet photothermique, photodétecteurs à base des materiaux hybrides

# English abstract

Short-wave infrared (SWIR) typically refers to the photons in the wavelength range from 1 to 3 microns. Applications in this wavelength window exploit various advantages such as long penetration length in biological tissue, spectral coverage of the atmospheric nightglow, and the characteristic excitation energy of certain molecular vibration modes. SWIR photodetectors are thus the key technological components to achieve optical communication, environmental gas sensing, biodiagnostics and passive night vision. Current SWIR technologies mainly rely on low-bandgap compound semiconductors such as InGaAs, InSb, PbS and HgCdTe. While classical SWIR photodetectors exhibit excellent detectivity, they are costly (due to epitaxial growth requirement) and/or environment unfriendly involving highly toxic heavy metal elements. There are therefore continuous research and development efforts for alternative material systems and fabrication methods to expand the scope of applications of SWIR photodetection, including black phosphorus, graphene, $MoS_2$, colloidal PbS nanocrystals and plasmonic nanostructures.

2-dimensional materials, sometimes referred to as single layer materials, are crystalline materials consisting of a single layer of atoms. These materials can find applications in photovoltaics, photodetectors, electrodes and water purification. For example, black Phosphorus, graphene and $MoS_2$, have been demonstrated tremendous potential for optoelectronic applications. Graphene, as a most extensively investigated two-dimensional material, has been widely used in broadband photodetection and many other optoelectronic applications.

Colloidal semiconducting nanocrystals such as PbS are also excellent material choices towards low-cost SWIR photodetection owing to their advantages in solution-processability, size-tunable spectral absorption and flexible substrate compatibility. Hybrid devices, taking advantage of both the high carrier mobility of two-dimensional materials and the large absorption cross-section of colloidal nanocrystals, are also highly promising.

Besides the above-mentioned semiconducting materials, plasmonic nanostructures based on noble metal represent another class of new materials to enable SWIR photodetection. Current plasmonic photodetectors rely on the extraction of "hot carriers" (*i.e.* highly energetic carriers not in thermal equilibrium with the metal atoms) produced during the decay of the localized surface plasmons from a metal nanostructure. Based on this principle various hot-carrier photodetectors were fabricated by lithographically defined nanostructures exhibiting photoresponsivity ranging from a few nA/W to a few tens of mA/W.

These materials show great promise in terms of operation at high modulation frequencies or high sensitivity. But some disadvantages still keep them away from the market: rigorous production process (poor reproducibility), non-adaptability to scale-up fabrication, manufactory safety and security concerns (due to the use of highly toxic heavy metal elements). Alternatively, solution-processed colloidal nanoparticles, such as colloidal gold nanorods (Au NRs) and upconversion nanoparticles (UCNPs), exhibit interesting characteristics possible to overcome these disadvantages: capability of scaling-up synthesis, solution-processability adaptable to low-cost fabrication, high stability, low biological toxicity, and good optical absorption for SWIR photons. This PhD thesis aims to apply these colloidal nanoparticles to fabricate SWIR photodetectors and verifies their possibilities for new generation of photodetection.

The organization of this thesis is as follows: In total four chapters will be presented in this thesis. The first chapter focused on a general introduction in the field of SWIR photodetection technologies, and the state-of-the-art and the technological prospect of SWIR photodetectors. Afterwards, two chapters are dedicated to present the main results from our strategies of SWIR photodetection. The second chapter includes the synthesis work of aspect-ratio-tunable colloidal Au NRs, and photothermal effect of Au NRs, and the fabrication and measurement of Au NRs/NTC-thermistor photodetector and Au-NRs/Pt photodetectors. The third chapter includes results from the synthesis of size-tunable solution-processed colloidal $NaYF_4:Er^{3+}$ nanocrystals, the hybrid device architecture chosen and the photoresponse of hybrid UCNPs/organic photodetectors. The fourth chapter is the conclusion and perspectives of my thesis.

First of all, a series of monodisperse colloidal nanocrystals were synthesized at the beginning of my project.

1) Au NRs: We synthesized a series of monodisperse colloidal gold nanorods of different aspect-ratios (ARs) with their longitudinal LSPR maximum tunable from 900 nm to 1.3 μm. The synthetic tuning was achieved by controlling the amount of four parameters: silver nitrate ($AgNO_3$), Au seeds, hydrochloric acid (HCl), sodium oleate (NaOL). Detailed preparation process is described in the experimental section of chapter 2.2. While most reported colloidal Au NRs exhibit a longitudinal LSPR (L-LSPR) in the wavelength range shorter than 1200 nm, we successfully extend the aspect-ratio (AR) of Au NRs up to 10.96 with their L-LSPR absorption peak reaching 1300 nm.

2) UCNPs: A series of monodisperse colloidal $NaYF_4$:15%$Er^{3+}$ UCNPs were first synthesized by an improved hydrothermal route. To adjust the size of the upconversion nanoparticles, different molar amounts of sodium citrate tribasic dihydrate were used to react with a fixed amount of $Ln^{3+}$ (containing 85% $Y^{3+}$ and 15% $Er^{3+}$) and NaF. Detailed preparation process is described in the experimental section of chapter 3.2. With the rest of the synthetic parameters being identical, the amount of sodium citrate tribasic dehydrate allowed a tuning the UCNP particle dimension from 150 nm to 1000 nm.

Benefiting by their surface plasmon resonance (SPR), Au NRs have a significant photothermal effect, which can be applied into optical sensing and biomedical field. For this reason, the researches on the Au NRs' photothermal and optoelectronic properties have been popping up in recent years. However, there are still few experiments on the quantitative analysis of a single Au NR's nano-heating capacity, especially on the high aspect-ratio Au NRs, even though Au NRs have been determined to have good surface plasmon resonance (SPR) and photothermal properties. Thus, in this work, a study of the temperature increase of Au NRs excited at 1.537 μm is presented to prove that the photothermal effect from Au NRs is high-efficiency. We will show that a few NRs can produce a local temperature increase of several tens of degrees, making them very efficient heaters in this wavelength range. The temperature elevation is measured via using a single fluorescent $Er^{3+}$-doped $NaYF_4$ nanocrystal (NC) as a nanothermometer. An interesting aspect of this configuration is that the SWIR laser used for heating the Au NRs is the same than the one that excites the fluorescence of $Er^{3+}$ ions. This very simple mode of operation makes the combination Au-NRs/$NaYF_4$:$Er^{3+}$ NC a very powerful and versatile heater/temperature sensor. Numerical simulation of temperature elevation by the photothermal effect of Au NRs was performed. It confirms the existence of temperature elevation but predicts a larger effect than what is measured, possibly duo to the fact that these models do not account for near- field coupling effects.

Since the photothermal effect of Au NRs is efficient, a hybrid device structure, composing of Au NRs on the surface of a NTC-thermistor, was proposed as an alternative low-cost approach for sensing in the SWIR spectrum. Under a monochromatic illumination of relatively low intensity (< 1 mW/cm$^2$), hybrid Au-NRs/thermistor devices exhibit a clear photoresponse in the form of photo-induced resistance drop in the wavelength window from 1.0 μm to 1.8 μm. This is in contrast to the control device (thermistor alone without Au NRs), the photoresponse of which is negligible under the same illumination condition. The photo-responsivity of the hybrid device reaches a maximum value of $2.06\times10^7$ Ω/W at 1.3 μm, a wavelength in agreement with the L-LSPR maximum of the Au NRs applied. At higher illumination intensities (from 6.7 mW/cm$^2$ to 4464.3 mW/cm$^2$) achieved by a laser (λ = 1.5 μm) focused onto device, due to the laser-induced heating photoresponse was observed in both the control and the hybrid device. Nevertheless, in this case hybrid devices exhibited more than 5-fold enhancement of photoresponsivity by comparison to the control device. Thus, these results suggest that the plasmonic-induced photothermal effect of Au NRs (i) enables the photo-sensing capability in a hybrid Au-NRs/thermistor device structure under relatively weak illumination and (ii) boost the photo-response of the hybrid device when illumination intensity is high. The response speed of the current Au-NRs/thermistor hybrid device is as short as 2 seconds, limited by the response speed of the thermistor itself. Optical sensing in the SWIR spectrum is a challenging task, the current approach harvesting the photothermal effect of solution-processed colloidal Au NRs thus represents a new path towards alternative and low-cost SWIR sensing.

To improve the response speed of these Au-NRs-based SWIR photodetectors, we propose a new hybrid SWIR photodetector structure based on the coupling between a resistive platinum (Pt) microwire and colloidal plasmonic Au NRs which is capable to reduce the photoresponse time of more than *four orders of magnitudes* compared to our previous work. Pt was chosen here due to its large temperature coefficient of resistance, wide operation temperature range, and high stability. The combination of these characteristics has led to the extensive applications of Pt as a resistance temperature detector (RTD). Here a series of Pt microwires of various dimensions were fabricated and applied to harvest the photothermal effect of Au NRs in an Au-NRs/Pt hybrid device structure. In an optimized Au-NRs/Pt photodetector, we measured a response time of 97 μs under the illumination of a λ=1.5 μm laser with its

ON/OFF modulated at 120 Hz. In particular, even at an illumination modulation frequency of 50 kHz, such Au-NRs/Pt photodetectors are still capable to generate clear photoresponse switching. These hybrid Au-NRs/Pt photodetectors, able to provide a fast conversion between SWIR photons, heat, and resistance change at a frequency up to tens of kHz, thus represent a brand-new strategy for SWIR photodetection alternatives, meeting the needs of emerging applications demanding reduced fabrication cost and high operation speed.

One other possible strategy for SWIR photodetection is to apply photon upconversion, a phenomenon to convert low energy photons into high energy ones. Various upconversion systems in the form of solution-processed nanoparticles (NPs) have been synthesized, mostly based on the doping of trivalent lanthanide cations in a low phonon energy hosts and performing upconversion through a two- or multi-photon mechanism. Since then they have been applied into many applications including biomedical engineering, thermal sensing, solar energy harvest, and photodetection. Indeed, most of these photon upconversion applications are based on $Yb^{3+}$ and $Er^{3+}$ co-doped systems capable to upconvert near-infrared light with a wavelength maximum no larger than 1.0 μm (e.g. upconversion from 808 nm or 975 nm to visible photons). Material systems able to upconvert SWIR photons remain rare. In this work, by a photodiode device architecture, we propose high-performance heavy-metal-free flexible photodetectors sensitive to $\lambda$ = 1.5 μm photons based on the formation of a solution-processed organic/inorganic hybrid composing of conjugated polymer/small molecule bulk-heterojunctions (BHJs, host) together with $Er^{3+}$-doped upconversion nanoparticles (UCNPs, guest). A series of monodisperse colloidal inorganic $NaYF_4:Er^{3+}$ UCNPs of various dimensions were synthesized by hydrothermal routes, providing effective upconversion of $\lambda$ = 1.5 μm photons to visible ones. An organic host was applied containing a donor-accepter BHJ blend of diketopyrrolopyrrole (DPP)-based copolymer and [6,6]-phenyl-$C_{71}$-butyric acid methyl ester ($PC_{70}BM$). Such organic host exhibits strong optical absorption covering the visible and near-infrared spectrum up to $\lambda \approx 1$ μm and is thus capable to efficiently harvest most visible photons upconverted by the guest nanoparticles. Under the illumination of $\lambda$ = 1.5 μm SWIR photons, optimized hybrid BHJ/UCNP photodetectors exhibit a clear photoresponsivity of 0.73 mA/W and 0.44 mA/W for devices built on rigid glass substrates and flexible polyethylene terephthalate (PET) substrates, respectively. Remarkably, a fast operation speed characterized by a short photocurrent rise time down to 80 μs was observed under the illumination of $\lambda \approx 1.5$ μm photons, which is faster by more than one order of

magnitude than previous photodetector studies applying $Er^{3+}$-doped upconversion systems, and by two to four orders than most other nonavalanche semiconductor photodetectors at SWIR wavelengths. Exhibiting advantages such as adaptability to flexible substrates, processability in solution, absence of highly toxic heavy metals, and superior performance, the hybrid organic/inorganic photodetectors developed in this work can be a bright contender for next-generation low-cost and high-performance SWIR photodetectors.

In a brief summary, in this thesis we reported two alternative approaches for SWIR sensors both of which rely on the solution-processed colloidal nanocrystals. A few SWIR photodetectors (Au-NRs/Thermistor, Au-NRs/Pt photodetector and UCNPs/organic photodetector) were developed in my work, showing high responsivity and sensitivity. In addition, the preparation of these devices is a low-cost and scalable up to mass production process both in the material synthesis and device fabrication. These results along with their characters of solution-process and absence of toxic heavy metal elements make these hybrid photodetectors promising candidates for new strategies towards a low-cost and wearable SWIR photodetection without the use of highly toxic heavy metal elements.

Keywords: short-wave infrared, colloidal nanocrystals, plasmonic nanoparticles, photothermal effect, hybrid photodetectors

# Table of Contents

1. Introduction ..... 1

2. Au NRs for SWIR photodetectors ..... 14

2.1 Introduction of Au NRs ..... 14

2.2 Experimental section ..... 17

2.2.1 Synthesis of colloidal Au NRs ..... 17

2.2.2 Synthesis of $NaYF_4:Er^{3+}$ fluorescent nanocrystals ..... 17

2.2.3 Fabrication and measurement of Au-NRs/Thermistor ..... 18

2.2.4 Fabrication and measurement of Au-NRs/Pt device ..... 19

2.2.5 Characterization for materials ..... 20

2.3 Results and discussion ..... 21

2.3.1 Aspect-ratio tunability of colloidal Au NRs ..... 21

2.3.2 Photothermal effect of Au NRs ..... 25

2.3.3 Au NRs/NTC-thermistor photodetector ..... 40

2.3.4 Au-NRs/Pt photodetector ..... 48

2.4 Summary ..... 61

3. $NaYF_4:Er^{3+}$ for flexible SWIR photodetectors ..... 62

3.1 Introduction of upconversion nanoparticle ..... 62

3.2 Experimental section ..... 64

3.2.1 Synthesis of $NaYF_4:Er^{3+}$ UCNPs with tunable sizes ..... 64

3.2.2 Synthesis of ZnO nanoparticles ..... 65

3.2.3 Device preparation and characterization ..... 65

3.2.4 Structural and optical characterizations ..... 66

3.3 Results and discussion ..... 67
3.3.1 Size-tunability of $NaYF_4:Er^{3+}$ ..... 68
3.3.2 Optical property of UCNPs and UCNP-organic hybrids ..... 70
3.3.3 Device architecture and photoresponse performance ..... 73
3.3.4 Comparison with other SWIR photodetectors ..... 79
3.3.5 Mechanical bending tests on flexible hybrid devices ..... 81
3.4 Summary ..... 82
4. Conclusion and perspectives ..... 83
5. Annex ..... 85
5.1 Annex I. supporting information for Au-NRs/thermistor ..... 85
5.2 Annex II. Supporting information for Au-NRs/Pt device ..... 89
5.3 Annex III. Supporting information for UCNPs/Polymer device ..... 96
6. Publications ..... 101
7. References ..... 102

# 1. Introduction

Short-wave infrared (SWIR) typically refers to the photons in the wavelength range from 1 to 3 microns. Applications in this wavelength window exploit various advantages such as long penetration length in biological tissue, spectral coverage of the atmospheric nightglow, and the characteristic excitation energy of certain molecular vibration modes.[1–3] SWIR photodetector are thus the key technological component to achieve optical communication, environmental gas sensing, biodiagnostics and passive night vision.[4]

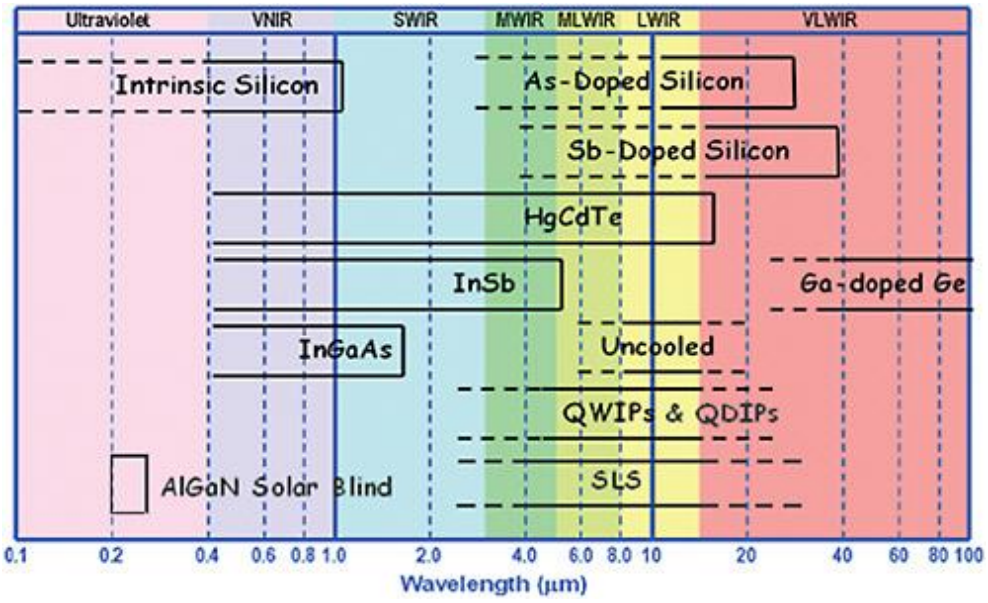


**Figure 1.1** *List of materials used to detect the ultraviolet-visible-infrared light (UV-Vis-IR). [Ref. 5]*

Current SWIR technologies mainly rely on low-bandgap compound semiconductors such as Indium Gallium Arsenide (InGaAs), Indium antimonide (InSb), and Mercury Cadmium Telluride (HgCdTe). Here, a summary of the materials used to detect the ultraviolet-visible-infrared light (UV-Vis-IR), is shown in **Figure 1.1**.[5] From this picture, we can see that all these detectors can cover mostly the entire spectrum from 0.1 μm to 100 μm. But only silicon (Si) photodetector is cheap one, the detectors beyond the visible spectrum are

costly due to epitaxial growth requirement and/or environment unfriendly involving highly toxic heavy metal elements. For instance, InGaAs is an expensive material because of its epitaxial growth requirement. Therefore making an InGaAs photodetector costs an exorbitant amount of money and is limited only to niche low-volume, high-value applications. Owing to these practical reasons, great efforts are being made continuously to search for suitable materials to replace these expensive materials and toxic metal elements. Many new materials have sprung up in recent years, such as two-dimensional (2D) materials,[6–11] colloidal lead sulfide (PbS) [12,13] and plasmonic nanostructures.[14]

2D Materials, sometimes referred to as single layer materials, are crystalline materials consisting of a single layer of atoms. They can provide very high carrier mobilities, nearly atomic thin profiles and a broadband spectral coverage from visible to infrared wavelength range. These advantages make 2D materials an alternative candidate to form high performance optoelectronic devices with additional features of ultra-low-weight and flexibility. The applications can be in photovoltaics, photodetectors, electrodes and water purification.[15] For example, black Phosphorus, graphene and Molybdenum disulfide ($MoS_2$), have been demonstrated tremendous potential for optoelectronic applications. Graphene, as a most extensively investigated two-dimensional material, has been widely used in broadband photodetection and many other optoelectronic applications.[16,17] Here, some important characteristics for photodetection applications using different 2D materials are summerized in **Figure 1.2**.[18] These 2D material-based photodetectors show ample competitiveness over commercial silicon and InGaAs photodiodes (PD). Graphene and black Phosphorus, in particular, are very competitive on both responsivity and response time when compared to Silicon PD and InGaAs PD (as shown in Figure 1.2A). They can be sensitive from near-infrared (NIR) to far-infrared (FIR) (Figure 1.2B). Both of these two characteristics make them alternative materials for applications on SWIR photodetection. But, regarding the preparation process and device fabrication, 2D materials are facing some problems: most of them need manual exfoliation process, which is difficult for large-scale fabrication. In the other hand, chemical vapor deposition (CVD) provides a new strategy to acquire monolayer materials, but the quality of these products still needs to be improved. Thus, the reproducibility issue and rigorous fabrication requirement make 2D material-based devices remain a laboratory-level demonstration.

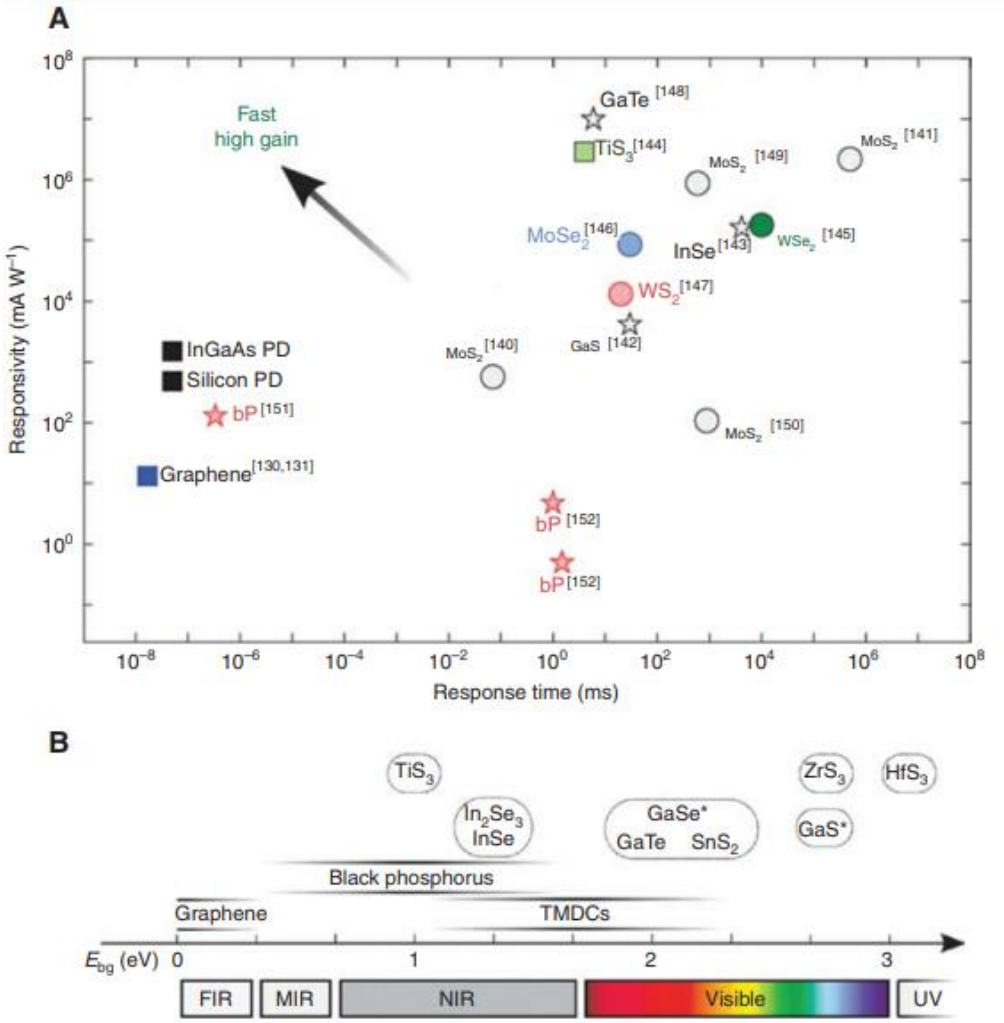


**Figure 1.2** *Summarization of important characteristics for detection application using different 2D materials. (A) Responsivity versus the response time for detectors based on 2D material and comparison with commercial silicon and InGaAs photodiodes (black squares). (B) Bandgap of the different layered semiconductors and the covered electromagnetic spectrum. The exact bandgap value depends on the number of layers, strain level and chemical doping. The asterisk indicates that the material's fundamental bandgap is indirect. [Ref. 18]*

Colloidal PbS also shows interesting performance owing to their advantages in solution-processability, size-tunable spectral absorption and flexible substrate compatibility.[12] **Figure 1.3**[12] shows the PbS nanocrystals' tunable optical properties, spectral range, responsivity and detectivity comparison of conventional state-of-the-art photodetectors. As shown in Figure 1.3a, PbS nanocrystals have a broadband spectral coverage from 200 nm to 2400 nm owing to their size-tunablility from 4.3 nm to 8.4 nm (Figure 1.3b). These PbS

nanocrystals can be formed into different photodetectors, including photoconductor, phototransistor and photodiode. Very high responsivity ($R$) and detectivity ($D^*$) are obtained from these devices. These superior performances make colloidal PbS nanocrystals promising candidates for the next-generation photodetectors. However, PbS nanocrystals have several shortcomings: air stability and the mobility of charge carriers in the nanocrystal films, that still need to be improved. In addition, when these materials are exposed to large-scale fabrication and our everyday life, the highly toxic lead in colloidal PbS is problematic to biology and environment, as well as the safety and security of fabrication/recycle process.

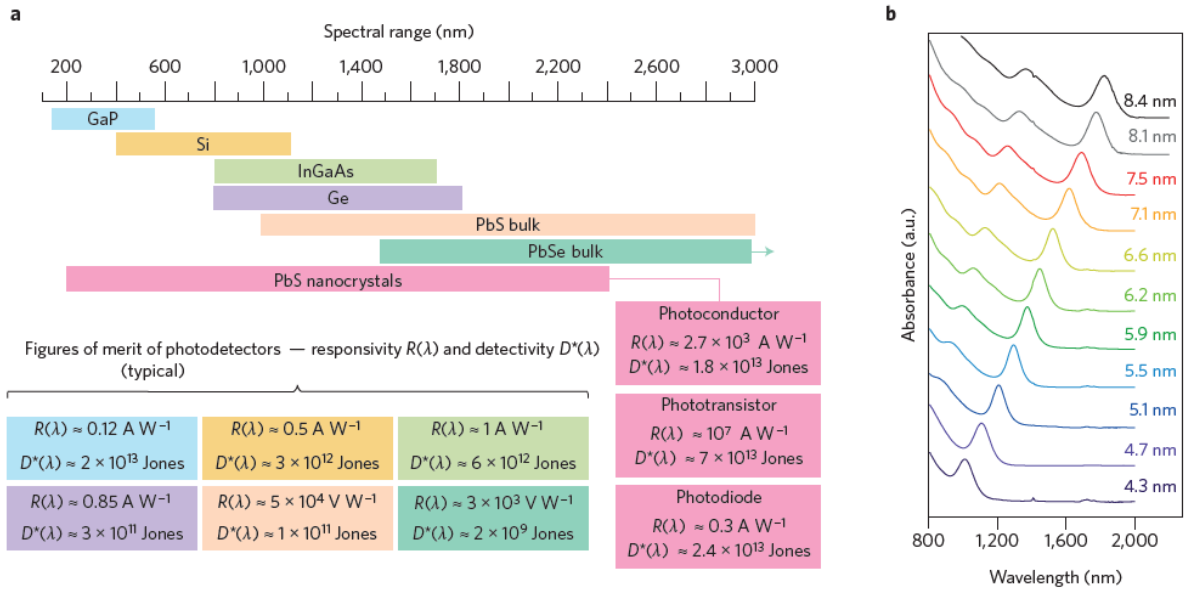


**Figure 1.3** *Tunable optical properties of PbS nanocrystals. a, Spectral range, responsivity and detectivity comparison of conventional photodetectors (GaP, Si, InGaAs, Ge photodiodes, and bulk PbS and PbSe photoconductors) with PbS NC-based photodetectors. b, Size-dependent optical absorption spectra for PbS NCs. [Ref. 12]*

Besides the above-mentioned materials, plasmonic nanostructures based on noble metal represent another class of new materials to enable SWIR photodetection.[14] Current plasmonic photodetectors rely on the extraction of "hot carriers" (i.e., highly energetic carriers not in thermal equilibrium with the metal atoms) produced during the decay of the localized surface plasmons from a metal nanostructure. Based on this principle, various hot-carrier photodetectors were fabricated by lithographically defined nanostructures, exhibiting photoresponsivity ranging from a few nA $W^{-1}$ to a few tens of mA $W^{-1}$.[7,19,20] **Figure 1.4**[21]

shows us a hot electron photodetection based on Au nanostructured arrays with a strongly resonant and broadband photocurrent response in the SWIR. Figure 1.4a and 1.4b show the device structure and the Au nanostructured arrays, which are periodic nanostructures. It is worth mentioning that their strong resonant absorption is tunable, which is determined by the nanostructure periodicity (as shown in Figure 1.4c and 1.4d). On a typical metamaterial perfect absorber (MPA) photodetector (D6), the nanostructure periodicity is L = 195 nm and P = 360 nm, respectively. Its responsivity is around 2.0 mA/W and covers the spectrum from 1200 nm to 1500 nm (Figure 1.4e). However, complex nanostructured arrays are difficult to achieve in large-scale mass production. The preparation by electron beam lithography (EBL) is not scalable and low-consumption process. Furthermore, so far, there is no detailed data to prove that these photodetectors based on lithographically defined nanostructures can be functional well under optical excitation with high modulation frequency, which is an important parameter for data communication applications.

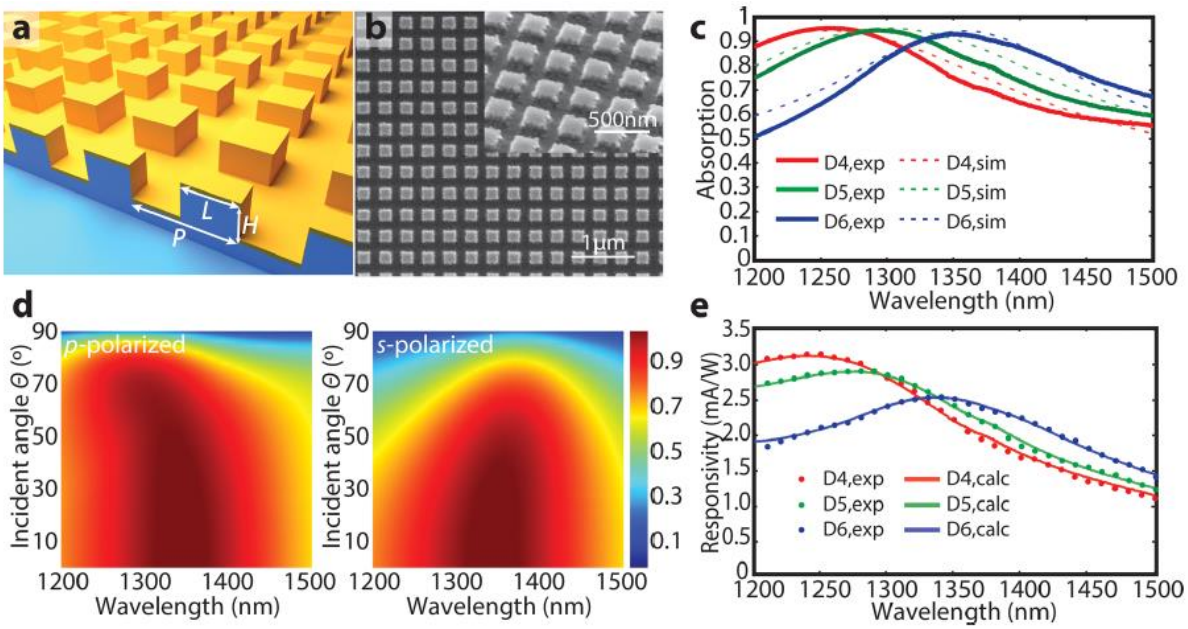


**Figure 1.4** *(a) Schematic of the polarization-independent MPA photodetectors. Dimensions of MPA photodetectors D4, D5, and D6 are L = 185, 195, and 195 nm and P = 340, 340, and 360 nm, respectively. The etching depth, H, for the three devices was 135 nm. (b) Scanning Electron Microscopy (SEM) image of a fabricated device. (c) Experimentally measured (solid lines) and simulated (dashed lines) absorption spectra of D4, D5, and D6 (red, green, and blue lines, respectively). (d) Finite-difference time-domain (FDTD) simulation of the angularly dependent optical absorption for p- (left) and s-polarized light (right). (e)*

*Experimentally measured (circles) and calculated (lines) photoresponsivity spectra of D4, D5, and D6 (red, green, and blue, respectively). [Ref. 21]*

These materials or systems show great superiority in high modulation frequencies and/or high sensitivity as candidates for the next-generation photodetectors, but they still have some disadvantages, such as epitaxial growth requirement, difficult to mass production and environment unfriendly involving highly toxic elements.[22–24] Here, we summarized the three candidates (2D materials, colloidal PbS and plasmonic nanostructures) in their terms of marketization, considering these two indices: Preparation process and Toxic heavy elements, as shown in **Table 1.1**.

**Table 1.1** *Summary of three candidates (2D materials, colloidal PbS and plasmonic nanostructures) in their terms of marketization, considering these two indices: Preparation process and Toxic heavy elements.*

| **Candidates** | **Preparation process (production cost)** | **Toxic heavy elements (environmentally friendly)** |
|---|---|---|
| 2D materials | Manual exfoliation process | No |
| Colloidal PbS | Solution process | Lead |
| Plasmonic nanostructures | Electron beam lithography | No |

On the path to the market, these drawbacks are becoming the main reasons to their remained unmarketable for consumers and industry: rigorous production process, costly manufacturing, only small-scale and low-volume, uncertain in the health, safety and security. These facts mean that finding alternatives with a cost- and performance- competitive over current III-V InGaAs or HgCdTe systems is still going on. To the point, the new generation SWIR photodetector needs a simultaneously cost- and performance- competitive production process, which should take both preparation process and toxic heavy elements into account (as we summarized in Table 1.1). This is why two-dimensional materials still haven't been able to be industrialized and marketed, although they have been very popular in recent years[25] due to

their excellent photoelectric performance. Currently main research can only obtains small-scale and low-volume experimental samples by manual mechanical exfoliation or harsh deposition techniques. Given these facts, colloidal nanocrystals with superior optical property and simple solution process show some outstanding features to overcome the unmarketable problem: low-cost and mass production. By comparison to the colloidal PbS QDs, some environmentally friendly and physically-chemically stable nanocrystals are more adapt to the current trend of green energy and durable development. Thus, in my doctoral project, I focused on seeking solution-processed nanoparticles with suitable optical properties and absence of toxic heavy elements for SWIR photodetection. Two candidates were confirmed in my project: Metallic nanoparticles (gold nanorods) and Upconversion nanocrystals ($NaYF_4$:$Er^{3+}$).

Metallic nanoparticles ( mainly Ag and Au) possess the capability of scale-synthesis, high physical & chemical stability and low biological toxicity, large optical absorption cross-section.[26–30] Thus, these nanoparticles have been applied in many fields, such as catalysis,[31,32] solar energy harvest,[33,34] optical switching,[35] cancer therapy,[36–39] and drug delivery.[40] The photoexcitation and relaxation mechanism of metallic nanoparticles reveals that hot carriers generation (on a time scale ranging from 1 to 100 fs) and transfer (on a time scale ranging from 100 ps to 10 ns) are ultra-fast and efficient processes. This suggests that the plasmonic induced colloidal nanoparticles create a feasible condition for ultra-fast and high sensitivity photodetection.[41,42] In these metallic nanoparticles, gold nanorods (Au NRs) reveal outstanding tunable optical properties by changing the aspect ratios (**Figure 1.5**A, ref. 43). As shown in Figure 1.5B and 1.5C, when the aspect ratio is larger (from 2.4 to 6.6), the gradient feature of the color from these Au NRs is observed, the optical absorption peak can be more red shift (from 650 nm to 1050 nm). This means that Au NRs with a larger aspect ratio will be sensitive to SWIR light. Therefore, owing to their ultra-fast photoexcitation/relaxation process and SWIR light- sensitivity, it is possible to apply the high aspect ratio Au NRs to SWIR photodetection.

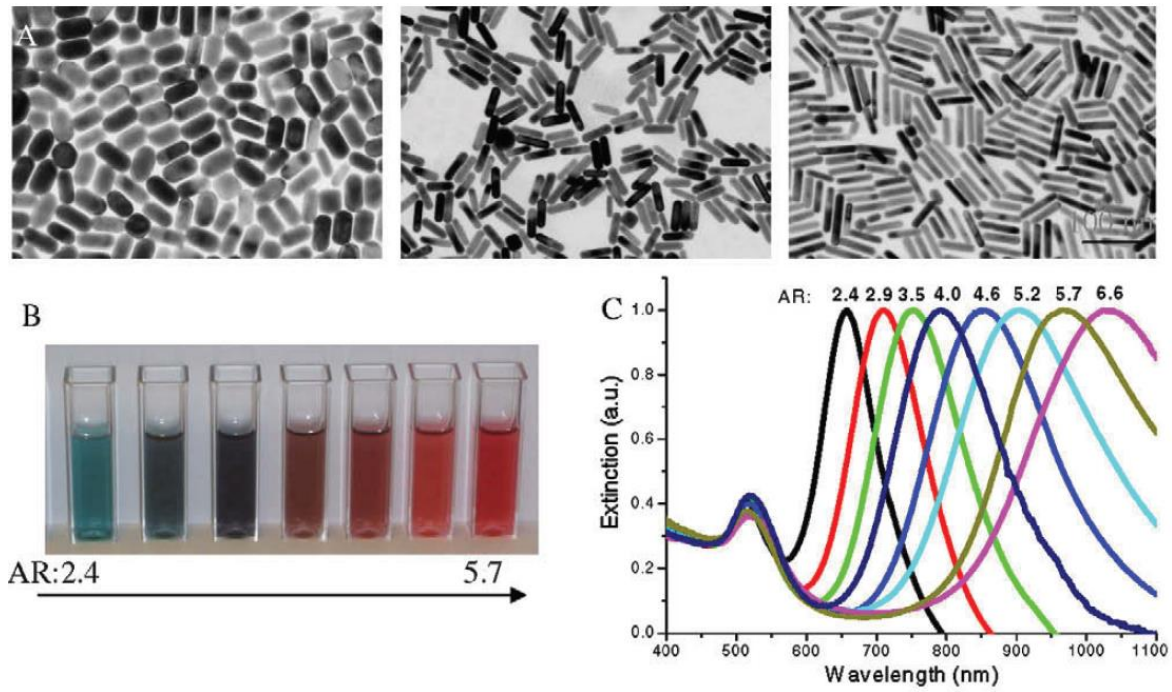


**Figure 1.5** *Tunable optical properties of gold nanorods by changing the aspect ratios. Gold nanorods of different aspect ratios exhibit different dimensions as seen by TEM (A), in different color (B) and different SPR wavelength (C). [Ref. 43]*

Upconversion nanocrystals (UCNPs), which are luminescent nanomaterials that convert a near-infrared excitation into several visible emissions through lanthanide doping,[44,45] display very distinctive optical characteristics. Owing to their large anti-Stokes shifts (up to 500 nm) that separate discrete emission peaks from the infrared excitation, and the high photochemical stability & sharp emission bandwidths, upconversion nanocrystals are used in a diversity of applications. Here, selective milestones in multifunctionalization of upconversion nanoparticles for emerging applications in recent years are listed in **Figure 1.6**.[46] These applications are widespread in many fields, including multimodal imaging, cancer therapy, volumetric displays and photonics.[46] In particular, owing to their ability of upconversion, UCNPs can convert unutilized sub-bandgap NIR photons into visible photons for photovoltaic devices, like Dye-sensitized solar cells (DSSCs), as shown in **Figure 1.7**.[47] The rare-earth elements in these UCNPs, $Nd^{3+}$, $Yb^{3+}$, $Ho^{3+}$ and $Er^{3+}$, contribute to the upconversion from the infrared band of 800 nm, 1000 nm, 1200 nm and 1500 nm, respectively (Figure 1.7a). This suggests that these rare-earth elements are sensitive to certain infrared light. It inspires us that $Er^{3+}$ is sensitive to 1500 nm, meaning that $Er^{3+}$ doped UCNPs (such as $NaYF_4$:$Er^{3+}$) can be a candidate for SWIR photodetection. In addition, UCNPs can be hybrid with DSSCs by

different structures (structure 1, structure 2 and structure 3 in Figure 1.7b), revealing the feasibility of using UCNPs for SWIR photodetectors.

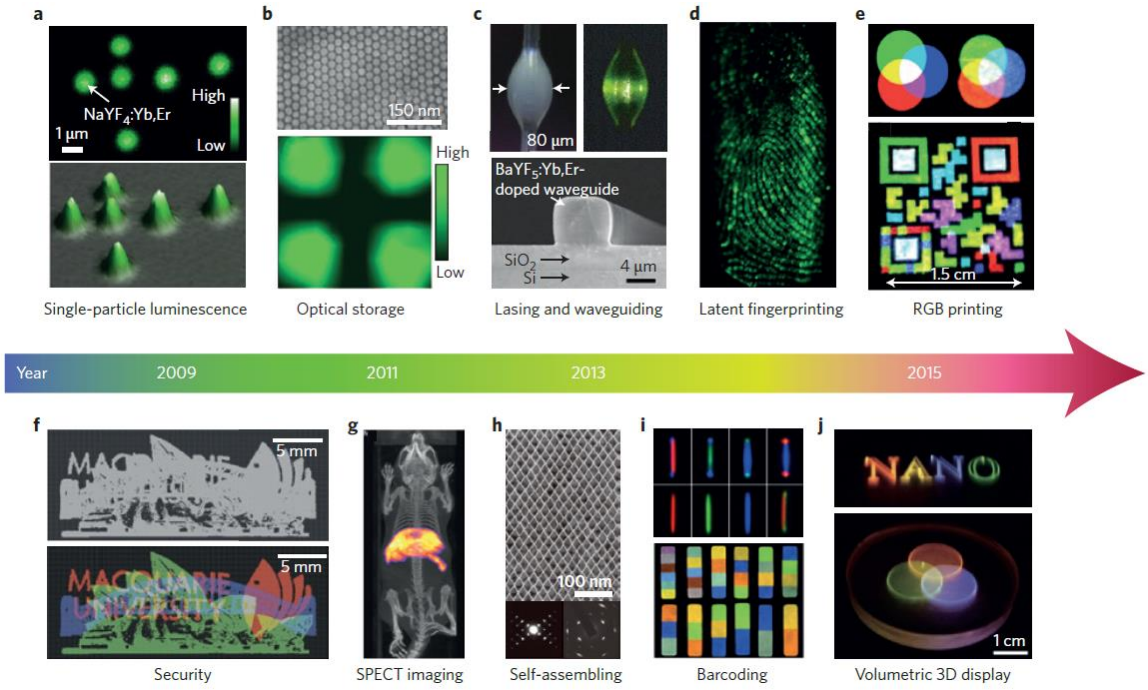


**Figure 1.6** *Selective milestones in multifunctionalization of upconversion nanoparticles for emerging applications. a, Confocal imaging of $NaYF_4$:Yb,Er nanoparticles at the single-particle level. The colour scale represents photon counts. b, Rewritable optical storage enabled by patterned NIR-light-responsive nanoparticles. Scanning electron microscope image (top) and luminescence mapping image (bottom) of patterned substrates consisting of $NaYF_4$:Yb,Er nanoparticles. The colour scale represents the photoluminescence intensity. c, Lasing and waveguide amplifier using the nanoparticles as gain media. Top: Photographs of the $NaYF_4$:Yb,Er@$NaYF_4$-containing microcavity before (left) and after (right) pulsed laser excitation at 980 nm. Bottom: Scanning electron microscope image of the waveguide device modified with $BaYF_5$:Yb,Er@$BaYF_5$ nanoparticles. d, Latent fingerprinting through the use of $NaYF_4$:Yb,Er nanoparticles. e, Red–green–blue (RGB) printing involving nanoparticle inks. Top: Schematic design for creating secondary colours (left) and the corresponding image of the experimental result (right). Bottom: Multicolour barcode printing using $NaYF_4$:Yb,Er(Tm) nanoparticles. f, Demonstration of document security printing, made possible by three sets of lifetime encoded $NaYF_4$:Yb,Tm nanoparticles. The overlaid patterns (top) printed with nanocrystals having three distinct lifetimes can be decoded (bottom) by a time-resolved confocal fluorescence microscope equipped with a 980 nm laser. g, In vivo whole-body 3D*

*imaging involving single-photon emission computed tomography (SPECT) through the use of 153Sm-radioactivated $NaLuF_4$:Yb,Tm nanoparticles. h, Self-assembly of fluoride-based nanoplates. Top: Electron microscope image of a 2D superlattice of $DyF_3$ rhombohedral nanoplates. Bottom: Small-angle (left) and wide-angle (right) electron diffraction patterns of the superlattice. i, Multicolour barcoding through single particles. Top: Optical micrograph of dual-colour-banded single-crystalline microrods. Bottom: Luminescence image of multicolour-banded rod-shaped particles fabricated by microfluidic devices. j, Full-colour volumetric 3D display using pulse-duration-sensitive nanoparticles. [Ref. 46]*

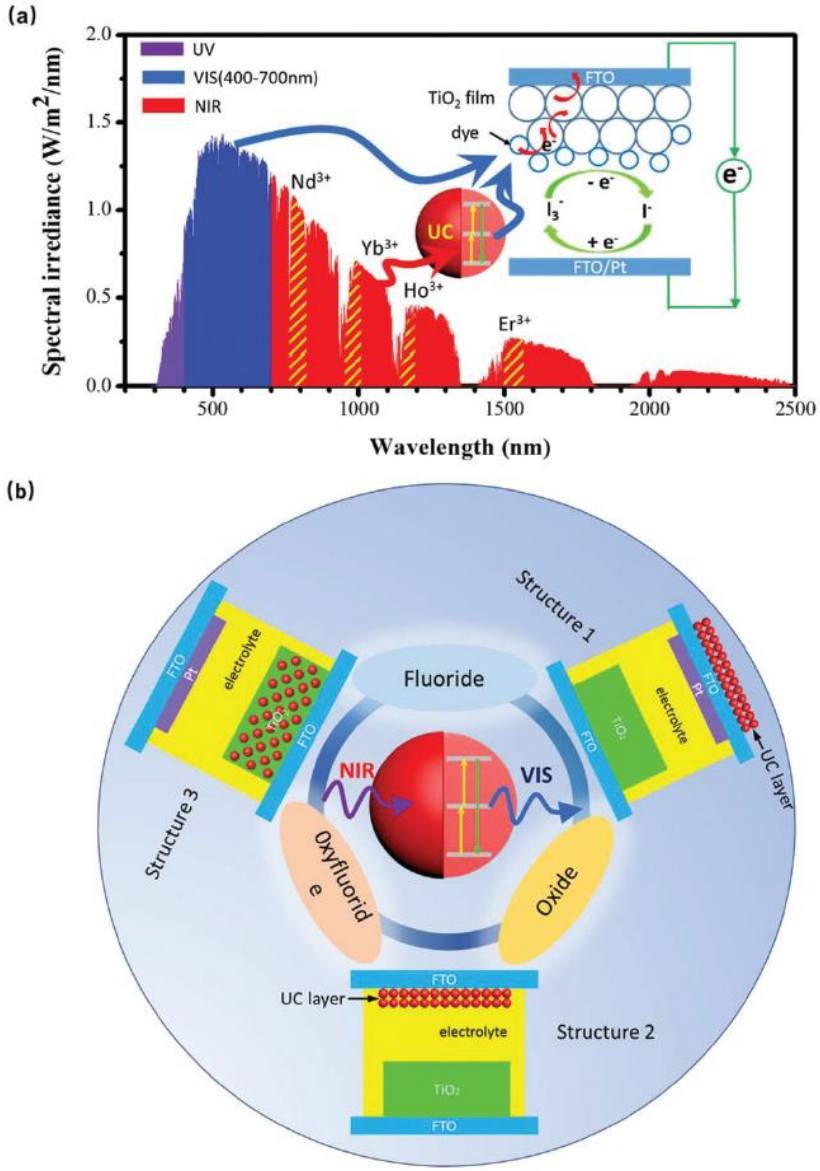


**Fig. 1.7** *(a) Scheme illustrating the harvesting of infrared sunlight (700–2500 nm) by upconversion to visible light (400–700 nm) to which a typical DSSC structure can respond to (inset). (b) Three structures of DSSCs with rare-earth upconversion in varying host lattices in literature. [Ref. 47]*

Due to the interesting optical performance of these colloidal nanocrystals (Au NRs and $NaYF_4:Er^{3+}$), we used them in a hybrid structure to form the innovative SWIR photodetectors in my project. We provided a solution-based fabrication process for both synthesis and devices, showing cost- and performance- competitive advantages for next-generation of SWIR photodetectors.

Firstly, a series of monodisperse colloidal nanocrystals were synthesized at the beginning of my project.

1) Au NRs: We synthesized a series of monodisperse colloidal gold nanorods of different aspect-ratios (ARs) with their longitudinal LSPR maximum tunable from 900 nm to 1.3 μm. The synthetic tuning was achieved by controlling the amount of four parameters: silver nitrate ($AgNO_3$), Au seeds, hydrochloric acid (HCl), sodium oleate (NaOL). Detailed preparation process is described in the experimental section of chapter 2.2. While most reported colloidal Au NRs exhibit a longitudinal LSPR (L-LSPR) in the wavelength range shorter than 1200 nm, we successfully extend the aspect-ratio (AR) of Au NRs up to 10.96 with their L-LSPR absorption peak reaching 1300 nm.

2) $NaYF_4:Er^{3+}$: A series of monodisperse colloidal $NaYF_4$:15%$Er^{3+}$ UCNPs were first synthesized by an improved hydrothermal route. To adjust the size of the upconversion nanoparticles, different molar amounts of sodium citrate tribasic dihydrate were used to react with a fixed amount of $Ln^{3+}$ (containing 85% $Y^{3+}$ and 15% $Er^{3+}$) and NaF. Detailed preparation process is described in the experimental section of chapter 3.2. With the rest of the synthetic parameters being identical, the amount of sodium citrate tribasic dehydrate allowed a tuning the UCNP particle dimension from 150 nm to 1000 nm.

Benefiting by their surface plasmon resonance (SPR), Au NRs have a significant photothermal effect, which can be applied into optical sensing and biomedical field. Thus, in this work, a study of the temperature increase of Au NRs excited at 1.537 μm is presented to prove that the photothermal effect from Au NRs is high-efficiency. We will show that a few NRs can produce a local temperature increase of several tens of degrees, making them very efficient heaters in this wavelength range. Since the photothermal effect of Au NRs is efficient, a hybrid device structure, composing of Au NRs on the surface of a NTC-thermistor, was proposed as an alternative low-cost approach for sensing in the SWIR spectrum. Under a

monochromatic illumination of relatively low intensity (< 1 mW/cm$^2$), hybrid Au-NRs/thermistor devices exhibit a clear photoresponse in the form of photo-induced resistance drop in the wavelength window from 1.0 μm to 1.8 μm. This is in contrast to the control device (thermistor alone without Au NRs), the photoresponse of which is negligible under the same illumination condition. The photo-responsivity of the hybrid device reaches a maximum value of $2.06\times10^7$ Ω/W at 1.3 μm, a wavelength in agreement with the L-LSPR maximum of the Au NRs applied. At higher illumination intensities (from 6.7 mW/cm$^2$ to 4464.3 mW/cm$^2$) achieved by a laser (λ = 1.5 μm) focused onto device, due to the laser-induced heating photoresponse was observed in both the control and the hybrid device. Nevertheless, in this case hybrid devices exhibited more than 5-fold enhancement of photoresponsivity by comparison to the control device. Thus, these results suggest that the plasmonic-induced photothermal effect of Au NRs (i) enables the photo-sensing capability in a hybrid Au-NRs/thermistor device structure under relatively weak illumination and (ii) boost the photo-response of the hybrid device when illumination intensity is high. The response speed of the current Au-NRs/thermistor hybrid device is as short as 2 seconds, limited by the response speed of the thermistor itself. To improve the response speed of these Au-NRs-based SWIR photodetectors, we propose a new hybrid SWIR photodetector structure based on the coupling between a resistive platinum (Pt) microwire and colloidal plasmonic Au NRs which is capable to reduce the photoresponse time of more than *four orders of magnitudes* compared to our previous work. Pt was chosen here due to its large temperature coefficient of resistance, wide operation temperature range and high stability. The combination of these characteristics has led to the extensive applications of Pt as a resistance temperature detector (RTD). Here a series of Pt microwires of various dimensions were fabricated and applied to harvest the photothermal effect of Au NRs in an Au-NRs/Pt hybrid device structure. In an optimized Au-NRs/Pt photodetector, we measured a response time of 97 μs under the illumination of a λ=1.5 μm laser with its ON/OFF modulated at 120 Hz. In particular, even at an illumination modulation frequency of 50 kHz, such Au-NRs/Pt photodetectors are still capable to generate clear photoresponse switching. These hybrid Au-NRs/Pt photodetectors, able to provide a fast conversion between SWIR photons, heat, and resistance change at a frequency up to tens of kHz, thus represent a brand-new strategy for SWIR photodetection alternatives, meeting the needs of emerging applications demanding reduced fabrication cost and high operation speed.

One other possible strategy for SWIR photodetection is to apply photon upconversion, a phenomenon to convert low energy photons into high energy ones. Various upconversion systems in the form of solution-processed nanoparticles (NPs) have been synthesized, mostly based on the doping of trivalent lanthanide cations in a low phonon energy hosts and performing upconversion through a two- or multi-photon mechanism. Since then they have been applied into many applications including biomedical engineering, thermal sensing, solar energy harvest, and photodetection. Indeed, most of these photon upconversion applications are based on $Yb^{3+}$ and $Er^{3+}$ co-doped systems capable to upconvert near-infrared light with a wavelength maximum no larger than 1.0 μm (e.g. upconversion from 808 nm or 975 nm to visible photons). Material systems able to upconvert SWIR photons remain rare. In this work, by a photodiode device architecture, we propose high-performance heavy-metal-free flexible photodetectors sensitive to $\lambda$ = 1.5 μm photons based on the formation of a solution-processed organic/inorganic hybrid composing of conjugated polymer/small molecule bulk-heterojunctions (BHJs, host) together with $Er^{3+}$-doped upconversion nanoparticles (UCNPs, guest). A series of monodisperse colloidal inorganic $NaYF_4$:$Er^{3+}$ UCNPs of various dimensions were synthesized by hydrothermal routes, providing effective upconversion of $\lambda$ = 1.5 μm photons to visible ones. An organic host was applied containing a donor-accepter BHJ blend of diketopyrrolopyrrole (DPP)-based copolymer and [6,6]-phenyl-$C_{71}$-butyric acid methyl ester ($PC_{70}BM$). Such organic host exhibits strong optical absorption covering the visible and near-infrared spectrum up to $\lambda \approx 1$ μm and is thus capable to efficiently harvest most visible photons upconverted by the guest nanoparticles. Under the illumination of $\lambda$ = 1.5 μm SWIR photons, optimized hybrid BHJ/UCNP photodetectors exhibit a clear photoresponsivity of 0.73 mA/W and 0.44 mA/W for devices built on rigid glass substrates and flexible polyethylene terephthalate (PET) substrates, respectively. Remarkably, a fast operation speed characterized by a short photocurrent rise time down to 80 μs was observed under the illumination of $\lambda \approx 1.5$ μm photons, which is faster by more than one order of magnitude than previous photodetector studies applying $Er^{3+}$- doped upconversion systems, and by two to four orders than most other nonavalanche semiconductor photodetectors at SWIR wavelengths. Exhibiting advantages such as adaptability to flexible substrates, processability in solution, absence of highly toxic heavy metals, and superior performance, the hybrid organic/inorganic photodetectors developed in this work can be a bright contender for next-generation low-cost and high-performance SWIR photodetectors.

# 2. Au NRs for SWIR photodetectors

In this chapter, we aim to achieve SWIR photodetection by colloidal Au NRs with an optical absorption cross-section covering SWIR spectrum. It is realized by obtaining suitable Au NRs with their absorption tunable in the visible-SWIR spectrum by the tunability of their aspect-ratio. In order to harvest the remarkable photothermal effect from these Au NRs, we combined them with thermistors and resistance temperature detectors (RTD) to form hybrid photodetectors. Introduction of the characteristics and feasibility of using Au NRs for SWIR photodetection is performed in **chapter 2.1**. Experimental details of synthesis, device fabrication and measurement are performed in **chapter 2.2**. Then, we present the results and discussion in **chapter 2.3**.

## 2.1 Introduction of Au NRs

In recent decades, gold nanoparticles, especially gold nanorods (Au NRs), have aroused extensive concern in the application of biomedical field, optical sensing and optoelectronic devices owing to their extremely attractive properties: (i) surface plasmon resonance (SPR) dominant optical properties, (ii) tunability of the rod aspect-ratio (AR) and therefore optical spectra in the visible-SWIR region, (iii) high physical & chemical stability and low biological toxicity.[26–30] Due to these fascinating properties, a great deal of research and literature has emerged about Au NRs synthesis,[48–50] self-assembling,[51–53] coupling modes[54–56] and optical applications, such as light scattering,[57,58] photothermal therapy,[59–62] photoluminescence,[63] nanothermometers[64] and pressure sensor[65].

Owing to the tunability of the aspect-ratio (AR), Au NRs can give optical spectra in the visible-NIR-SWIR region,[66] meaning that they have potential detectivity to form broadband photodetectors, especially for SWIR (1000 nm - 3000 nm) photodetection, which mainly relies on InGaAs,[67,68] InSb,[69] PbS,[70] and HgCdTe.[71] To our best knowledge, vast amounts of photo-sensing applications of Au NRs appeared, mainly in biomedical field, in vivo

imaging[72–74] and photothermal cancer therapy.[75–78] But most of current research focus on the optical region < 1000 nm (AR < 6): Aquiles Carattino *et al* used gold nanoparticles as absolute nano-thermometers (AR = 2),[64] Edakkattuparambil Sidharth Shibu *et al* applied small gold nanorods for photothermal microscopy in cells (AR = 2 ~3),[79] Hui Hou *et al* fine-tuned the localized surface plasmon resonance (LSPR) of Au NRs with high photothermal efficiency for cancer cell ablation (AR = 3 ~4),[75] Takuro Niidome *et al* modified Au NRs for in vivo applications (AR = 6)[80]... Nevertheless, for high aspect-ratio Au NRs (AR > 10, LSPR covering of SWIR region), the discussion and application are still rare. Applying Au NRs for SWIR photodetection has not been presented or implemented, to our best knowledge.

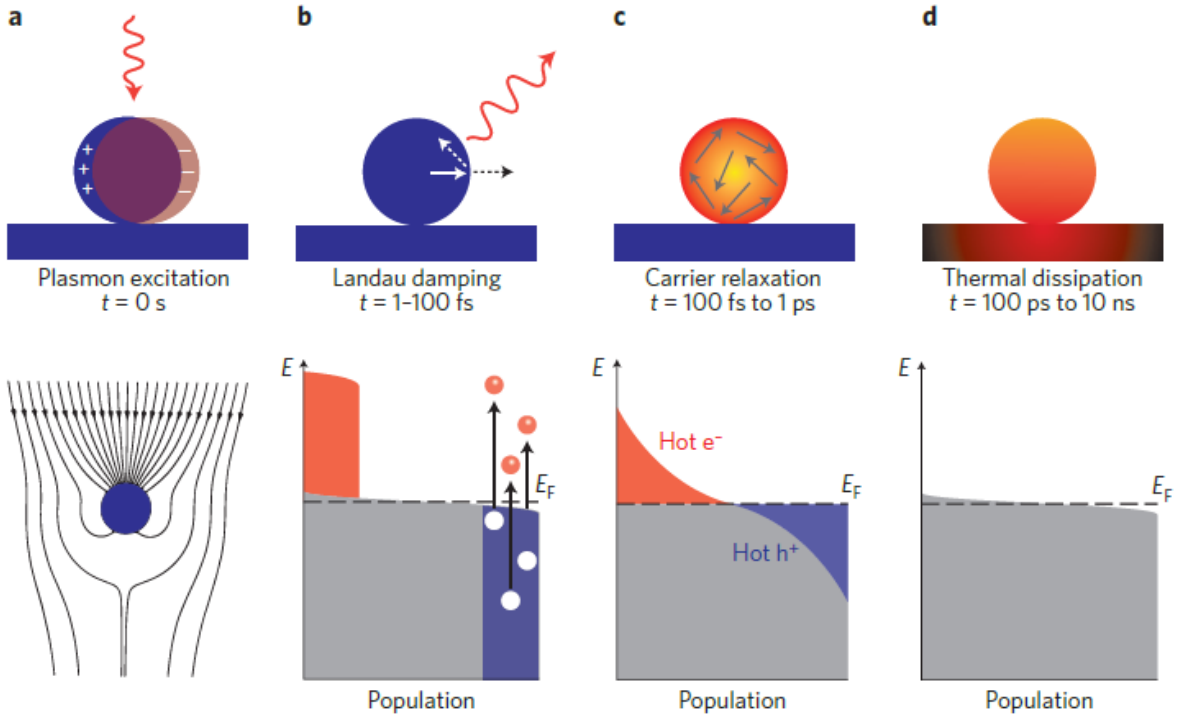


**Figure 2.1** *Photoexcitation and relaxation of metallic nanoparticles. a–d, Photoexcitation and subsequent relaxation processes following the illumination of a metal nanoparticle with a laser pulse, and characteristic timescales. a, First, the excitation of a localized surface plasmon redirects the flow of light (Poynting vector) towards and into the nanoparticle. b–d, Schematic representations of the population of the electronic states (grey) following plasmon excitation: hot electrons are represented by the red areas above the Fermi energy $E_F$ and hot hole distributions are represented by the blue area below $E_F$. b, In the first 1–100 fs following Landau damping, the thermal distribution of electron–hole pairs decays either through*

*re-emission of photons or through carrier multiplication caused by electron–electron interactions. During this very short time interval $\tau_{nth}$, the hot carrier distribution is highly non-thermal. c, the hot carriers will redistribute their energy by electron–electron scattering processes on a timescale $\tau_{el}$ ranging from 100 fs to 1 ps. d, Finally, heat is transferred to the surroundings of the metallic structure on a longer timescale $\tau_{ph}$ ranging from 100 ps to 10 ns, via thermal conduction. [Ref. 41]*

Meanwhile, the hot carriers generation and transfer in plasmonic materials create a feasible condition for fast response photodetection.[30,41,81,82] Generation and transfer processes of hot carriers are shown in **Figure 2.1**.[41] After photon absorption and subsequent LSPR excitation in Au NRs, hot carriers are generated via Landau damping on a time scale ranging from 1 to 100 fs, then quickly redistribute their energy toward lower energy electrons via electron-electron scattering followed by thermalization with the lattice and heat dissipated to the surroundings on a time scale ranging from 100 ps to 10 ns. Subsequent heat transfer is related to the restriction from the nanoparticle size, the material and the thermal conduction properties of the surroundings.[30,41]

This ultrafast process of hot carriers generation and transfer in plasmonic materials reveals that metallic nanoparticles (*e.g.* Au NRs) have effective photosensitive property. Considering their large optical absorption cross-section and tunability of their optical spectra[26–30], colloidal Au NRs can be an alternative material for photodetectors. Therefore, in this project, a series of monodisperse colloidal nanocrystals were synthesized in **Experimental section 2.2.1** by modifying the silver-assisted seed-mediated growth method applying binary surfactants reported previously.[48] $NaYF_4$ :$Er^{3+}$ fluorescent nanocrystal were synthesized (**Experimental section 2.2.2**) to prove that the photothermal effect from Au NRs is high-efficiency, then two hybrid device structures, composing of Au NRs on the surface of a NTC-thermistor and Platinum wire, were fabricated and measured in **Experimental section 2.2.3** and **Experimental section 2.2.4**, respectively. These hybrid devices show an alternative low-cost approach for sensing in the SWIR spectrum (results and discussion in **chapter 2.3**).

## 2.2 Experimental section

### 2.2.1 Synthesis of colloidal Au NRs

**Au nanoparticle seed solution:** After mixing 5 ml of 0.5 mM $HAuCl_4$ solution with 5 ml of 0.2 M CTAB solution, 1 ml of 0.006 M $NaBH_4$ solution was added followed by vigorously stirring for 2 minutes. This solution was then left un-stirred for aging during 30 minutes.

**Au NR growth solution:** 9 g of CTAB was evenly mixed with different amounts of NaOL (listed in Table 2.1). They are then dissolved in 250 ml of de-ionized water under stirring at 50 $^oC$. After the solution was cooled down to 30 $^oC$, different amounts of 4.15 mM $AgNO_3$ solution were added and the whole solution was kept at 30 $^oC$ for 15 minutes. This is followed by the addition of 250 ml of 1 mM $HAuCl_4$ solution under stirring for about 90 minutes (until the solution turned colourless). At this stage, different amounts of a 12.1 M HCl solution were added under stirring for 15 minutes. 1.25 ml of 0.064 M ascorbic acid solution was then added under vigorous stirring for 30 s. Finally, different amounts of seed solution were added first under rigorous stirring for 30 s then the whole solution was kept un-stirred for 12 hours at 30 $^oC$ for NR growth. After 12 hours of growth the final product was isolated by centrifugation (6k rpm for 30 minutes) and subsequent decantation of mother liquid. De-ionized water was then added to re-dissolve the Au NRs. The centrifugation/decantation process was repeated for 3 times and the final Au NR products were dissolved in de-ionized water.

### 2.2.2 Synthesis of $NaYF_4:Er^{3+}$ fluorescent nanocrystals

To demonstrate the photothermal effect of these Au NRs, a nanothermometer, $NaYF_4$ nanocrystal (NC) doped with $Er^{3+}$ ions were synthesized by modifying the typical hydrothermal method described in ref 83. The relative composition was 85% of Y and 15% of Er. The nanocrystal had a hexagonal phase and their diameter was around 230 nm.

In a typical preparation of $NaYF_4$: 15 mol % $Er^{3+}$ NC, a 5 mL aqueous solution of $Ln(NO_3)_3 \cdot 6H_2O$ (0.2 mol/L, lanthanide ion molar ratio, Y: Er = 85:15) was mixed with a 5 mL aqueous solution of sodium citrate tribasic dihydrate (1.8 mol/L) under vigorous stirring. A white precipitate of lanthanide citrate was observed. A 5 mL aqueous solution of NaF (2.4 mol/L) was then added slowly into the mixture. After being stirred for 1 h, the resulting precursor solution was transferred to a 70-mL-volumn autoclave. The autoclave was then placed in a digital type temperature controlled oven and heated at 120 $^{o}$C for 2 hours. The autoclave was then allowed to cool down to room temperature naturally (typically overnight). The precipitate in the autoclave ($NaYF_4$: $Er^{3+}$ NCs) was then separated from the reaction media by centrifugation (6000 rpm, 30 min), decantation, and dispersion in DI water. This purification process was repeated three times. The final synthetic product was first dried in a vacuum oven at 60 °C for 24 h before being annealed in air at 300 °C for 2 hours.

## 2.2.3 Fabrication and measurement of Au-NRs/Thermistor

To harvest the photothermal from the Au NRs, a temperature- sensitive thermal device, a negative temperature coefficient (NTC) thermistor, was introduced to fabricate a hybrid Au-NRs/Thermistor device. This NTC thermistor with a room-temperature (25 °C) resistance of 10 kΩ (Series B57540G1 from TDK EPCOS) was obtained from RS components (no. 769-1892, ~ 3 €/each). It is then fixed on a glass microscopy slide. To fabricate the hybrid Au-NRs/thermistor device, a drop (~ 3 µL) of Au NR water solution (sample h of table 2.1, with a concentration ranging from 0.6 g/L to 7.2 g/L) was casted directly to coat the surface of the thermistor. After the Au NR solution was dried on the thermistor, Scanning Electron Microscopy (SEM) characterizations were performed directly onto the hybrid device (FEI Magellan 400 system, field emission gun source). The hybrid device was measured under monochromatic illumination generated by a quartz halogen lamp and a computer-controlled Oriel Cornerstone monochromator (and appropriate order sorting filters). The intensity of the monochromatic illumination was calibrated by a NIST-calibrated germanium photodiode. The monochromatic illumination was modulated by a shutter while we measured the resistance of the hybrid and control device by a computer-controlled Keithley 2634B source measurement unit (SMU). Concerning measurements under laser, the output of a fiber-coupled laser diode ($\lambda$ = 1.5 µm) was focused onto the hybrid or control device. Neutral density filters were used to adjust the laser power while the laser power was calibrated by a laser power meter. The

laser illumination was modulated by a shutter while we measured the device resistance by a Keithley 2634B SMU.

## 2.2.4 Fabrication and measurement of Au-NRs/Pt device

To harvest the photothermal from the Au NRs, a platinum (Pt) microwire was introduced to fabricate a hybrid Au-NRs/Pt device. The Pt microwire resistance temperature detector (RTD) devices with a series of width were prepared by laser direct writing lithography (Heidelberg Ins. Laser writer µPG 101). Quartz coated glass substrates were cleaned by ultrasonication in a bath of de-ionized (DI) water, acetone and 2-propanol followed by $O_2$ plasma etching. A layer of adherence promoter (TI from microchemicals) and a layer of photosensitive resin (AZ5214, microchemicals) were spin-coated one after the other on these glass substrates. Pt microwires of various dimensions were then defined by direct laser writing lithography (Heidelberg Ins. laserwriter µPG101). Substrates were then developed by dipping the sample in a bath of developer (AZ726 MIF, microchemicals) for 30 s with subsequent DI water rising and air-drying. A Ti (5 nm)/Pt (40 nm) layer was then evaporated onto the sample by an e-beam evaporator (Plassys MEB550S). Finally, the sample was lifted-off by immersing samples into a bath of acetone.

To fabricate the Au-NRs/Pt hybrid device, a drop (~ 1 µL) of Au NRs water solution (with a concentration of 1 g/L - 6 g/L) was casted directly to coat the surface of Pt microwire. After the Au NR solution was dried on the surface, SEM characterizations were performed directly onto the hybrid device (FEI Magellan 400 system, field emission gun source). The hybrid device was measured under monochromatic illumination generated by a quartz halogen lamp and a computer-controlled Oriel Cornerstone monochromator (and appropriate order sorting filters). The intensity of the monochromatic illumination was calibrated by a NIST-calibrated germanium photodiode. The monochromatic illumination was modulated by a shutter while we measured the resistance of the hybrid and control device by a computer-controlled Keithley 2634B source measurement unit (SMU). Concerning measurements under laser, the output of a fiber-coupled laser diode ($\lambda$ = 1.5 µm) was focused onto the hybrid or control device. Neutral density filters were used to adjust the laser power while the laser power was calibrated by a laser power meter. The laser illumination was modulated by a shutter while we measured the device resistance by a Keithley 2634B SMU.

## 2.2.5 Characterization for materials

Agilent Cary 5E UV-Visible-NIR spectrometer was used for Au NRs' UV-Visible absorption spectra measurements, as shown in the following figures:
Figure 2.2 Absorbance spectrums of Au NRs in water.
Figure 2.5 Absorbance of Au NRs spin-coated on a $SiO_2$ substrate.
Figure 2.19 (b) Optical absorbance spectrum of a film of Au NRs on a glass substrate

JEOL 2010 microscope operated at 200 kV was used for TEM characterizations of Au NRs' morphology, as shown in the following figures:
Figure 2.4 (a-h) TEM images of Au NRs with different aspect-ratio (AR) and L-LSPR absorbance maximum.
Figure 2.5 Inset: TEM picture of the NRs.
Figure 2.19 (b) the lower inset shows a TEM image of these Au NRs.

FEI Magellan 400 system with a standard field emission gun source was used for SEM characterizations of Au NRs' morphology, as shown in the following figures:
Figure 2.8 a) SEM picture of Au NRs deposited on SiO2 substrate, b) SEM picture of the same zone after the deposition of two luminescent NaYF4: Er3+ NCs on the surface. NanoA is on the NRs and NanoB is 5 μm away from them.
Figure 2.9 c) SEM picture of the scanned zone. The scale bar is 2 μm.
Figure 2.15 (d) SEM image of the Au NRs-coated thermistor exhibiting mostly Au NRs on the surface of the hybrid device.
Figure 2.19 (c) SEM image of a Au-NRs/Pt device with a 10 μm by 2 μm Pt microwire. (d) Zoom-in SEM image of the device permitting the visualisation of Au NRs on the Pt microwire.

Finite difference time domain (FDTD) was used to check the spectral position of the L-LSPR on Au NRs, as shown in the following figure:

Figure 2.6 FDTD calculation of the absorption cross-section of isolated Au NRs on a $SiO_2$ substrate as a function of their AR. Their diameter was fixed to 8 nm, and their length is varied between 80 and 110 nm.

# 2.3 Results and discussion

## 2.3.1 Aspect-ratio tunability of colloidal Au NRs

Here, by a careful synthetic tuning, we synthesized a series of monodisperse colloidal gold nanorods of different aspect-ratios (ARs) with their longitudinal LSPR maximum tunable from 900 nm to 1.3 µm. These gold nanorods (Au NRs) with different ARs were synthesized by modifying the silver-assisted seed-mediated growth method applying binary surfactants reported previously.[48](Synthesis detail is shown in **Experimental section 2.2.1**) While most reported colloidal Au NRs exhibit a longitudinal LSPR (L-LSPR) in the wavelength range shorter than 1200 nm,[84–88] we successfully extend the aspect-ratio (AR) of Au NRs up to 10.96 with their L-LSPR absorption peak reaching 1300 nm. Such a synthesis involved first the formation of gold nanoparticle seeds by reducing gold (III) chloride ($HAuCl_4$) by sodium borohydride ($NaBH_4$) in the presence of hexadecyltrimethylammonium bromide (CTAB) as surfactant. Different amounts of Au seeds were further placed into a growth solution where Au(III) is slowly reduced to Au(I) by a combination of ascorbic acid (AA) and sodium oleate (NaOL) in the presence of hydrochloric acid (HCl), CTAB and silver nitrate ($AgNO_3$). In such a multi-parameter synthesis, we have specifically experimented various amounts of Au seeds, $AgNO_3$, surfactant NaOL, and the acidity of the growth solution (amounts of HCl) (summarized in **Table 2.1**).

**Table 2.1** *Synthetic parameters experimented in this work and the resulting dimension, aspect-ratio, and L-LSPR maximum wavelength of Au NRs. Error bars are calculated from 50 Au NRs measured by TEM images. Aspect-ratios are figured out from specific value of NR average length and NR average diameter. Au NRs' L-LSPR maximum is extracted from the Absorbance spectrums of Au NRs in water, as shown in Figure 2.2.*

| Sample | 4mM $AgNO_3$ (mL) | Au seed (mL) | 12.1 M HCl (mL) | NaOL (g) | NR average length (nm) | NR average diameter (nm) | Aspect ratio | L-LSPR maximum (nm) |
|---|---|---|---|---|---|---|---|---|
| **a** | 24 | 0.3 | 2.1 | 1.234 | 107.2±7.9 | 24.0±2.2 | 4.5 | 903 |
| **b** | 36 | 0.2 | 2.1 | 1.234 | 103.1±9.0 | 22.2±1.9 | 4.7 | 943 |
| **c** | 24 | 0.2 | 2.1 | 1.234 | 103.3±6.5 | 19.9±1.1 | 5.2 | 966 |
| **d** | 24 | 0.3 | 2.1 | 1.234 | 95.9±16.2 | 17.5±3.7 | 5.5 | 980 |
| **e** | 24 | 0.4 | 2.1 | 1.234 | 81.7±5.7 | 14.1±1.6 | 5.8 | 1050 |
| **f** | 24 | 0.8 | 4.2 | 1.234 | 86.1±7.7 | 12.8±1.8 | 6.7 | 1143 |
| **g** | 24 | 0.8 | 4.2 | 0.925 | 132.3±16.9 | 17.5±2.0 | 7.6 | 1193 |
| **h** | 24 | 0.8 | 5.4 | 0.925 | 93.5±13.8 | 8.6±1.4 | 11 | 1300 |

Comparing the results of sample c and sample e (Table 2.1), we observed an increased average length and diameter of Au NRs associated with the decreased amount of Au seeds, which is possibly due to more growth material available per seed. Sample e exhibited a larger AR compared to sample c due to their smaller NR width (diameter). The role of $Ag^{3+}$ in such a synthesis has been reported as crucial as it interacts with CTAB to form elongated templates and hinders the growth of certain crystallographic facets of Au NRs.[26,89] Increasing the amount of $Ag^{3+}$ from the optimum value however led to a decrease of AR due to the thickened NR width (comparing sample b and c, Table 2.1). Concerning the amount of surfactant NaOL, we observed longer and thicker Au NRs with larger AR when the amount of NaOL decreases from 1.234 g to 0.925 g (sample f and g, Table 2.1). The use of NaOL here together with CTAB in the growth solution represents a binary surfactant strategy. NaOL serves here both as a reduction agent and likely also as a surface binding mediator between

CTAB and certain facet of Au to allow NR morphological tuning. Concerning HCl, one modifies the NR growth by controlling the acidity of the growth solution. A larger amount of HCl here led to a reduction of pH favoring larger AR by reducing more significantly the width of NRs (sample g and h, Table 2.1). By controlling these four parameters we were able to tune the AR of NRs from 4.47 to 10.96. As the L-LSPR of Au NRs are highly sensitive to their AR, this series of samples thus exhibits distinctive optical property with a strong and well-defined L-LSPR progressively red-shifted towards 1300 nm as AR increases (**Figure 2.2**).

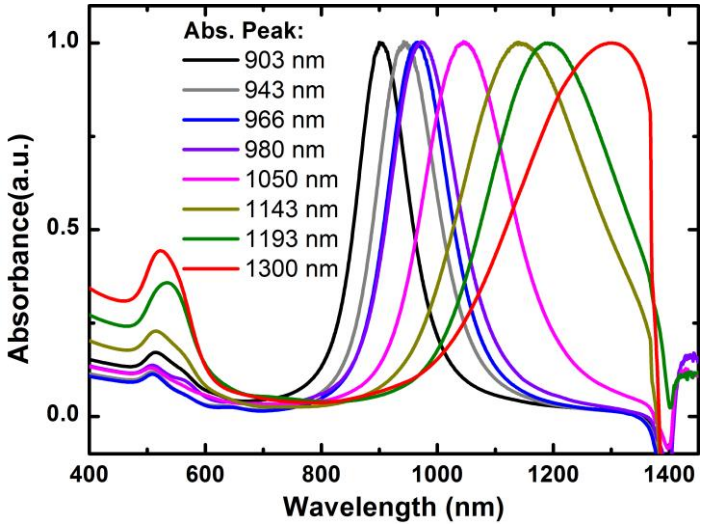


**Figure 2.2** *Absorbance spectrums of Au NRs in water. The absorbance feature at 1400 nm originates from the absorption of water.*

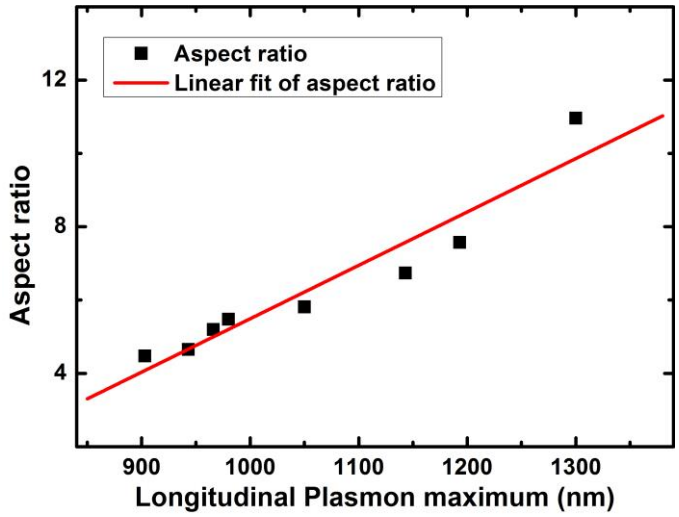


**Figure 2.3** *The evolution of the L-LSPR maximum over the AR of Au NRs. Aspect-ratios are figured out from specific value of NR average length and NR average diameter, as listed in Table 2.1.*

The evolution of the L-LSPR maximum over the AR of NRs roughly follows a linear relation (**Figure 2.3**). The asymmetric shape of the L-LSPR absorbance of samples g and h (Table 2.1, and the green and red curves of Figure 2.2) are due to the artifact originated from water absorption. The small contribution of the transverse-LSPR lies in the wavelength range between 650 to 700 nm, which is relatively less sensitive to the change of AR compared to L-LSPR. The absorption contribution at about 525 nm originates from the existence of semi-spherical Au nanoparticles, which are impurities in the Au NR synthesis. While the proportion of these impurities over Au NRs slightly increased in a NR synthesis for high AR, the majority of the synthetic products of the whole series of samples remained to be NRs of high uniformity as shown in transmission electron microscopy (TEM) characterization (**Figure 2.4**).

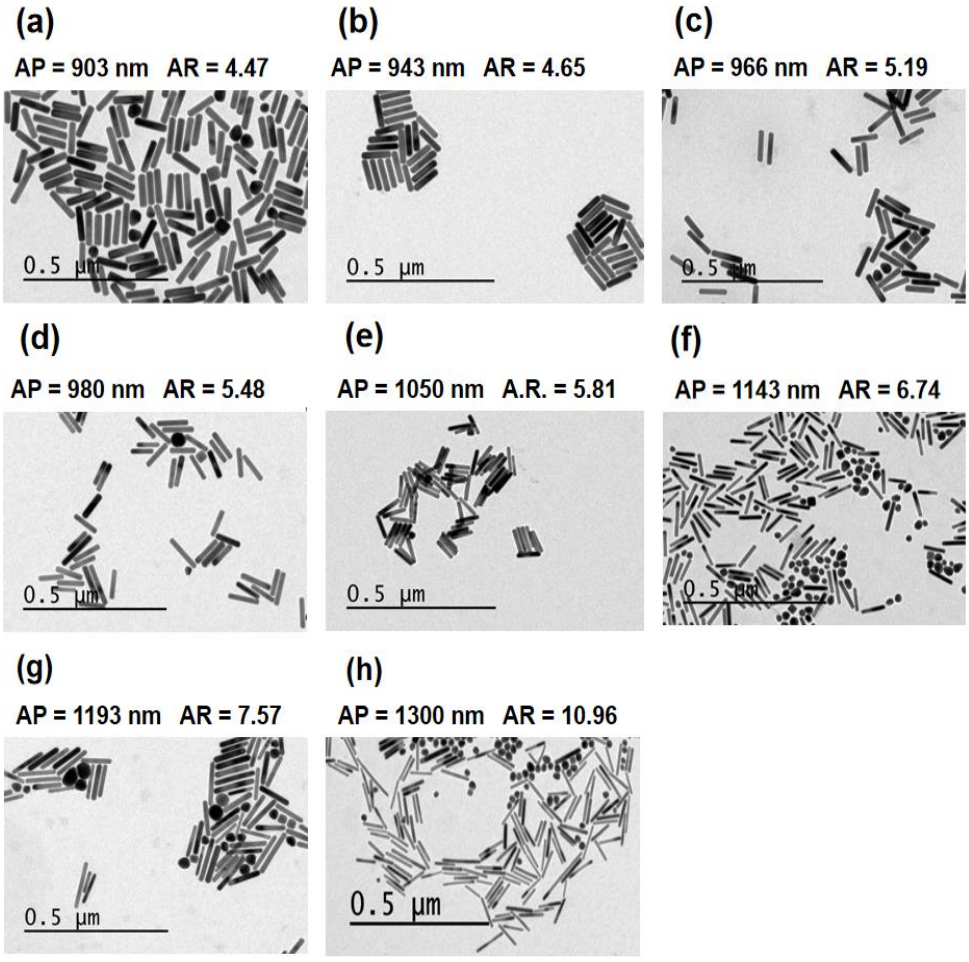


**Figure 2.4** *(a-h) TEM images of Au NRs with different aspect-ratio (AR) and L-LSPR absorbance maximum (Absorbance peak = AP). Correspond to the samples a-h of table 2.1 respectively. AR is figured out from specific value of NR average length and NR average diameter. AP is extracted from the absorbance spectrums of Au NRs in water, as shown in Figure 2.2.*

## 2.3.2 Photothermal effect of Au NRs

Benefiting by their surface plasmon resonance (SPR), Au NRs have a significant photothermal effect, which can be applied into optical sensing and biomedical field.[59,90–97] For this reason, the researches on the Au NRs' photothermal and optoelectronic properties have been popping up in recent years.[65,77,79,90–93,98,99] However, there are still few experiments on the quantitative analysis of a single Au NR's local heating capacity, especially on the high aspect-ratio Au NRs, even though Au NRs have been determined to have good surface plasmon resonance (SPR) and photothermal properties.[60,100]

Here, a study of the temperature increase of Au NRs excited at 1.537 μm is presented to prove that the photothermal effect from Au NRs is high-efficiency. In order to observe the temperature changes as a function of the 1.537 μm laser power, an optical- thermal nanoprobe, lanthanide (Ln) doped upconverting nanoparticles (UCNPs), was used in our experiment as a nanothermometer. These luminescent nanothermometers (NTs) have been proved to have a good temperature-detection performance. Their ability of temperature- detection is based on ratio- metric temperature sensing, which involves taking the ratio between the integrated signals of two well-defined emission bands.[101–106] Therefore, in this part, a UCNP (a single fluorescent $Er^{3+}$-doped $NaYF_4$ nanocrystal, synthesis detail is shown in **Experimental section 2.2.2**) is put on the surface of our Au NRs to measure the temperature variation. We show that a few NRs can produce a local temperature increase of several tens of degrees, making them very efficient heaters in this wavelength range. Numerical simulation of temperature elevation by the photothermal effect of Au NRs is also performed. It confirms the existence of temperature elevation and predicts a larger effect than what is measured. Finally, a summary about using some temperature measurements recently performed on various Au nanostructures is given to compare different thermometers measuring on different gold particles.

### 2.3.2.1 Optical property of Au NRs on glass substrate

We show in **Figure 2.5** the absorption spectrum of gold NRs deposited (drop-coating) on a glass ($SiO_2$) substrate. As shown in the transmission electron microscope (TEM) image in the inset, they have a diameter d = 8.5 ± 1.2 nm and a length D = 94.1 ± 9.8 nm which gives an AR between 10 and 13. The absorption spectrum exhibits a broad peak between 1100 and 1600 nm which corresponds to the L-LSPR of the rods whereas the smaller peak below λ = 600 nm corresponds to their T-LSPR. The broadness of the L-LSPR peak is likely due to the inhomogeneous size distribution of the NRs, some of them being longer than others, and their AR varies between 10 and 13. This enlarges the global resonance on a 500 nm wide spectral window. The position of the L-LSPR peak is also in good agreement with other measurements recently performed on NRs with similar large AR.[88]

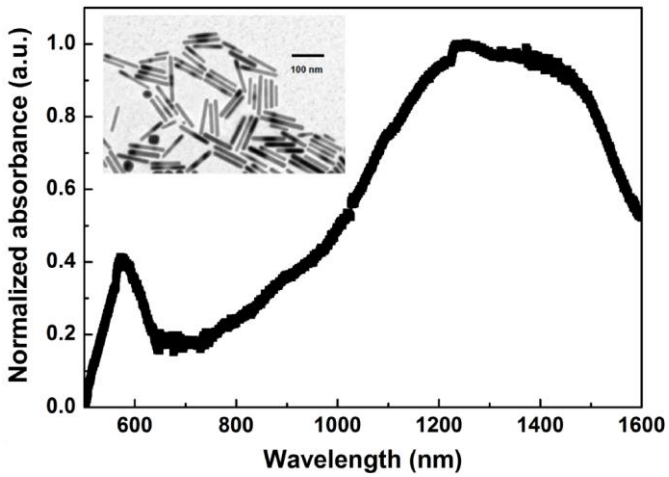


**Figure 2.5** *Absorbance of Au NRs drop-coated on a $SiO_2$ substrate. Inset: TEM picture of the NRs. They have an AR of ~10-13, and a L-LSPR peak between 1100 and 1600 nm.*

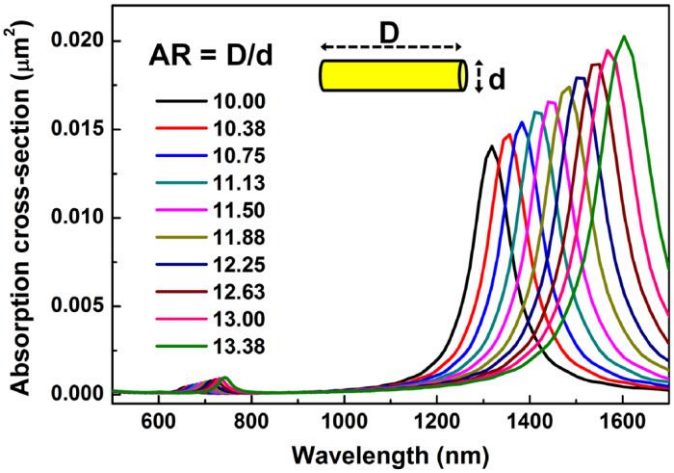


**Figure 2.6** *FDTD calculation of the absorption cross-section of isolated Au NRs on a $SiO_2$ substrate as a function of their AR. Their diameter (d) was fixed to 8 nm, and their length (D) is varied between 80 and 110 nm.*

To check the spectral position of the L-LSPR, we calculated by finite difference time domain (FDTD) the absorbance of Au NRs of different AR deposited on a $SiO_2$ substrate. The simulations were performed using Lumerical commercial software.[107] For the calculation, the Au NRs are placed on a $SiO_2$ substrate and are supposed to be isolated from each other. We consider that the incident source is a polychromatic plane wave, from 500 nm to 1700 nm, and polarized along the long axis of the Au NR. For the simulation region, the space-mesh size we applied is 1 nm in order to balance our calculation time and geometry description of these nanostructures. As shown in **Figure 2.6** the peak position is found to be in the same wavelength range than in the experiments, i.e. between 1300 and 1700 nm for an AR between 10 and 13. Note that if NRs are separated by only a few nanometers or even if they are in mechanical contact with each other, near-field coupling effects may appear and could shift the resonance furthermore toward the SWIR.[108] This means that NRs of smaller AR could have their resonance in the same wavelength range, and thus also contribute to the wide experimental absorbance spectrum of Figure 2.5.

### 2.3.2.2 Thermal and fluorescence experimental setup

To demonstrate the photothermal effect from our high AR Au NRs, we built an experimental set-up to measure the temperature changing by using a nanothermometer ($Er^{3+}$- doped $NaYF_4$ NC). This set-up for measuring the luminescence of $Er^{3+}$- doped $NaYF_4$ NC is shown in **Figure 2.7**(a). Excitation was performed with a continuous-wave infrared laser diode ($\lambda$ = 1537 nm) focused on the surface in a transmission mode on a 2 µm wide spot. After absorption by up-conversion, the laser radiation is emitted by luminescence in the visible range. The sample was set on a piezo-electric scanning stage (PI) for scanning. The fluorescence was collected by a large numerical aperture objective (Olympus, x100, N.A. = 0.8) and sent to a spectrometer (Jobin-Yvon, Triax) connected to a nitrogen-cooled CCD camera (Jobin-Yvon, Symphony). During a scan, a luminescence spectrum was measured at every position of the laser on the surface. The acquisition time was set to ~1 s per point. And the sample scanning and spectrum measurements were synchronized and driven with a homemade Labview program.

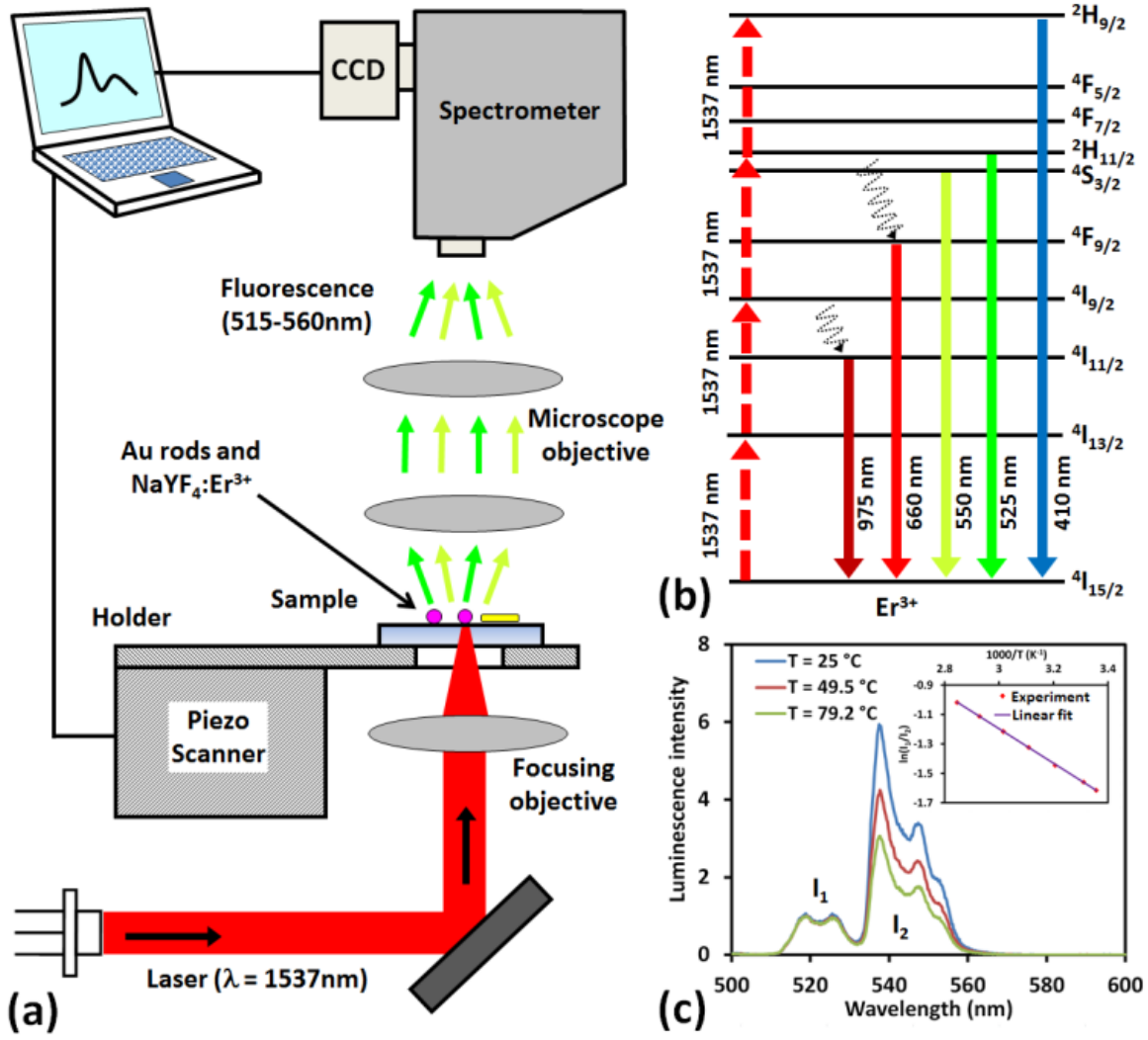


**Figure 2.7** *a) Experimental set-up for fluorescence measurements, b) energy band diagram and simplified energy transfers in $Er^{3+}$ ions excited at 1537 nm, c) luminescence spectra of $NaYF_4$: $Er^{3+}$ NC at 25°C, 49.5°C and 79.2°C. The inset shows the evolution of $ln(I_1/I_2)$ as a function of the inverse temperature.*

### 2.3.2.3 Temperature dependence of luminescence and calibration

The band diagram describing the energy transfers[109] and a room temperature (RT) luminescence spectrum of the $NaYF_4$:$Er^{3+}$ NCs excited at λ = 1537 nm are shown in Figure 2.7 (b) and (c) respectively. In our case, we are interested in two particular emission lines, located between 510 nm and 532 nm (green), and between 532 nm and 560 nm

(yellowish-green). The green line, further referred as $I_1$, comes from the transition from the excited $^2H^{11/2}$ state to the $^4I_{15/2}$ state. The yellowish-green line, ~5 times more intense at room temperature than the green one, and further referred as $I_2$, comes from the de-excitation from level $^4S_{3/2}$ to the ground state. The infrared excitation is non-linear and involves the absorption of several photons. However, the emitted luminescence intensity does not exactly scale as $P^n$ where $n$ is the number of photons ($n$ = 3 in the case of green emission) but rather as ~ $P^1$. This behavior has been studied recently and is explained by the relative difference between the decay rates of the intermediate and final energy levels during the up-conversion process.[110,111] It also depends on the power used for the excitation. Here, we are mostly concerned with the temperature dependence of the NC luminescence. Peaks $I_1$ and $I_2$ are linked to two transitions whose excited energy levels are in thermal equilibrium.[112–117] When the temperature increases, $^4S_{3/2}$ depopulates in favor of $^2H_{11/2}$, and this causes a relative decrease of $I_2$ with regard to $I_1$. The ratio $I_1/I_2$ is linked to temperature by the following relation: [112–117]

$$\frac{I_1}{I_2} = Ae^{-B/T} \qquad (2.1)$$

Where A and B are constants, T is the temperature in K, and $I_1$ and $I_2$ are the intensities integrated in the ranges [510-532] and [532-565]. From the intensity ratio of these peaks, and after a proper calibration, it is possible to retrieve the absolute temperature of the NCs. The evolution of the luminescence as a function of T is shown in Figure 2.7(c). For this calibration, the NCs were spin-coated on a Si substrate placed on a Peltier stage whose temperature was regulated and measured using a Pt100 thermoresistor. In that case, the laser excitation was achieved in the reflection mode at oblique incidence (not represented here). The evolution of $\ln(I_1/I_2)$ as a function of 1000/T is given in the inset of Figure 2.7(c). We fitted the experimental data with eq. (2.1) and determined the value of parameters A and B. A is a constant that depends on the environment near the NC and also on the excitation power. It requires to be slightly adjusted every time the sample or the power is changed. More information about the influence of the excitation power is given in chapter 2.3.2.5. B is the important parameter which rules the temperature dependence of luminescence. It is linked to the energy separation between the two peaks. From the fit shown in the inset of Figure 2.7 (c), we found A ≅ 10.1 and B = 1170 ± 100 K, in agreement with previous studies with similar $Er^{3+}$-doped NCs.[117,118]

### 2.3.2.4 Photothermal properties and heating capabilities of Au NRs

In order to study the photothermal properties of these high aspect ratio Au NRs and their heating capabilities at this excitation wavelength, we fabricated a sample made of only some tens of NRs concentrated in a small region on the $SiO_2$ substrate. To measure their temperature elevation following an external laser illumination, we used a single $NaYF_4$:$Er^{3+}$ NC as a nanothermometer deposited on their surface. A scanning electron microscope (SEM) image of the rods prior to the NC deposition is shown in **Figure 2.8**(a). The NRs are grouped in a 200 nm wide line. They are not oriented in the same direction although some of them are parallel and in contact with each other's. In Figure 2.8(b), we show the same NRs after the deposition of two NCs, deposited with a nanomanipulation system.[119] One NC (furthered referred as NanoA) was directly placed on the NRs and the other (further referred as NanoB) was positioned ~5 µm away on the $SiO_2$ surface. The role of NanoB is to act as a reference thermometer, insensitive to plasmonic heating.

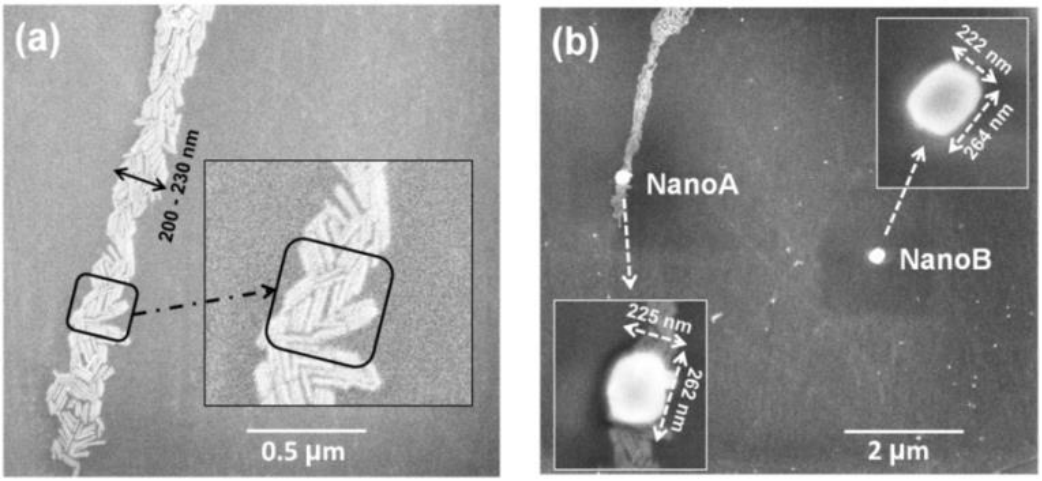


**Figure 2.8** *a) SEM picture of Au NRs deposited on $SiO_2$ substrate, b) SEM picture of the same zone after the deposition of two luminescent $NaYF_4$: $Er^{3+}$ NCs on the surface. NanoA is on the NRs and NanoB is 5 µm away from them.*

The surface was excited with the configuration shown in Figure 2.7. By moving the sample, we first scanned an area of 6 × 10 $\mu m^2$ that includes NanoA and NanoB. We show in **Figure 2.9**(a) and (b) the measured luminescence maps for an excitation power density of ~2 mW /

$\mu m^2$. The maps exhibit two bright spots corresponding to NanoA and NanoB [see the SEM picture in Figure 2.9 (c)]. Their size is limited by the diameter of the incident laser spot on the surface. Cross-sections extracted from the images are shown in Figure 2.9 (d). Luminescence was separated and integrated into two spectral zones, corresponding to $I_1$ and $I_2$. The intensity of $I_1$ is around 5 times smaller than $I_2$. From these images, we can see that Nano A and Nano B have roughly the same intensity in the $I_1$ spectral range. On the other hand, the intensity of NanoA in the $I_2$ spectral range is reduced compared to NanoB [see the red arrow in Figure 2.9 (d)]. This different behavior is an evidence of the heating induced by NRs located under NanoA. After absorption of light, the NRs transfer their heat to NanoA and this induces a relative decrease of $I_2$ compared to $I_1$. By dividing the image of Figure 2.9 (a) by the one of Figure 2.9 (b), we can map the ratio $I_1/I_2$ and convert it to a temperature scale using eq (2.1). The resulting temperature map and cross-sections are shown in **Figure 2.10** (a) and (b). For clarity, the zones in which there were no luminescence (outside NanoA and NanoB) were eliminated. The temperature of NanoA is found to be around 322 K whereas it remains near room temperature (RT) for NanoB.

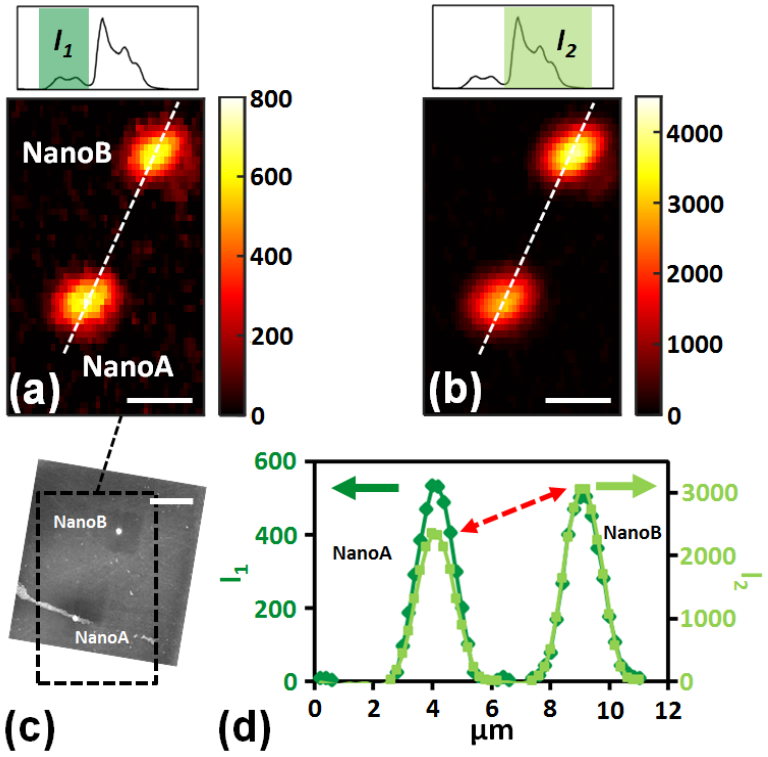


**Figure 2.9** *a) luminescence map around NanoA and NanoB in the $I_1$ spectral region, b) luminescence map of the same zone in the $I_2$ spectral region, c) SEM picture of the scanned zone, d) cross-sections extracted from a) and b). The excitation power density was 2 mW/$\mu m^2$. The scale bar is 2 µm.*

We also measured the temperature elevation of NanoA as a function of the laser power density without moving the sample [see Figure 2.10 (c)]. For a power density close to 3 mW/µm$^2$, we observed that T increases up to 332 K, i.e. ΔT = 34 K with respect to RT. More detailed calculation and calibration on these temperature data will be detailedly explained in chapter 2.3.2.5.

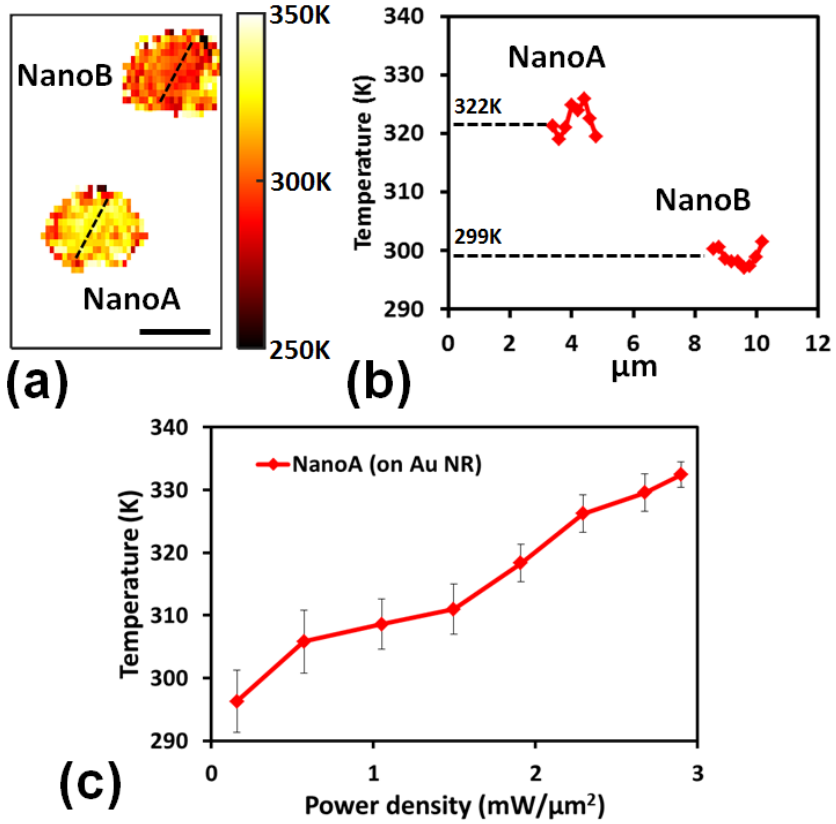


**Figure 2.10** (*a) Temperature map around NanoA and NanoB for an excitation power density of 2 mW/µm$^2$. (b) Cross-section extracted from a) showing the temperature increase of NanoA. (c) evolution of the temperature of NanoA as a function of the power density.*

## 2.3.2.5 Temperature determination in our measurement

To determinate the reliability of this nanothermometer and get an accurate temperature, we more detailedly describe here the influence of the temperature and the excitation power on the luminescence spectra of $NaYF_4$: $Er^{3+}$ NCs. When NCs are excited at 1537 nm, visible luminescence occurs after the absorption of three photons. We are interested in the green luminescence lines, located between 510 and 532 nm ($I_1$) and between 532 and 560 nm ($I_2$).

The two levels are in thermal equilibrium [(see **Figure 2.11** (a)]. When temperature is increased, the low energy level ($I_2$) depopulates toward the high energy one ($I_2$) [see the spectra shown in Figure 2.11 (b)]. The intensity ratio between these two lines $I_1/I_2$ depends on temperature with the simple relation:

$$\frac{I_1}{I_2} = Ae^{-\frac{\Delta E}{k_b T}} = Ae^{-B/T} \qquad (2.2)$$

For a given excitation power, $A$ is a constant than depends on the local environment like for instance on the optical properties of the surface it is located on. $B$ is another constant that depends on the Boltzmann constant and on the energy separation $\Delta E$ between the two levels.

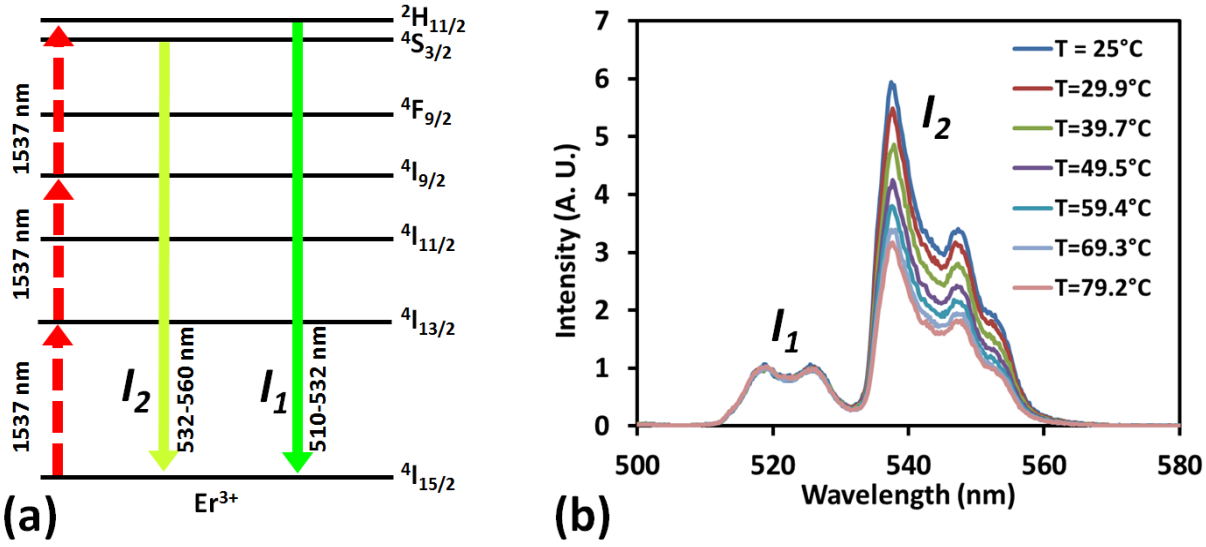


**Figure 2.11** *a) simplified energy level of $Er^{3+}$ ions, b) evolution of the luminescence spectra of $NaYF_4$: $Er^{3+}$ NCs as a function of temperature.*

We show in **Figure 2.12** the evolution of the intensity ratio $I_1/I_2$ and its logarithm $\ln(I_1/I_2)$ as a function of T and 1000/T respectively. The intensities are the integrated intensities in the ranges 510 - 532 nm and 532 - 560 nm. At room temperature $I_2$ 5 times larger than $I_1$. A linear fit with eq. (2.2) allows to extract $\ln(A)$ = 2.3 ($A$ = 10.1) and $B$ = 1170 K. At room temperature $I_2$ is ~5 times larger than $I_1$.

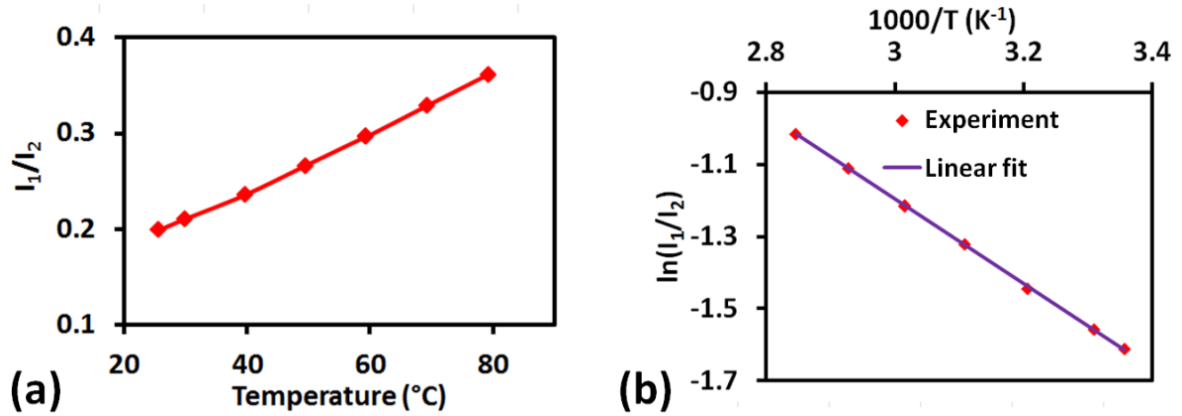


**Figure 2.12** *a) evolution of $I_1/I_2$ as a function of T, b) evolution of $\ln(I_1/I_2)$ as a function of 1000/T. The line is a fit with equation 2.2.*

The incident power density may also change the intensity ratio $I_1/I_2$. Indeed, it may influence the different energy transfers inside the NC and change the band filling. We observed this effect by measuring $I_1/I_2$ when the laser is focused on NanoB which is situated on the glass substrate (see Figure 2.8). The results are shown in **Figure 2.13** (a) together with the ones for NanoA.

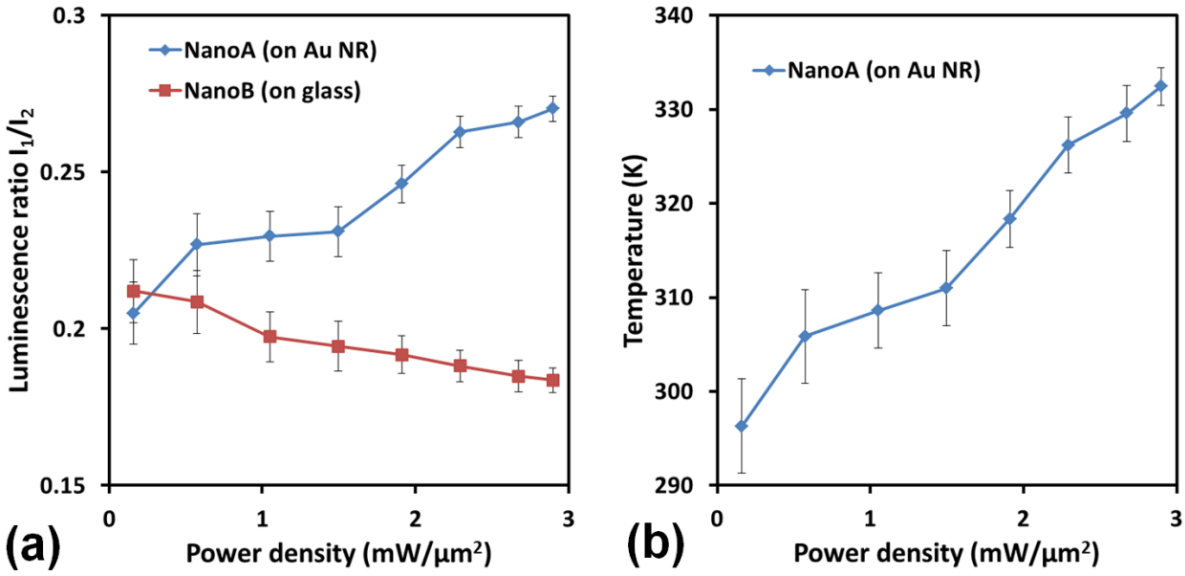


**Figure 2.13** *a) influence of the power density on the luminescence intensity ratio ($I_1/I_2$) of NanoA and NanoB, b) evolution of the temperature of NanoA as a function of the power density.*

When the NC is situated on the glass substrate, the intensity ratio $I_1/I_2$ diminishes a little bit when increasing the excitation power. This tendency is the opposite of that of the temperature which induces an increase of the ratio $I_1/I_2$. We had to take into account this effect in the determination of the temperature of NanoA. For that, we modified eq. (2.1) and eq. (2.2) by the following:

$$\frac{I_1}{I_2} = A(P)e^{-B/T} \qquad (2.3)$$

Where the constant *A* depends now on the incident power *P*. The determination of *A(P)* was made by fitting the evolution of $I_1/I_2$ made on NanoB as a function of P with a simple linear function. The results of the normalization are shown in Figure 2.13(b) [and labeled Figure 2.10(c) in the previous part]. This procedure allowed us to take into account the effect of the power density on $I_1/I_2$ into the determination of the temperature of the Au NRs.

### 2.3.2.6 Temperature elevation by numerical simulation

For a power density close to 3 mW/µm$^2$, we observed that the *T* of the nanoA increases up to 332 K, *i.e.* $\Delta T$ = 34 K with respect to RT. Knowing the pump power density, we tried to determine the temperature of the NRs from numerical simulations. Here, two models were tried to get some temperature values:

**Model 1** Temperature elevation from a single NR

We used a simple model described in ref 120. For a single NR excited by a laser beam, the NR temperature elevation $\Delta T$ can be estimated from the following equation:

$$\Delta T = \frac{\sigma_{abs} I}{4\pi\kappa R_{eq}\beta} \qquad (2.4)$$

Where $\sigma_{abs}$, *I*, and $\kappa$ are the absorption cross-section of the NRs, the power density, and the thermal conductivity of the surrounding medium, respectively. $R_{eq}$ and $\beta$ are parameters that

depend on the NR geometry.[120,121] For a NR with a respective length and width of 100 nm and 8 nm, we estimated by FDTD that $\sigma_{abs}$ = 0.01 μm$^2$ at $\lambda$ = 1.537 μm (see Figure 2.6). This value is an average value which takes into account the fact that the resonance of some of the heated NRs may be slightly shifted from the excitation wavelength. Since the transverse orientation does not absorb much, we divided $\sigma_{abs}$ by 2 and used 0.005 μm$^2$. From ref. 120 and 121, we calculated β = 1.62 and $R_{eq}$ = 1.05×10$^{-8}$ m. More difficult is an estimate of the thermal conductivity of the surrounding medium. The NRs are sandwiched between the glass substrate ($\kappa_{glass}$ ~ 1 W.m$^{-1}$.K$^{-1}$) and the $NaYF_4$ NC for which no exact value of $\kappa$ *is* available. Regarding the thermal conductivity of the surrounding medium, we used an effective thermal conductivity[122] which takes into account the one of the substrate ($\kappa_{glass}$ ~ 1 W.m$^{-1}$.K$^{-1}$) and the one of the air ($\kappa_{air}$ ~ 0.024 W.m$^{-1}$.K$^{-1}$). We neglected the presence of the nanocrystal which is of finite size and isolated in air above the NRs and used $\kappa = (\kappa_{glass} + \kappa_{air})/2$.

For a power density ($I$) of 3 mW/μm$^2$, we calculated with eq. (2.4) a temperature elevation $\Delta T$ = 137 K, which is 4 times larger than our experimental value ($\Delta T$ = 34 K). The difference is not surprising and can be explained by several reasons. As mentioned before, the value of $\kappa$ is the prevailing source of error since $\Delta T$ is inversely proportional to it. However, it cannot fully explain the difference. Another important reason is that what we measure is the average temperature of the NC. Since its size is ~ 230 nm (confirmed from the SEM image as shown in Figure 2.8), $T$ may not be homogeneous inside, with a negative gradient between its lower part directly in contact with the NRs and its top part that extends in free space. Finally, $T$ may also be different between the NC and the NRs simply by considering the nature of the heat transfer channels involved in the thermalization process. Two heating paths are possible here (**Figure 2.14**), one by direct contact, and the other one by conduction through the air gap in the interstices or laterally by the sides. The relative importance of such channels depends on the size of the interstices between the NRs and the NC, and on the roughness of the interfaces. The presence of an interfacial thermal resistance between the two bodies can also alter the efficiency of the heat transfer by direct contact. These issues are well known in nanothermics and in scanning thermal microscopy where the measured temperature is the one of the probe, not that of the sample.[123]

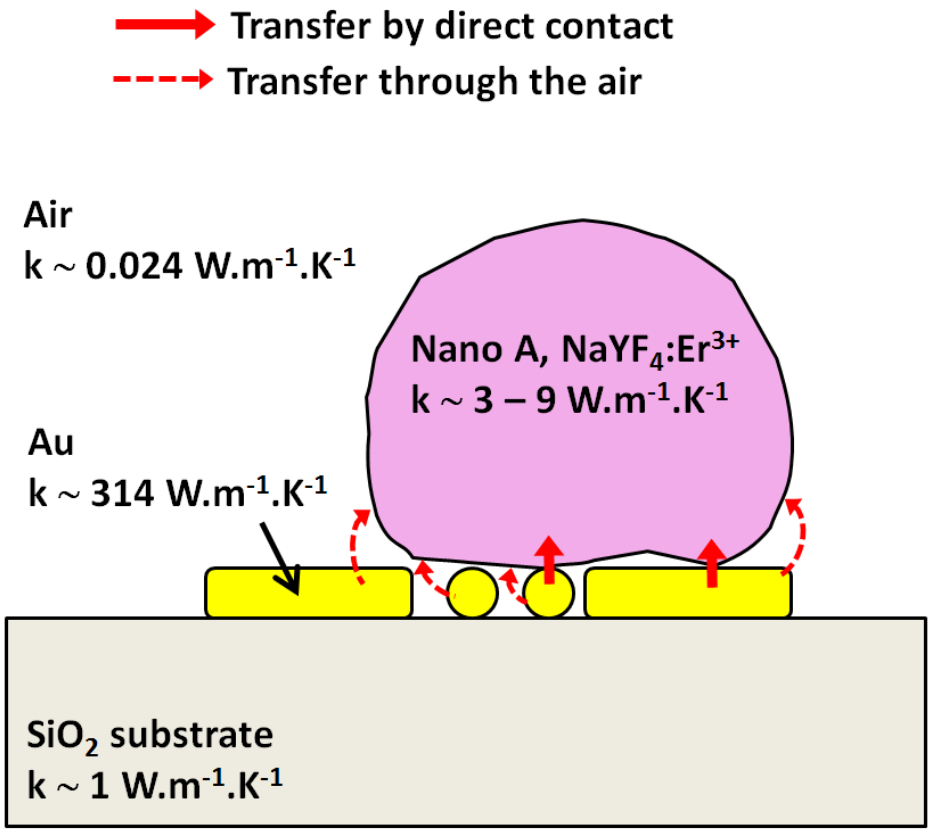


**Figure 2.14** *Illustration of the different heat transfer channels between the NRs and the fluorescent nanocrystal.*

**Model 2** Temperature elevation from an array of NRs

Since we are dealing with several NRs, we also tried to use a model which takes into account the presence of several NRs close to each other and that all of them contribute to the heating.[124] Here, an estimation of the collective temperature increase of an infinite array of NRs for a Gaussian illumination beam is given by the expression:[124]

$$\Delta T_0^{ext} \approx \frac{\sigma_{abs} P}{\kappa} \sqrt{\frac{ln2}{4\pi}} \frac{1}{HA} \qquad (2.5)$$

Where $P$ is the laser power, $H$ is the full width at half maximum of the beam, $A$ is the area of a unit cell of the NR lattice and $\sigma_{abs}$ and $\kappa$ stand for the absorption cross section of the NRs and the thermal conductivity of the surrounding media respectively. In our case, the NRs do not form an infinite array, so we take $H$ = 200 nm which corresponds to the width of the NRs

line (see the SEM image in Figure 2.8) and $A = 10^{-15}$ m$^2$ which corresponds to an area of 200 × 200 nm$^2$ divided by the number of NRs (~40). Here, as we did in model 1, we used 0.005 μm$^2$ as the $\sigma_{abs}$. Regarding the thermal conductivity of the surrounding medium, we used an effective thermal conductivity[122] $\kappa = (\kappa_{glass} + \kappa_{air})/2$. Using $P = I \cdot \pi (H/2)^2$, where $I$ is the power density ($I$ = 3 mW/μm$^2$), we find $\Delta T$ = 1079 K which is more than one order of magnitude larger than what we measure and is above the melting temperature of the NRs. This discrepancy can be explained by two main reasons. First, the absorption cross section we calculated concerns an isolated NR. Here, since several NRs are close to each other, near-field effects can occur and modify it significantly. A decrease of the absorption cross section would decrease the temperature. Second, as we explained in model 1, there is possibly a difference between the NRs temperature and the NC one, which makes a thermal resistance between the two bodies can also alter the efficiency of the heat transfer by direct contact.

By the simulations above, we can see that either the simple model for an isolated nanorod or a more complex model which takes into account several rods are not adapted to describe our experiment. For determining the real temperature of the NRs, more complex simulations, made by a fine element method, are necessary, but is not the scope of my work. Here, the simple analytical simulation confirmed us that the temperature elevation occurred and is probably larger than what is measured, showing the efficient photothermal effect of high AR NRs at this excitation wavelength.

### 2.3.2.7 Comparison with other measurements

**Table 2.2** *Comparison of previous temperature measurements performed on Au nanostructures. λ: Heating wavelength; ΔT : Temperature elevation.*

| **Au nanoparticle** | **Thermometer** | **Surrounding** | **Laser power** | **λ(nm)** | **ΔT (K)** | **Ref** |
|---|---|---|---|---|---|---|
| Au nanosphere | Simulation | Water | 1 mW/μm$^2$ | 530 | 50 | [120] |
| Au nanosphere | Refractive index of surrounding medium | Water/glass | 1 mW/μm$^2$ | 488 | 60 | [125] |
| Au nanosphere | Ice phase transformations | Water | $4\times10^4$ W/cm$^2$ | 520 | 6 | [126] |
| Au nanorod | Perylene | Polymer | 8 mW/cm$^2$ | 800 | 60 | [127] |
| Au nanosphere | $NaGdF_4$: $Yb^{3+}$: $Er^{3+}$ | Water | 198.3 mW | 980 | 20 | [128] |
| Au nanorod | $NaYF_4$:$Yb^{3+}$:$Er^{3+}$ | Liquid | / | 980 | ~ 9 | [129] |
| Au nanorod | Fluorescein | Air/glass | 20 mW | ~ 770 | ~ 3 | [130] |
| Au nanorod | $NaYF_4$:$Er^{3+}$ | Air/glass | 3 mW/μm$^2$ | 1537 | 34 | This work |

Here, we also compare our Au NRs with other Au nanoparticles, such as Au nanosphere[120,125,126,128] and other Au NRs with different aspect ratio[127,129,130]. We summarize them in **Table 2.2.** Although they are measured under different surroundings and laser-excitation conditions by different thermometers, efficient photothermal effect (Temperature elevation: ΔT), from a few to tens of degrees, is obvious in these Au nanoparticles. Compared to some complex systems[125,126], luminescent nanothermometers (NTs), particularly the lanthanide (Ln) doped UCNPs have a wider application in different surroundings, such as $NaGdF_4$: $Yb^{3+}$: $Er^{3+}$ (Ref. 128), $NaYF_4$:$Yb^{3+}$:$Er^{3+}$ (Ref. 129) and $NaYF_4$:$Er^{3+}$ in this work. It is worth mentioning that, to our knowledge, nano-heating measurements have been performed only in the visible and NIR range (< 1000 nm). For SWIR range (> 1000 nm) and high aspect ratio Au NRs, the quantitative analysis of their nano-heating capacity is still rare. In addition, the temperature elevation in this work is measured via using a single $NaYF_4$:$Er^{3+}$ NC as a

nanothermometer. An interesting aspect of this configuration is that the 1.537 µm laser used for heating the Au NRs is the same than the one that excites the fluorescence of $Er^{3+}$ ions. This very simple mode of operation makes the combination Au-NRs/$NaYF_4$:$Er^{3+}$ NC a very powerful and versatile heater/temperature sensor.

### 2.3.2.8 Summary of photothermal properties

We investigated the photothermal properties of high aspect-ratio Au NRs (AR >10). They possess a L-SPR in the SWIR region near 1.5 µm, and can be easily excited with an inexpensive SWIR laser diode. We measured the temperature elevation of a few NRs by depositing a single $Er^{3+}$ doped $NaYF_4$ NC on their surface. At a moderate power of 3 mW/$\mu m^2$, we measured a temperature elevation of 34 K on this nanothermometer. This temperature is smaller than the one we calculated by a simple analytical model but it shows the good capabilities of such nanostructures for achieving a local heating at this excitation wavelength. Applications can be found in the domain of photothermal therapy in the third biological window, or for designing cheap near-infrared detectors that use photothermal effect. The association nanorod/nanocrystal constitutes also a very efficient heater/temperature sensor. In order to gain in sensitivity and temperature accuracy, it would be interesting to use smaller luminescent nanocrystals directly chemically attached to nanorods for ensuring a good thermal transfer.

## 2.3.3 Au NRs/NTC-thermistor photodetector

Since we have shown that the photothermal effect of Au NRs is efficient, what we need to do is detecting and measuring the energy, here formed as heat. About the heat from plasmonic-induced Au nanoparticles, an important application is photothermal therapy (PTT) as we mentioned in chapter 1. This approach is an extension of photodynamic therapy, in which a photosensitizer is excited with specific band light. This activation brings the sensitizer to an excited state where it then releases vibrational energy (heat), which is what kills the targeted cells.[131] However, in our case, we want to detect the heat, then to realize the photodetection. Like what we did in chapter 2.3.2, UCNP succeeded in detecting the change

of temperature from the photothermal effect of Au NR, but the Au NRs + UCNP is a complicated system, which cannot be a photodetector. At this point, we came up with some thermistors, which have been in widely using in our daily life and industrial manufacturing for many years due to their simple structure, low price, high reliability and convenient maintenance. Thus, we next describe how we tried to combine the Au NRs and the thermistor as a hybrid device to form an innovative SWIR photodetector.

### 2.3.3.1 Au-NR/NTC-thermistor hybrid device architecture

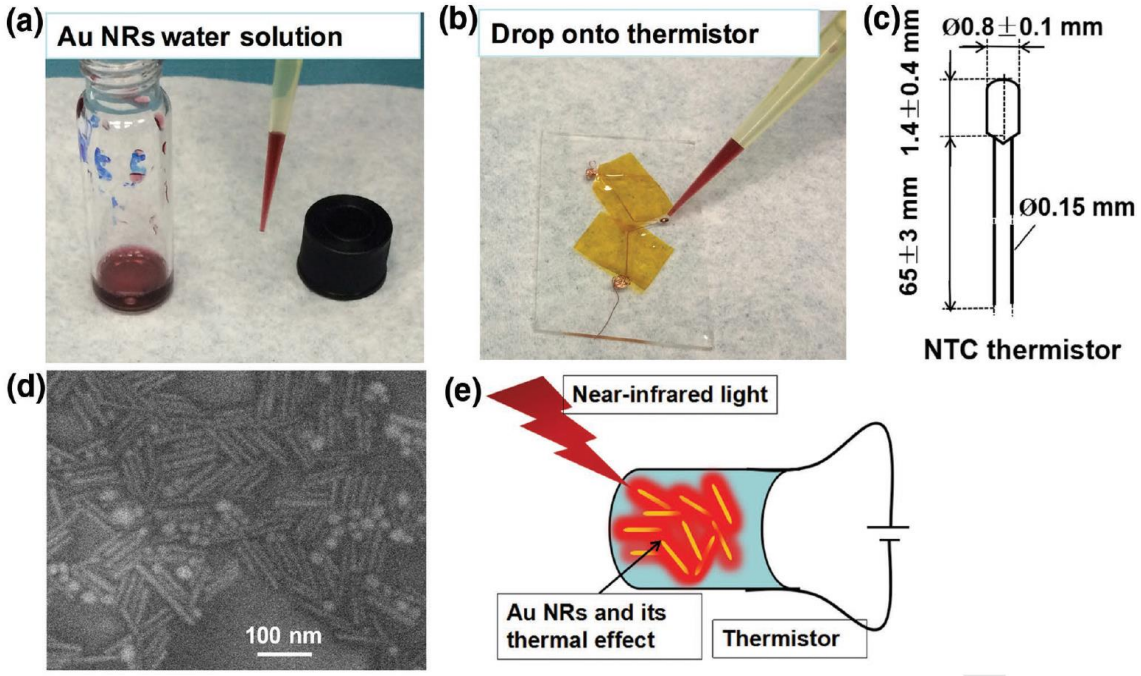


**Figure 2.15** *(a) Au NRs in water (sample h of Table 2.1). (b) Image showing a NTC thermistor fixed on a glass slide. Au NR water solution was drop-casted onto the thermistor. (c) The dimension of the thermistor applied in this work. (d) SEM image of the Au NRs-coated thermistor exhibiting mostly Au NRs on the surface of the hybrid device. (e) A schematic describing the hybrid Au-NRs/thermistor device structure to harvest the photothermal effect of Au NRs for SWIR sensing.*

Firstly, to demonstrate the remarkable photothermal effect of Au NR, as a proof-of-concept, we used a low-cost negative temperature coefficient (NTC) thermistor with a room-temperature (25 °C) resistance of 10 kΩ (Series B57540G1 from TDK EPCOS).

As-synthesized Au NRs in water (with a concentration ranging from 0.6 to 7.2 g $L^{-1}$) was drop-casted directly to coat the thermistor surface leading to the formation of a hybrid Au-NRs/thermistor device (**Figure 2.15**). The optimization experiments on Au NRs solution concentration, different thermal devices and different size of Au NRs are listed in **Chapter 5.1 Annex I.**

In order to perform sensing in the SWIR spectrum, we selected the sample h of Table 2.1 with a L-LSPR maximum at 1300 nm to fabricate such Au-NRs/thermistor hybrid devices. Scanning electron microscopy (SEM) characterization, carried out directly on the Au NRs-coated thermistor, confirmed the thermistor surface coating to be dominated by Au NRs (Figure 2.15d). In such a hybrid configuration, Au NRs serve as the photon absorption agent and generate heat as a result of the decay of LSPR excitation. This leads to a drop of the resistance of the NTC thermistor which is in contact with Au NRs and the variation of resistance can be probed by simple electrical measurements (Figure 2.15e).

### 2.3.3.2 Photoresponse under monochromatic illumination

We then applied a series of monochromatic illuminations ranging from 1.0 µm to 1.8 µm and we studied the photoresponse of the hybrid Au-NRs/thermistor (**Figure 2.16**). This series of monochromatic illumination were generated by a quartz halogen lamp, a monochromator and relevant filters. (Experiment set-up is shown in Chapter 5.1 Annex I) The density of illumination, determined by the lamp and the grating of the monochromator, was calibrated to be from 0.16 $mW/cm^2$ (at 1800 nm) to 0.35 $mW/cm^2$ (at 1300 nm). Under each monochromatic illumination, a "control device" containing only the thermistor (without Au NRs) was equally experimented and we observed limited photoresponse at the whole wavelength range (grey curves of Figure 2.16a). In these experiments, the illumination applied is of relatively low intensity and therefore negligible photo-induced heating effect was observed on the control device. By comparison, under the same illumination condition, hybrid Au-NRs/thermistor exhibit a clear photoresponse revealed by a photo-induced resistance drop (Figure 2.16a). Here the existence of Au NRs on the surface of the thermistor and their photothermal effect enable a measurable photoresponse in the hybrid device in a form of resistance variation. The response time of the hybrid device can be characterized by the rise

and decay time, respectively defined here as the time used by the resistance to drop from its room-temperature value to 70% of the saturation level (when illumination is on) and the time used by the resistance to increase back to 70% of its room-temperature value (when illumination is off). As shown in Figure 2.16b, both the rise and decay time of the hybrid device are less than a few seconds. After normalizing the photo-induced resistance drop by the intensity of the illumination, we obtained the responsivity (in Ω/W) of the hybrid device over the whole wavelength window tested. From the datasheet of the thermistor we obtained the corresponding responsivity in °C/W. As shown in Figure 2.16c, in the wavelength window experimented, the maximum photoresponsivity of hybrid Au-NR/thermistor devices shifted slightly from $\lambda$ = 1.3 μm to 1.4 μm when a more concentrated Au NR solution was applied. For devices fabricated by relatively diluted Au NR solutions (e.g., 0.6 g/L and 1.2 g/L), the responsivity peak wavelength is in good agreement with the L-LSPR maximum of the Au NRs applied. For devices fabricated by a more concentrated Au NR solution (4.8 g/L), the dense packing of Au NRs may lead to the observed redshift of the responsivity maximum. Besides the slight redshifting of the responsivity maximum, the responsivity magnitude of the hybrid devices increased as the Au NR solution concentration increased from 0.6 g/L to 4.8 g/L. This is coherent with the fact that more Au NRs are available on the thermistor surface to exercise their nanoheater function when a more concentration Au NR solution was applied. With a further increased concentration (> 4.8 g/L), however, we started to observe a decrease of hybrid device performance, likely due to the increased limitation of heat transfer from very dense Au NRs clusters to the thermistor. The most optimized hybrid device, fabricated by 4.8 g/L Au NR solution, exhibited a maximum photoresponsivity of $4.44 \times 10^7$ Ω/W at $\lambda$ = 1.4 μm (0.28 mW $cm^{-2}$).

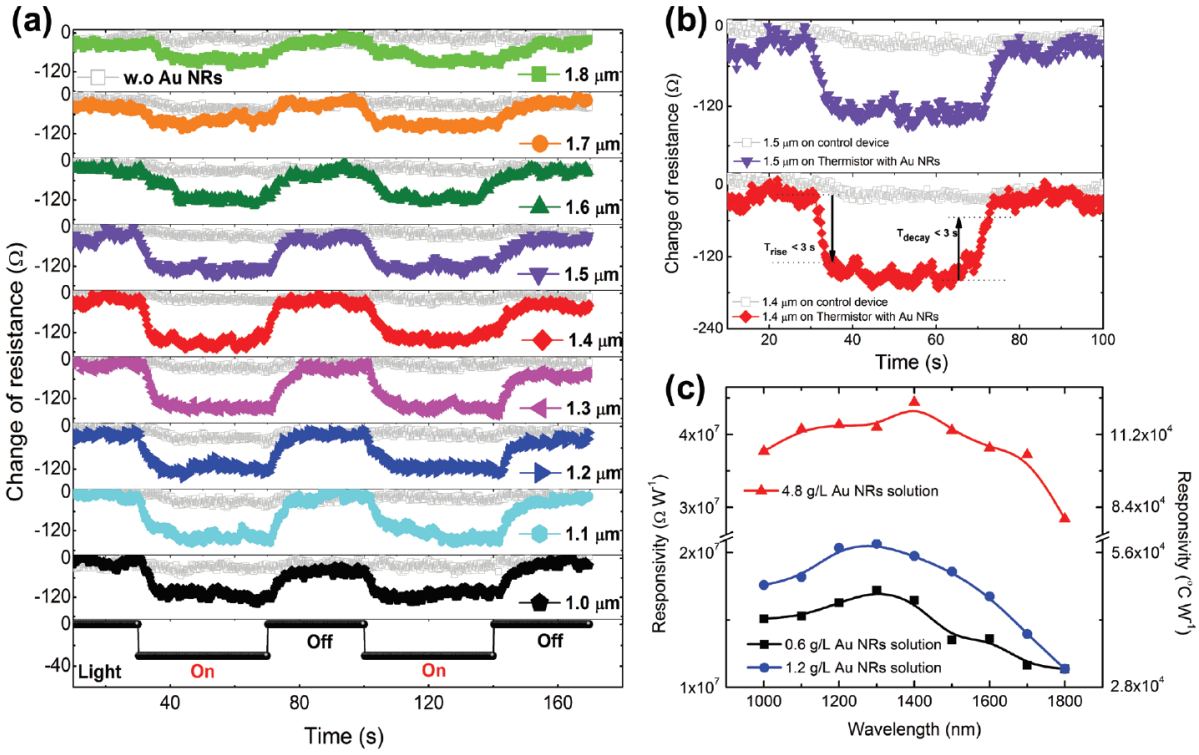


**Figure 2.16** *(a) Photoresponse characteristics over time of a hybrid Au-NRs/thermistor device (fabricated by 4.8 g/L Au NRs solution) in the form of photoinduced resistance drop upon exposure of monochromatic illumination (λ from 1.0–1.8 μm). Gray curves with open symbols represent the photoresponse from a control device without Au NRs. (b) Zoom-in view of the photoresponse characteristics in (a) under 1.4 and 1.5 μm illumination exhibiting the time scale of the response speed. Right-hand-side Y-axis represents the current measured under a direct current (DC) bias of 1 V. (c) Zoom-in view of the photoresponse characteristics in (a) under 1.4 and 1.5 μm illumination exhibiting the time scale of the response speed. Right-hand-side Y-axis represents the current measured under a direct current (DC) bias of 1 V.*

### 2.3.3.3 Photoresponse under 1.5 μm Laser

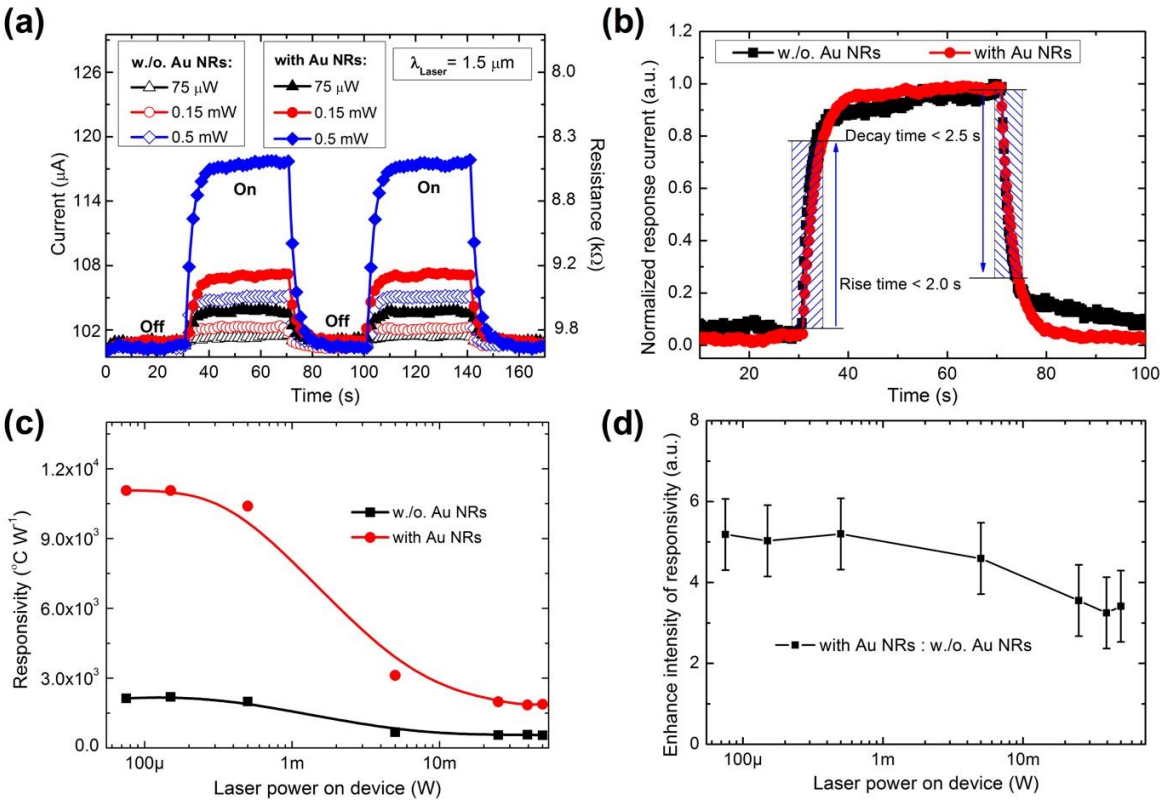


**Figure 2.17** *(a) Photoresponse characteristics over time of both the control device (thermistor without Au NRs) and the hybrid Au-NR/thermistor device (fabricated by 4.8 g/L Au NR solution) under the illumination of a laser (λ = 1.5 μm) focused on device. The photoresponse is presented in the form of photo-induced resistance drop (W, right Y axis) or in photo-induced change of measured current under a DC bias of 1V (Amperes, left Y axis). (b) Normalized of photoresponse characteristics (in measured current) comparing the control and the hybrid device under the illumination of a laser (λ = 1.5 μm, 0.5 mW, focused on device). Current was measured under a DC bias of 1V.The response time was measured from 0% to 80% and from 100% to 20% for rise time and decay time, respectively. (c) The evolution of the photoresponsivity (in °C/W) under the illumination of a laser (λ = 1.5 μm) of the control and the hybrid device over different laser powers experimented. (d) The enhancement ratios calculated from the photoresponsivity (shown in c) of the hybrid device over the control device (without Au NRs) at different laser powers.*

In order to understand the process which limits the response speed of these types of hybrid Au-NRs/thermistors, on the most optimized hybrid device fabricated by 4.8 g/L Au NR solution, we further studied their photoresponse characteristics under larger illumination intensities (by a laser diode illumination at λ = 1.5 μm). In these experiments a laser spot was

focused onto the surface of the hybrid device. Various laser powers ranging from 75 μW to 50 mW were experimented (which corresponds to a power densities ranging from 6.7 mW/cm$^2$ to 4464.3 mW/cm$^2$). In this case, as the illumination intensity is relatively high, on a control device (thermistor without Au NRs) we can already observe a response due to the laser-induced heating detected by the thermistor (**Figure 2.17a**).

By comparison, the existence of Au NRs on the surface of hybrid Au-NRs/thermistor devices enables a clear enhancement of photoresponse (curves with solid symbols in Figure 2.17a). After normalizing the response characteristics of the control device and the hybrid device, near-identical rise and fall time, on the scale of 2 s, were observed on both devices (Figure 2.17b). This suggests that the limitation of response speed of the hybrid device does not originate from the photothermal effect of Au NRs or from the heat-transfer processes between the Au NRs and the thermistor. Instead, the limitation of response speed comes from the response speed of the thermistor itself. This suggests that the hybrid Au-NRs/thermistor device can potentially exhibit a shorter response time if a more performing thermistor is applied in the hybrid device structure. The photoresponsivity (in °C/W) of both the control and the hybrid device at each experimented laser intensity was shown in Figure 2.17c. In particular, the hybrid device exhibited a remarkable responsivity enhancement compared to the control device for up to 5.19-fold enhancement at 0.5 mW laser illumination. For both control and hybrid devices, the photoresponsivity decreases as the laser power increases. From previous studies,[132,133] we do not expect the absorption of Au NRs saturates at the current laser intensity window. After extracting the enhancement ratio from the responsivity of the hybrid over the control device, one observed that the enhancement ratios are roughly of the same order of magnitude over the whole laser power window experimented (Figure 2.17d). This suggests that the decrease of responsivity along with increasing laser power originates again from the thermistor itself. Au NRs here in the hybrid device serve as a sensitizing agent either enabling SWIR photodetection when the illumination intensity is low ($\leqslant$0.35 mW cm$^{-2}$, the case of Figure 2.16) or boost the photoresponsivity when the illumination intensity is high (the case of Figure 2.17). From the data sheet of the thermistor it is possible to obtain the magnitude of photo-induced temperature change corresponding to the resistance change under each laser power experimented (**Figure 2.18**). By subtracting the temperature change observed in the control device from that of the hybrid device, we estimated that the laser-induced temperature increase contributed from the Au NRs can be as high as 66 °C at a

laser power of 50 mW (λ = 1.5 µm). (Relationship between resistance and temperature is shown in Chapter 5.1 Annex I)

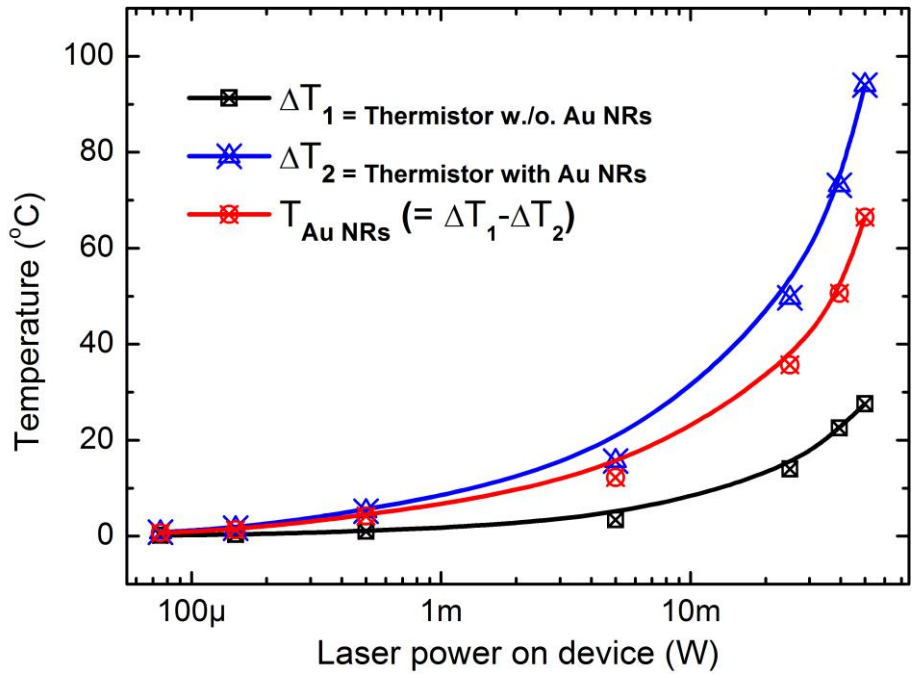


**Figure 2.18** *Evolution of the photoinduced temperature change over laser power of the control (black curve) and the optimized hybrid Au-NRs/thermistor device fabricated by 4.8 g/L Au NRs solution (blue curve) under the illumination of a laser (λ = 1.5 µm) that was focused on device. Red curve shows the contribution from Au NRs.*

### 2.3.3.4 Summary of Au-NRs/thermistor photodetectors

Started from colloidal synthesis, we prepared a series of uniform solution-processed Au NRs of various ARs (aspect-ratios) exhibiting a strong and well-defined L-LSPR maximum from 900 to 1.3 µm. A hybrid device structure, composing of Au NRs on the surface of a NTC-thermistor, was proposed as an alternative low-cost approach for sensing in the SWIR spectrum. Under a monochromatic illumination of relatively low intensity (< 1 mW/cm$^2$), hybrid Au-NRs/thermistor devices exhibit a clear photoresponse in the form of photo-induced resistance drop in the wavelength window from 1.0 µm to 1.8 µm. This is in contrast to the control device (thermistor alone without Au NRs), the photoresponse of which is negligible under the same illumination condition. The photo-responsivity of the hybrid device reaches a

maximum value of $4.44\times10^7$ Ω/W at 1.4 μm, a wavelength in agreement with the L-LSPR maximum of the Au NRs applied. At higher illumination intensities (from 6.7 mW/cm$^2$ to 4464.3 mW/cm$^2$) achieved by a laser (λ = 1.5 μm) focused onto device, due to the laser-induced heating photoresponse was observed in both the control and the hybrid device. Nevertheless, in this case hybrid devices exhibited more than 5-fold enhancement of photoresponsivity by comparison to the control device.

In summary, the plasmonic-induced photothermal effect of Au NRs (i) enables the photo-sensing capability in a hybrid Au-NRs/thermistor device structure under relatively weak illumination and (ii) boost the photo-response of the hybrid device when illumination intensity is high. The response speed of the current Au-NRs/thermistor hybrid device is as short as 2 seconds, limited by the response speed of the thermistor itself. Optical sensing in the SWIR spectrum is a challenging task, the current approach harvesting the photothermal effect of solution-processed colloidal Au NRs thus represent a new path towards alternative and low-cost SWIR sensing.

### 2.3.4 Au-NRs/Pt photodetector

In our previous work, for the first time, we proposed a hybrid device structure coupling colloidal plasmonic Au NRs with a commercially available thermistor to achieve low-cost SWIR photon sensing.[134] These Au-NRs/thermistor devices exhibited clear photo-response in the wavelength window between 1.0 to 1.8 μm. Yet, their response speed remains slow (rise/decay time = ~ 2 s) which was limited by the response time of the thermistor itself. A temperature sensor with a much faster response speed would be necessary to access the full potential of the photo-thermal effect of Au NRs.

In this part, we propose a new hybrid SWIR photodetector structure based on the coupling between a resistive platinum (Pt) microwire and colloidal plasmonic Au NRs which is capable to reduce the photoresponse time of more than *four orders of magnitudes* compared to our previous work. Pt was chosen here due to its large temperature coefficient of resistance, wide operation temperature range and high stability. The combination of these characteristics has led to the extensive applications of Pt as a resistance temperature detector (RTD).[135–138] Here

a series of Pt microwires of various dimensions were fabricated and applied to harvest the photothermal effect of Au NRs in an Au-NRs/Pt hybrid device structure. We anticipate that these hybrid Au-NRs/Pt photodetectors would be able to provide a fast conversion between SWIR photons, heat, and resistance change. This device structure maybe represent a brand-new strategy for SWIR photodetection alternatives, meeting the needs of emerging applications demanding reduced fabrication cost and high operation speed.

### 2.3.4.1 Pt micro-wire RTD and Au-NR/Pt device architecture

To fabricate resistance temperature detectors, a series of Pt microwires with different lengths (from 1.5 mm to 10 µm) and widths (from 200 µm to 2 µm) were defined by photolithography on quartz coated glass substrates. Colloidal Au NRs dispersed in water with an optimized concentration (4.8 g/L) were deposited onto the surface of a Pt RTD. The preparation process is described in **Figure 2.19**a and **Figure 2.20**.

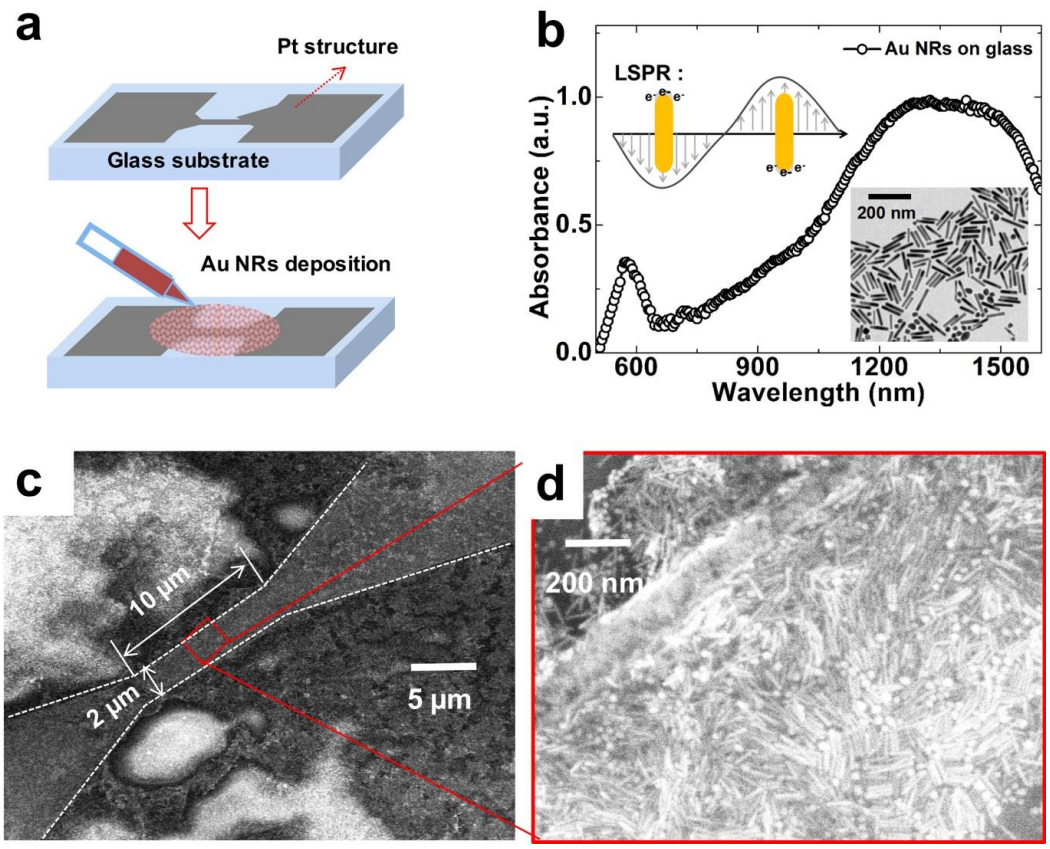


**Figure 2.19** *Device fabrication, optical characteristics of colloidal Au NRs and the morphology of Au-NRs/Pt device. (a) Schematic of the deposition process of a drop of Au NRs solution onto the surface of a Pt microwire RTD device. (b) Optical absorbance spectrum of a film of Au NRs on a glass substrate (the upper inset shows a schematic of the longitudinal*

*surface plasmon resonance (LSPR) of Au NRs; the lower inset shows a TEM image of these Au NRs). (c) SEM image of an Au-NRs/Pt device with a 10 µm by 2 µm Pt microwire. (d) Zoom-in SEM image of the device permitting the visualisation of Au NRs on the Pt microwire.*

The optical absorbance of Au NRs deposited on a glass substrate reveals strong absorption in the wavelength range between 1200 nm and 1600 nm (Figure 2.19b) which originates from the longitudinal surface plasmon resonance (LSPR) of these high aspect-ratio Au NRs. As observed in transmission electron microscopy (TEM) characterizations (insert of Figure 2.19b), these Au NRs are relatively monodisperse with an average rod length of 94 ± 13 nm, an average rod diameter of 8.5 ± 1.5 nm, and an aspect-ratio of ~ 11. Scanning electron microscope (SEM) characterizations were carried out on a typical Au-NRs/Pt device (Figure 2.19c and d). A dense layer of Au NRs was observed on the Pt microwire RTD (Figure 2.19d).

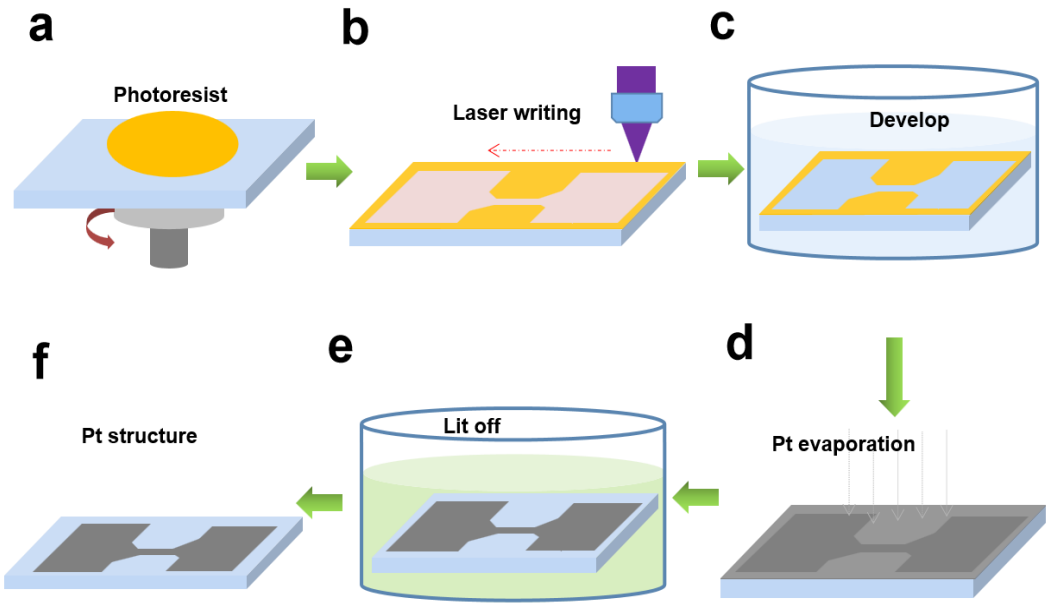


**Figure 2.20** *Detailed fabrication process for the platinum (Pt) microwire resistance temperature detector (RTD) devices. (a) spin-coating a layer of adherence promoter (TI from microchemicals) and a layer of photosensitive resin (AZ5214, microchemicals). (b), patterns with various dimensions were then defined by direct laser writing lithography (Heidelberg Ins. laserwriter µPG101). (c), substrates were then developed by dipping the sample in a bath of developer (AZ726 MIF, microchemicals) with subsequent DI water rising and air-drying. (d), a Ti (5 nm)/Pt (40 nm) layer was evaporated onto the sample by an e-beam evaporator (Plassys MEB550S). (e), the sample was lifted-off by immersing samples into a bath of acetone. (f), Pt RTD device was formed after acetone-washing and air-drying.*

### 2.3.4.2 Optimizing the Au-NR/Pt hybrid devices

We fabricated and characterized various Pt microwires with different widths and lengths and we studied the impact of them on the time-dependent photoresponse characteristics of Au-NRs/Pt devices. Indeed, the size of the microwire is supposed to strongly influence the heat dissipation in similar structures: Joule heating in metallic nanowires, in which, the decay time is linearly dependent on the temperature coefficient and both increase to saturation values with the increasing wire width.[139] In order to verify the infection of Pt wire's size on response time, we first fabricated a series of microwires with a fixed length (1500 μm) but a variable width (from 200 μm to 2 μm) as large size Pt RTD devices. Au NRs were drop-coated on these Pt wires to form Au-NRs/Pt hybrid devices, a λ=1.5 μm laser (laser spot: 1000 μm) was focused on these devices to measure their response time. The rise time and the decay time were measured from 0% to 80% and from 100% to 20%, respectively. A faster response was observed when the width is smaller (as shown in **Figure 2.21a** and **Table 2.3 left**). This means that smaller devices are more sensitive to the temperature variation from Au NRs. Therefore, we fabricated and characterized much shorter devices (width = 2 μm) where we varied the length from 150 μm to 10 μm (small size Pt RTD devices). As we did on large size devices, Au NRs were drop-coated on these Pt wires to form Au-NRs/Pt hybrid devices, a λ=1.5 μm laser (laser spot: 10 μm) was focused on these devices to measure their response time. We observed a similar result: The response becomes faster when the length is smaller (Figure 2.21b and Table 2.3 right). As summarized in Table 2.3, the narrower of the width (from 200 μm to 2 μm) and the shorter of the length (from 150 μm to 10 μm) in these Au-NRs/Pt hybrid devices lead to a faster photoresponse. This optimizing process means that the size of the Pt wires determines the optical response speed under existing conditions, and it shows us an optimized device size: length = 10 μm and width = 2 μm.

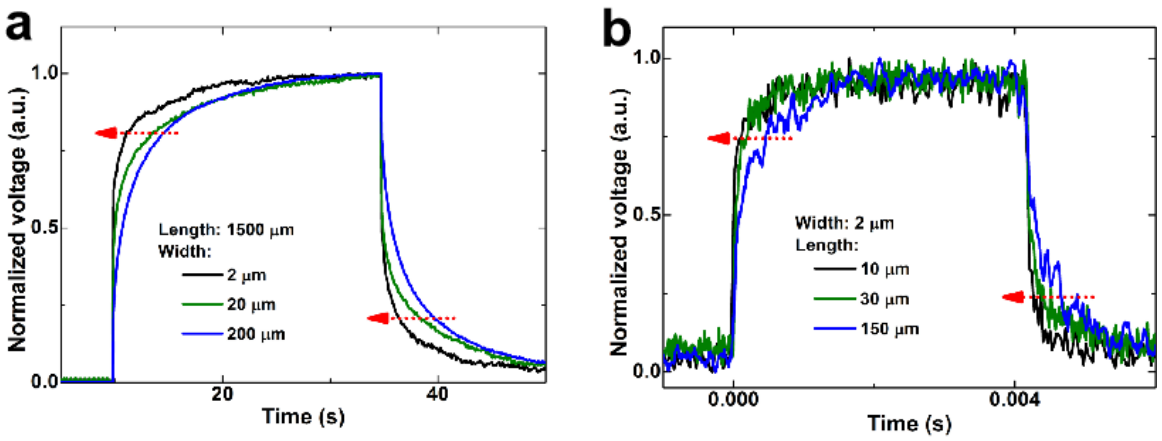


**Figure 2.21** *Summary of the response time of a series of Au-NRs/Pt devices with different lengths and widths. (a), response time of Au-NRs/Pt hybrid devices on large size Pt RTD devices with a fixed length (1500 µm) but a variable width (from 200 µm to 2 µm), a λ=1.5 µm laser (laser spot: 1000 µm) was focused on these devices. (b), response time of Au-NRs/Pt hybrid devices on small size Pt RTD devices with a fixed width (2 µm) but a variable length (from 150 µm to 10 µm), a λ=1.5 µm laser (laser spot: 10 µm) was focused on these devices.*

**Table 2.3** *Summary of the response time (rise time and decay time) from a series of Au–NRs/Pt devices on large size Pt RTD devices with a fixed length (1500 µm) but a variable width (from 200 µm to 2 µm) and small size Pt RTD devices with a fixed width (2 µm) but a variable length (from 150 µm to 10 µm). The response time was measure from these Au-NRs/Pt devices under the illumination of λ=1.5 µm laser while it's ON/OFF modulated at 120 Hz.*

| **Au-NRs/Pt device (large size) Length = 1500 µm, different widths** | | | **Au-NRs/Pt device (small size) Width = 2 µm, different lengths** | | |
|---|---|---|---|---|---|
| **Width [µm]** | **Rise time [s]** | **Decay time [s]** | **Length [µm]** | **Rise time [µs]** | **Decay time [µs]** |
| 2 | 0.65 | 0.95 | 10 | 97 | 131 |
| 10 | 1.12 | 1.96 | 30 | 172 | 226 |
| 20 | 2.28 | 3.23 | 50 | 282 | 358 |
| 200 | 3.63 | 4.54 | 150 | 470 | 632 |

### 2.3.4.3 Performance of the 10 µm Au-NR/Pt device

To explore the interaction between SWIR photons and the hybrid Au-NRs/Pt devices, a homebuilt microscope[140,141] was applied where an Au-NRs/Pt device was illuminated by a λ=1.5 µm laser spot (diameter of ~ 10 µm) while the device position was controlled by a piezoelectric stage during a scanning experiment. As a function of the laser position on the device surface (corresponding to each pixel of a scanning image), the resistance of the device was analysed by measuring the voltage fell on the device under a circuit shown in **Figure 2.22**a with an external applied voltage of 0.1 V. The experimental set-up and schematic diagram of device operation are shown in Figure 2.22a and b respectively.

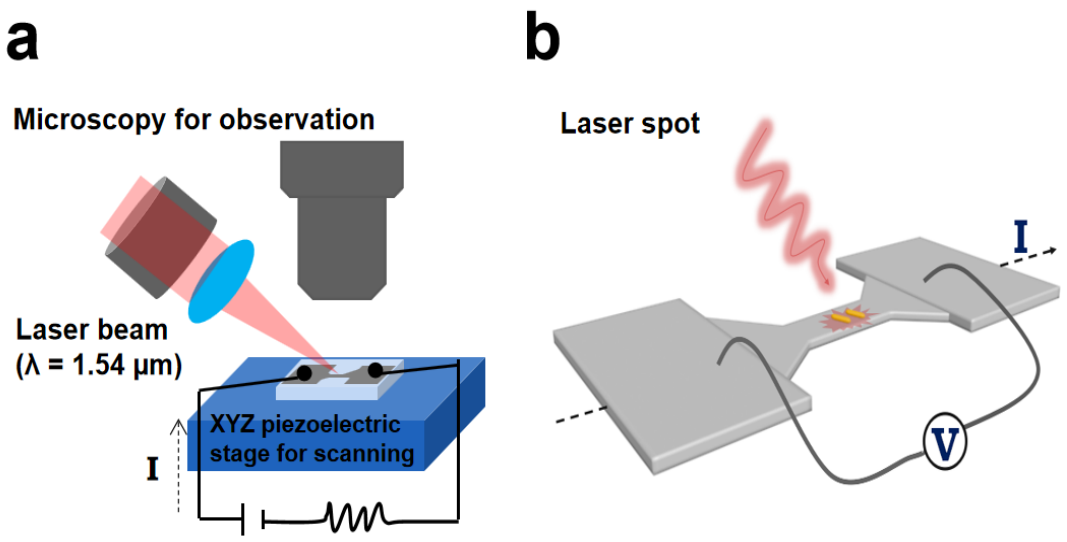


**Figure 2.22** *Experimental set-up of 10-µm devices under a 10-µm-spot continuous laser illumination (λ = 1.5 µm) while the sample position was controlled by a piezoelectric stage. (a) Schematic of the experimental set-up and the circuit used for device measurement; an external voltage of 0.1 V was applied and a current-limiting resistance (207 Ω) was placed in series with the device under test; (b) Schematic of the device where the change of voltage (DV) was measured. It is proportional to DR.*

Under identical experimental conditions, such scanning experiments were performed under a continuous laser illumination with a power density of 80 µW/µm$^2$ respectively on a control device (Pt microwire RTD without Au NRs) and an Au-NRs/Pt device (Pt microwire RTD

covered by Au NRs). Both devices are based on a Pt microwire with a dimension of 10 μm by 2 μm (below termed as "10-μm devices", Figure 2.19c). The resistance mapping obtained in such scan experiments (**Figure 2.23**a and c) exhibits a clear profile identical to the morphology characterization of the Pt microwire by SEM shown in Figure 2.19c.

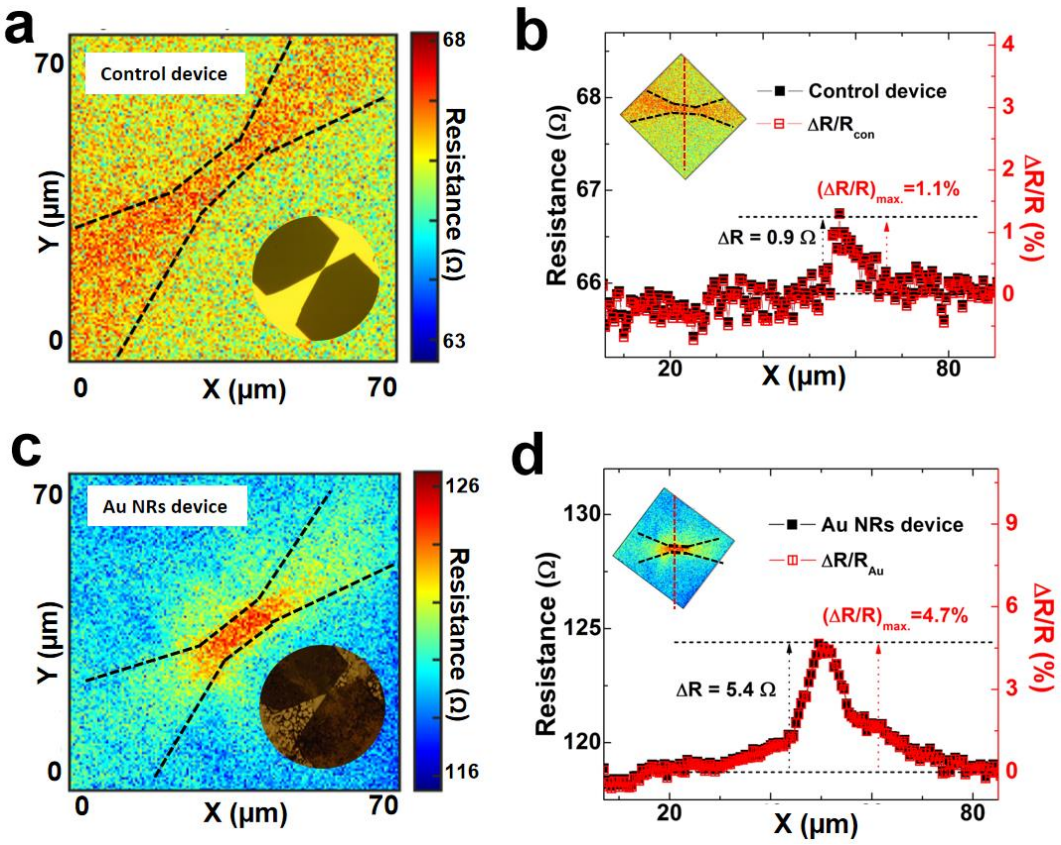


**Figure 2.23** *Resistance mapping of 10-μm devices under a 10-μm-spot continuous laser illumination (λ = 1.5 μm) while the sample position was controlled by a piezoelectric stage. (a) and (c) Resistance mappings of the control device (a) and the Au-NRs/Pt device (c) under a 10-μm-spot continuous laser illumination. (b) and (d) The cross-sectional profiles extracted from the mapping images shown in (a) and (c) and the resultant device response in terms of ΔR or ΔR/R of the control device (b) and the Au-NRs/Pt device (d).*

By comparison with the control device, a more pronounced resistance contrast was observed in the Au-NRs/Pt device, indicating a drastic increase of resistance in the Au-NRs/Pt device under laser illumination due to the plasmonic-induced photothermal effect of Au NRs: Upon absorption of the laser illumination, Au NRs generate heat and transfer it to the Pt microwire whose resistance is highly sensitive to any temperature change. By comparison, even though

there is heat generated on the control device under the same laser illumination, such amount of heat is much smaller leading to only a limited change of resistance of the device. To quantify the difference between the Au-NRs/Pt device and the control device, the resistance line profiles across a device obtain from the mapping experiments are compared (Figure 2.23b and d): Here, the change of resistance due to laser illumination normalized by the device resistance in dark ($\Delta R/R = (R_{laser} - R_{dark})/R_{dark}$) represents the relative responsivity of this type of photodetectors. Note that there was a slight difference in the absolute value of the dark resistance of the two devices, which is likely due to the existence of colloidal Au NRs coating on the Au-NRs/Pt device and any possible (resistive) surfactant residue from the synthesis. Remarkably, the $\Delta R/R$ observed in the Au-NRs/Pt device ($\Delta R/R$=4.7%) is more than four-fold larger than that observed in the control device ($\Delta R/R$=1.1%). Clearly, such responsivity enhancement originates from the existence of Au NRs and their photothermal effect.

Not only being able to provide a clear photoresponse in the form of resistance change under the $\lambda$=1.5 μm laser illumination, these Au-NRs/Pt hybrid devices exhibit also fast-switching sensing capabilities at high illumination modulation frequency. The time-dependent photoresponse of a typical 10-μm Au-NRs/Pt device under a modulated laser illumination at various frequencies is shown in **Figure 2.24**. At low laser ($\lambda$=1.5 μm) modulation frequency (Figure 2.24a-c), nearly instantaneous rise/fall of the device resistance was observed at different laser powers (from 200 μW to 1.6 mW, corresponding to a power density ranging from 10 $\mu W/\mu m^2$ to 80 $\mu W/\mu m^2$, Figure 2.24a). In particular, even under a very low laser power (200 μW, corresponding to 10 $\mu W/\mu m^2$), the Au-NRs/Pt device is still capable to generate a clear change of resistance under laser light (Figure 2.24a, dark curve) while only negligible resistance change was observed in the control device under the same condition. The photoresponsivities of both the Au-NRs/Pt device and the control device are shown in Figure 2.24b, represented by the change of resistance normalized by the laser power ($\Delta R/P$ in the unit of Ω/W or $(\Delta R/R)/P$ in the unit of %/W). By comparison to the control device, about four-fold responsivity enhancement was observed in the Au-NRs/Pt device under different applied laser powers, except for the case of the lowest laser power (200 μW) where the control device exhibited no photoresponse under the same measurement condition. The response time of this Au-NRs/Pt device can be extracted from Figure 2.24c that exhibits a zoom-in view of the rise/decay time following a square ON/OFF laser illumination operated

at 120 Hz. Defined as the time used by the resistance to increase from null to 80% of the saturation level, the response time of this device is measured as 97 µs, which is more than four orders of magnitudes smaller than the response time measured in a previous work.[134]

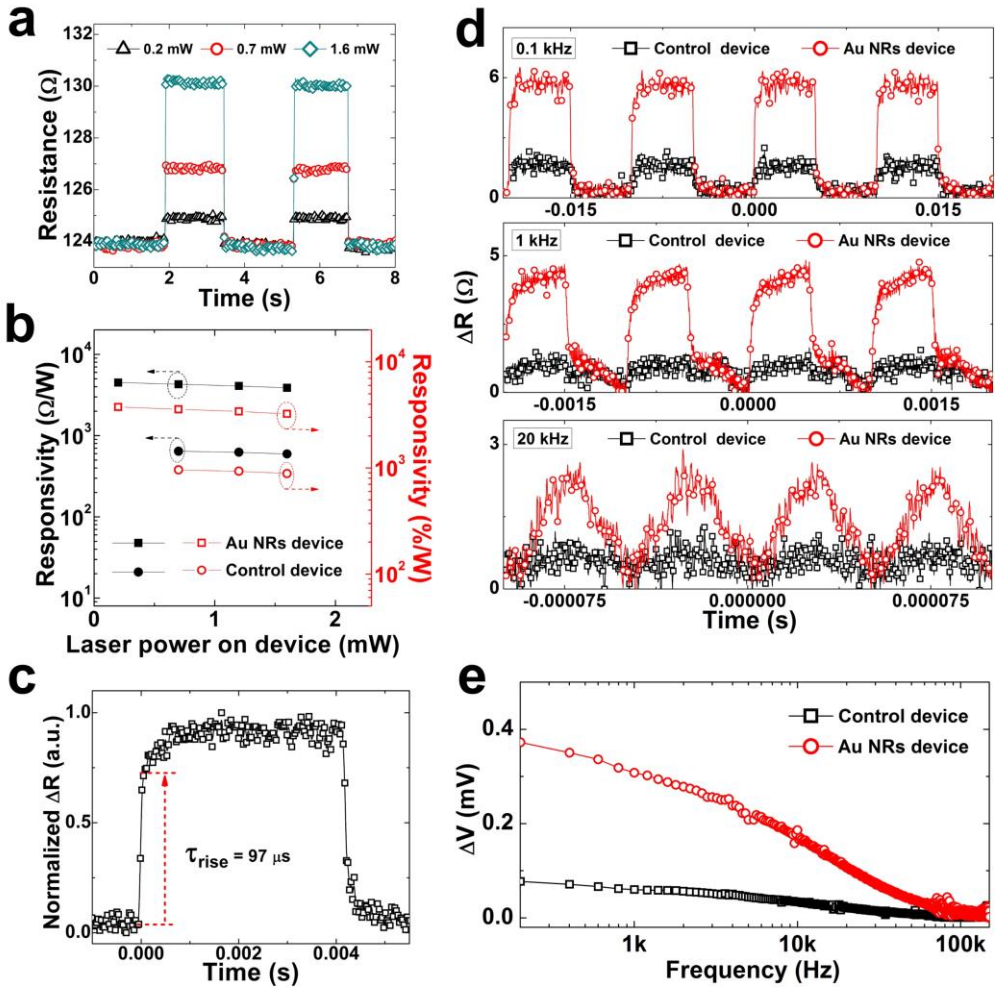


**Figure 2.24** *(a) Time-dependent photoresponse characteristics of a 10-µm Au-NRs/Pt device as a function of laser power (200 µW, 0.7 mW and 1.6 mW, corresponding to a power density of 10 µW/µm², 35 µW/µm² and 80 µW/µm², λ = 1.5 µm). (b) The photoresponsivity (in terms of R/P (Ω/W) or (ΔR/R)/P (%/W), P = laser power) of the Au-NRs/Pt device at different laser powers. (c) Zoom-in time-dependant photoresponse characteristics permitting the extraction of the device response speed (rise/decay profile) under a λ = 1.5 µm laser illumination modulated at 120 Hz. (d) Comparison of the photoresponse characteristics from the Au-NRs/Pt and the control device under a λ = 1.5 µm laser illumination modulated at different frequencies: 0.1 kHz, 1 kHz and 20 kHz. (e) Evolution of the photoresponse as a function of laser modulation frequency from 200 Hz to 150 kHz for both the control and Au-NRs/Pt device.*

Such rapid photoresponse originates from both the efficient heat transfer between Au NRs and the Pt microwire and the optimized geometry of the Pt microwire. Indeed, as the dimension of the laser spot applied in this work is about 10 µm, a 10-µm-long Pt microwire can be fully illuminated by the laser spot without the laser spot shining onto the large contact pads. If a shorter Pt microwire is used with the laser spot covering the contact pads, a large amount of heat can be generated and thus a much longer time will be needed for the device to cool down (when the illumination is off) leading to difficulties in switching off the device. Beyond this optimized Pt microwire dimension, increasing either the length or the width of the Pt microwire led also to an increased device response time (Figure 2.21 and Table 2.3). In the devices based on either a longer or wider Pt microwire, only a part of the microwire was illuminated by the laser and heat up by the Au NRs. A longer time is thus needed for these Pt microwires to reach a thermal equilibrium, leading to a longer rise time. This observation is in agreement with numerical simulations on Joule-heated nanowires[139] which show a longer response time along with an increased nanowire dimension.

The fast-response time of the optimized Au-NRs/Pt device thus allows their operation at a higher laser modulation frequency. The time-dependent photoresponse in terms of resistance change ($\Delta R$) of the Au-NRs/Pt device under a laser illumination ($\lambda$=1.5 µm) with ON/OFF modulated at 0.1 kHz, 1 kHz and 20 kHz is shown in Figure 2.24d. At all measured frequencies, a clear enhancement of photoresponse can be observed in the Au-NRs/Pt device compared to the control device. As modulation frequency increases, the time-dependant resistance change ($\Delta R$) starts to deviate from the rectangular form of the laser modulation. Nevertheless, even at 20 kHz, in contrast to the control device, the Au-NRs/Pt device is still capable to provide a clear photoresponse switching. By a lock-in amplifier, the peak-to-peak voltage $\Delta V$ (V) measured on the Au-NRs/Pt device and the control device (which is proportional to $\Delta R$) as a function of the modulation frequency of the laser beam in a continuous spectral frequency range (from 200 Hz to 150 kHz) is exhibited in Figure 2.24e. Even at 50 kHz, the Au-NRs/Pt device still exhibited a response amplitude of 40 µV, which is more than 10% of that measured under low frequency situation ($\Delta V$ = 370 µV at 200Hz). Compared to the control device, the Au-NRs/Pt device exhibited a response more than four times larger than that of the bare Pt control device on the whole frequency range, which is coherent as the observations shown in Figure 2.23 b and d.

### 2.3.4.4 Mapping of Au-NRs/Pt device under modulated illumination

As shown in Figure 2.23c, the observed resistance change under a continuous laser illumination occurs mainly at the Pt microwire, where the resistance is large, but not at the large contact pads. In order to visualize how the laser modulation frequency affects the location of the resistance change, we next performed mapping experiments on the ΔR of the device with a modulated laser. During such mapping experiments, the device position was controlled by a piezoelectric stage. In contrast to the mapping experiments shown in Figure 2.23 under a continuous laser illumination, here, several frequencies (220 Hz, 50 kHz and 100 kHz) were applied to modulate the laser (λ=1.5 μm) illumination. At each frequency, the (peak-to-peak) voltage change on the 10-μm Au-NRs/Pt or control device (which is proportional to the ΔR) was measured as a function of the position of the laser beam on the device by a lock-in amplifier with a gain of 2000.

These mapping experiments thus give a direct proof of device functioning under various laser modulation frequencies. Results obtained on the control and the Au-NRs/Pt devices are shown in **Figure 2.25**a-c and d-f, respectively. For both devices, as the frequency increases, the device responsivity decreases, this is coherent with the observation shown in Figure 2.24d. For the control device, the light modulation induces a resistance change that extends to the contact pads at low frequency (Figure 2.25a). As the frequency increases, the zone that corresponds to the resistance change shrinks down to within the microwire (Figure 2.25b). This behaviour can be explained by the fact that, at low frequency, the device has the time to heat up and cool down to a larger area within a modulation cycle. This is no more the case at higher frequency where the temperature stabilizes at an average value and only the microwire region is small enough to follow the heating and cooling sequence. The same behaviour is observed on the Au-NRs/Pt device, with a smaller device zone that corresponds to the resistance change as the frequency increases (Figure 2.25d, e and f). By comparison to the control device, at a given frequency, the Au-NRs/Pt device exhibits a more than four-fold stronger response, which is coherent with observations in Figure 2.23 and 2.24. In addition, at a given frequency, the zone that corresponds to the resistance change in the Au-NRs/Pt device is more localized than that in the control device. This is likely due to the non-uniform distribution (clustering) of the Au NRs on the Pt microwire contributing to a smaller heating zone. (About the relationship between the resistances (ΔR) and the voltage changes (ΔV) we

measured in Figure 2.25, we give the calculation process and the formulas in **Chapter 5.2 Annex II.**)

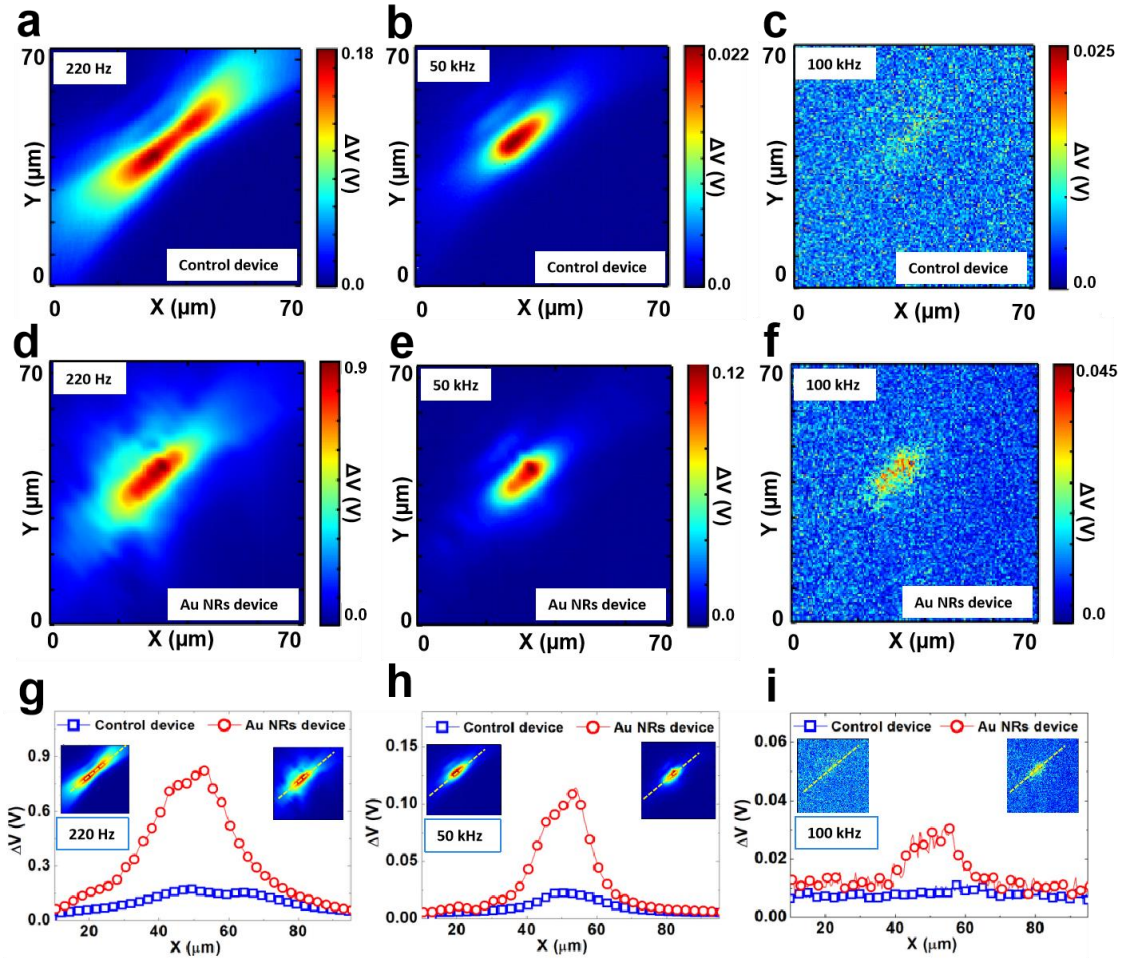


**Figure 2.25** *Mappings of the voltage changes measured on the control device (a-c) and the Au-NRs/Pt device (d-f) in the circuit described in Figure 2.22 under a 10-μm-spot of λ = 1.5 μm laser modulated at 220 Hz (a, d), 50 kHz (b, e) and 100 kHz (c, f). Note that the measured DV is proportional to DR. (g-i) The cross-sectional profiles extracted from the mapping images with the illumination modulated at 220 Hz (g), 50 kHz (h) and 100 kHz (i).*

These above results suggest that the Au-NRs/Pt device is a highly responsive photodetector able to operate at up to a few tens of kilohertz. Surprisingly, compared to the numerous applications in photocatalysis[142,143] and cancer therapy[59–62], on photodetection the photothermal effect of plasmonic nanoparticles has been rarely applied.[134] Instead, many reported photodetectors applied colloidal plasmonic nanoparticles in the device either to harvest the hot electrons generated ("hot-electron" devices)[98,144,145] or to achieve a

plasmonic-enhanced absorption in the absorber of the device.[146–148] The characteristics in terms of operation wavelengths and response speed of some representative studies applying colloidal plasmonic metallic nanoparticles for the purpose of photodetection are summarized in **Table 2.4** together with the results from this work. Remarkably, the response speed of the current Au-NRs/Pt device is hundreds of times to even thousands of times faster than previous studies. In addition, compared to previous studies, the current Au-NRs/Pt device operates at the wavelength of 1.5 µm, on which low-cost Si photodetectors do not have sensitivity.

**Table 2.4** *Summary of the response time of the photodetectors that use colloidal plasmonic metallic nanoparticles.*

| **Device structure** | **Wavelength** | **Response time** | **Ref.** |
|---|---|---|---|
| Au NPs/$TiO_2$ | 400-900 nm | 1.5 s | [145] |
| Au NRs/ZnO Nanowire | 650-850 nm | 0.25 s | [98] |
| Au NPs/Graphene | 532 nm | 1.5 s | [147] |
| Au NRs/NTC thermistor | 1.0-1.8 µm | 2.5 s | [134] |
| Au NRs/Pt | 1.5 µm | 97 µs | this work |

## 2.3.4.5 Summary of Au-NRs/Pt photodetectors

We proposed a new hybrid device structure composed of colloidal plasmonic Au NRs to achieve low-cost SWIR photon detection by coupling these NRs with a morphology-optimized resistive Pt microwire. These Au-NRs/Pt photodetectors are able to response with a rise time of 97 µs under the illumination of a λ=1.5 µm laser. Even at an illumination modulation frequency of 50 kHz, such Au-NRs/Pt photodetectors are still able to generate clear photoresponse switching. A series of mapping experiments were performed permitting a direct visualisation of the device zone where a laser illumination modulated at different frequencies can provoke a resistance change of the device. These hybrid Au-NRs/Pt hybrid photodetectors, exhibiting a fast response at a frequency up to tens of kHz, thus open a new pathway for low-cost SWIR photodetection technology.

## 2.4 Summary

Starting with material synthesis, solution-processed colloidal gold nanorods with high aspect-ratio were applied to my project, showing strong plasmonic-induced photothermal effect in the range of SWIR. In order to reveal and detect the photothermal effect from the Au NRs, we measured the temperature elevation of a few Au NRs by depositing a single $Er^{3+}$ doped $NaYF_4$ nanoparticle on their surface as a nano thermometer. This experiment shows that Au NRs have good capability for achieving a local heating under SWIR excitation. Afterwards, a NTC thermistor and a Pt microwire were combined with the Au NRs, forming the hybrid Au-NRs/thermistor and Au-NRs/Pt photodetectors, respectively. An effective responsivity was observed on these hybrid devices. In particular, after continuous optimization, the hybrid Au-NRs/Pt device showed a fast response time (97 μs) under the illumination of a $\lambda$=1.5 μm laser.

# 3. $NaYF_4:Er^{3+}$ for flexible SWIR photodetectors

In the previous chapter (**2.3.2 Photothermal effect of Au NRs**), Au NRs' temperature elevation is measured via using a single fluorescent $Er^{3+}$-doped $NaYF_4$ nanocrystal (NC) as a nanothermometer. We mentioned "this very simple mode of operation makes the combination Au-NRs/$NaYF_4:Er^{3+}$ NC a very powerful and versatile heater/temperature sensor". We also noticed that, in this configuration, the SWIR laser (1.5 μm) used for heating the Au NRs is the same than the one that excites the fluorescence of $Er^{3+}$ ions ($NaYF_4:Er^{3+}$ NC). It inspired us that upconversion nanoparticles (e.g. $NaYF_4:Er^{3+}$ NC) can be effective sensitizers to SWIR light. $NaYF_4:Er^{3+}$ upconversion nanoparticles (UCNPs) can be one possible strategy to implement 1.5- μm- wavelength photodetection, which plays an important role in applications such as optical communication, environmental gas sensing, medical diagnostics, night vision, and light detection and ranging (LIDAR).[4,149] In particular, at the wavelength of 1.5 μm, two advantages are offered: the optical loss of a typical silica fiber at this wavelength reaches its minimal value[150] and lasers (< 1 J/cm$^2$) operating at this wavelength are eye-safe.[151] 1.5 μm is therefore considered as the "magic" wavelength widely applied in optical communications. Therefore, in this chapter, we will present that how we try to apply $NaYF_4:Er^{3+}$ UCNPs for 1.5- μm- wavelength photodetection. Introduction of upconversion nanoparticle is performed in **chapter 3.1**. Nanoparticles synthesis, device fabrication and measurement are performed in **chapter 3.2 Experimental section**. Results and discussion of materials and device performance are performed in **chapter 3.3**.

## 3.1 Introduction of upconversion nanoparticle

Photon upconversion refers to a phenomenon to convert low energy photons into high energy ones. It can be carried out by various upconversion nanoparticles, which are mainly synthesized by a low-cost solution process and absent of toxic heavy metal elements, which meets our requirements as we summarized in our introduction of **chapter 1** (**Table 1.1**). Therefore, various upconversion systems in the form of solution-processed nanoparticles

(NPs) have been synthesized,[83,152–154] mostly based on the doping of trivalent lanthanide cations in a low phonon energy hosts and performing upconversion through a two- or multi-photon mechanism.[44] Since then they have been applied into many applications including biomedical engineering,[155–157] thermal sensing,[158,159] solar energy harvest,[160–162] and photodetection.[163–167] Indeed, most of these photon upconversion applications are based on $Yb^{3+}$ and $Er^{3+}$ co-doped systems capable to upconvert near-infrared light with a wavelength maximum no larger than 1.0 μm (e.g. upconversion from 808 nm or 975 nm to visible photons). Material systems able to upconvert SWIR photons remain rare. Recently, Zhang et al. fabricated novel erbium silicate nanosheets to upconvert $\lambda$ = 1.5 μm photons to visible ones.[168] By combining these nanosheets with organo-lead halide perovskites, they achieved photoconductors sensitive to $\lambda$ = 1.5 μm with a modest photoresponsivity of 0.1 mA/W (at 1 V driving voltage) and a promising response speed (rise time ≈ 900 μs). While these perovskite-erbium silicate photodetectors are important demonstrations, they can be built only on rigid substrates (not suitable for flexible applications) and they involve the use of lead. In addition, the photodetector response speed is still to be improved as it is a major figure-of-merit directly determining the application range of the devices. Equally by a photoconductor device structure, Zhao *et al.* demonstrated flexible photodetectors based on a conjugated polymer/$Er^{3+}$-doped nanoparticle hybrid sensitive to the wavelength of 1.5 μm.[165] While these polymer/$Er^{3+}$-doped nanoparticle hybrid photoconductors are highly interesting, their response speed was not characterized and they suffered from high dark currents (> $mA/cm^2$ level) likely related to the photoconductor device architecture applied. There is therefore still room to improve towards high-performance flexible photodetectors sensitive to SWIR photons without the use of highly toxic heavy metal elements.

In this work, by a photodiode device architecture, we propose high-performance heavy-metal-free flexible photodetectors sensitive to $\lambda$ = 1.5 μm photons based on the formation of a solution-processed organic/inorganic hybrid composing of conjugated polymer/small molecule bulk-heterojunctions (BHJs, host) together with $Er^{3+}$-doped upconversion nanoparticles (UCNPs, guest). A series of monodisperse colloidal inorganic $NaYF_4$:$Er^{3+}$ UCNPs of various dimensions were synthesized by hydrothermal routes (Synthesis detail is shown in **Experimental section 3.2.1**), providing effective upconversion of $\lambda$ = 1.5 μm photons to visible ones. An organic host was applied containing a donor-accepter BHJ blend of diketopyrrolopyrrole (DPP)-based copolymer and

[6,6]-phenyl-$C_{71}$-butyric acid methyl ester ($PC_{70}BM$). Such organic host exhibits strong optical absorption covering the whole visible and near-infrared spectrum up to $\lambda \approx 1$ μm and is thus capable to efficiently harvest most visible photons upconverted by the guest nanoparticles. Under the illumination of $\lambda = 1.5$ μm SWIR photons, optimized hybrid BHJ/UCNP photodetectors exhibit a clear photoresponsivity of 0.73 mA/W and 0.44 mA/W for devices built on rigid glass substrates and flexible polyethylene terephthalate (PET) substrates, respectively. Remarkably, a fast operation speed characterized by a short photocurrent rise time down to 80 μs was observed under the illumination of $\lambda \approx 1.5$ μm photons, which is faster by more than one order of magnitude than previous photodetector studies applying $Er^{3+}$- doped upconversion systems,[165,168], and by two to four orders than most other nonavalanche semiconductor photodetectors at SWIR wavelengths.[13,169–172] Exhibiting advantages such as adaptability to flexible substrates, processability in solution, absence of highly toxic heavy-metals, and superior performance, the hybrid organic/inorganic photodetectors developed in this work can be a bright contender for next-generation low-cost and high-performance SWIR photodetectors.

# 3.2 Experimental section

## 3.2.1 Synthesis of $NaYF_4:Er^{3+}$ UCNPs with tunable sizes

UCNPs were synthesized by an improved hydrothermal route.[83] To adjust the dimension of UCNPs, different concentrations of sodium citrate tribasic dihydrate (1 to 18 mmol) in 5 mL deionized (DI) water were used to react with 1 mmol of $Ln^{3+}$ (e.g. 85% $Y^{3+}$ and 15% $Er^{3+}$) in 5 mL DI water and 12 mmol of NaF in 5 mL DI water. In a typical synthesis for 300-nm $NaYF_4$:15%$Er^{3+}$ UCNPs 15 mol % $Er^{3+}$ UCNPs: a 5 mL aqueous solution of $Ln(NO_3)_3 \cdot 6H_2O$ (0.2 mol/L, $Y^{3+}$: $Er^{3+}$ molar ratio = 85:15) was mixed with a 5 mL aqueous solution of sodium citrate tribasic dihydrate (1.2 mol/L) under vigorous stirring until the formation of a white precipitate of lanthanide citrate. A 5 mL aqueous solution of NaF (2.4 mol/L) was then added slowly into the above mixture. After being stirred for 1 h, the resulting precursor solution was transferred to a 75-mL-volumn autoclave. The autoclave was sealed and then placed into an oven heated at 120 $^oC$ for 2 hours. After 2 hours, the autoclave was allowed to cool down to

room temperature naturally. Subsequently, the $NaYF_4$:15%$Er^{3+}$ UCNPs in the autoclave were separated from the reaction media by centrifugation (6000 rpm, 30 min) and then washed several times with deionized (DI) water. The obtained UCNPs were then dried in vacuum at 60 $^{o}$C for 24 h followed by a 300 $^{o}$C annealing process for 2 hours. UCNPs of other dimensions or with other $Er^{3+}$ concentrations were prepared by the same procedure.

## 3.2.2 Synthesis of ZnO nanoparticles

To fabricate the hybrid organic/inorganic photodetectors, ZnO nanoparticles (NP) was chose as an electron transfer layer in this work. Here, we give the details of the synthesis:

In two separated containers, we dissolved tetramethylammonium hydroxide (TMAH) in 30 mL of ethanol (0.55 M) and zinc acetate dihydrate into 90 mL of dimethyl sulfoxide (DMSO) (0.1 M). The TMAH solution was then added dropwise (about 2 mL/min) into the zinc acetate DMSO solution at room temperature under stirring. This solution was further stirred at room temperature for 1 hour and then storage in a refrigerator (4 $^{o}$C) until use. At the moment of use, 4 mL of the above-mentioned mixture was taken into a centrifuge tube. Ethyl acetate was added into the centrifuge tube followed by centrifugation at 6000 rpm for 10 min. After centrifugation, the mother liquid was decanted and the precipitate was collected and dispersed into 2.5 mL of ethanol. Such centrifugation process repeated one more time. As an electron transfer layer in photovoltaic devices, the ZnO NP solution dispersed in ethanol was then deposited onto the substrate by spin-coating at 2000 rpm for 60 s following by a mild annealing at 80 $^{o}$C for 15 minutes.

## 3.2.3 Device preparation and characterization

The synthetic procedure of the polymer DPPTT-T was described in a previous work.[173] To fabricate the hybrid photodetectors of this study, a layer of poly (3, 4-ethylenedioxythiophene)-poly (styrenesulfonate) **(**PEDOT: PSS, Baytron P VP Al4083), as hole transport layer, was spin-coated onto a cleaned and pre-patterned indium tin oxide (ITO) glass substrate or an ITO-PET flexible substrate. The photoactive layer was deposited by spin

coating on top. To formulate the photoactive solution, a certain concentration of UCNPs (2 to 8 mg/mL) was first dispersed in a solution containing a mixture of 80% of chloroform and 20% of 1, 2-Dichlorobenzene (DCB). This UCNP solution was then used to dissolve a mixture of DPPTT-T (6 mg/mL) and $PC_{70}BM$ (12 mg/mL). For devices without UCNPs, a solvent mixture containing 80% of chloroform and 20% of DCB was used. The photoactive solution was then spin-casted at 3000 RPM onto the PEDOT: PSS-coated substrate followed by annealing at 130 $^{o}$C for 30 minutes. The ZnO NP layer, as an electron transfer layer, was then deposited by spin-coating the above-described ZnO NP solution dispersed in ethanol (2000 rpm, for 60s). Finally, 100 nm of gold (Au) top electrode was deposited by thermal evaporation with a vacuum level at $10^{-6}$ mbar. The active area of the cells was 4 $mm^2$. Photodiode *J-V* characteristics were measured inside an Ar-filled glovebox by a computer-controlled Keithley 2612B System SourceMeter® instrument. Devices were then encapsulated by an UV-curing resin and an encapsulation glass before being transferred outside the glovebox for EQE and photoresponse measurements (except for those devices undergoing bending tests). For EQE measurements, monochromatic light was obtained from a 50 W tungsten halogen lamp in combination with a monochromator (Oriel Cornerstone 130) and it was modulated by mechanical chopper. Under each monochromatic wavelength, the device short-circuit current $I_{sc}$ was measured in air by a Stanford Research systems SR570 low-noise current preamplifier and a SR810 DSP lock-in amplifier. A NIST-calibrated Si and Ge cells were used as reference. For visible and SWIR device photoresponse, devices were under the illumination of a modulated laser either with a wavelength of 517 nm or 1.5 µm. The photo-induced current was measured by a SR570 low-noise current preamplifier together with a digital phosphor oscilloscope (DPO2024B). Bending tests of the flexible devices were carried out by a home-built adjustable mechanical stretcher set-up.

## 3.2.4 Structural and optical characterizations

SEM characterizations of UCNPs and device films were performed by a FEI Magellan 400 system with a standard field emission gun source, as shown in the following fugures:

Figure 3.1 (a-d) SEM images of $NaYF_4$:15%$Er^{3+}$ UCNPs of different dimensions and NaF/citrate/$Ln^{3+}$ molar ratios applied in the synthesis. (a-d) correspond respectively to the sample 1, 3, 4, and 6 listed in the Table 3.1.

Figure 3.2 (a-d) SEM images of $NaYF_4$:15%$Er^{3+}$ UCNPs of different dimensions and NaF/citrate/$Ln^{3+}$ molar ratios applied in the synthesis. (a-d) correspond to the sample no. 2, 5, 7 and 8 of Table 3.1 respectively.
Figure 3.8 (c) SEM image of a typical hybrid film containing the DPPTT-T/$PC_{70}$BM BHJ host with the upconversion guest NPs incorporated inside. Insert shows a zoom-in SEM image of this film.

XRD spectrum of UCNPs was obtained by a PANalytical X'Pert X-ray diffractometer using Cu-K$\alpha$ radiation, as shown in the following fugure:
Figure 3.3 XRD patterns of the UCNPs synthesized with different NaF/citrate/$Ln^{3+}$ molar ratios plotted together with the reference pattern JCPDS no. 00-016-0334.

UV-Visible absorption spectra were recorded in a transmission mode by an Ocean Optics HL-2000 fiber-coupled tungsten halogen lamp and an Ocean Optics HR4000 spectrometer (200-1100 nm). Steady-state fluorescence measurements was recorded in a reflection mode by the same Ocean Optics spectrometer with the sample being excited by a $\lambda$ = 1.5 μm single mode pigtailed laser diode. They are shown in the following fugure:
Figure 3.5 The upconversion fluorescence spectrum obtained on a single $NaYF_4$:$Er^{3+}$ NP with 10% (black), 15% (red), or 20% (blue) $Er^{3+}$ doping. Laser excitation wavelength = 1.5 μm.

For single-particle fluorescence measurement, diluted UCNPs were first casted on a microscope glass slide. The microscope glass slide was then placed in an optical microscope with the $\lambda$ = 1.5 μm laser excitation being focused on a single UCNP by a transmission mode. Single-particle upconversion fluorescence spectra were recorded by a CCD camera coupled with a monochromator (HORIBA Jobin Yvon), as shown in the following fugure:
Figure 3.5 The upconversion fluorescence spectrum obtained on a single $NaYF_4$:$Er^{3+}$ NP with 10% (black), 15% (red), or 20% (blue) $Er^{3+}$ doping. Laser excitation wavelength = 1.5 μm.

# 3.3 Results and discussion

## 3.3.1 Size-tunability of $NaYF_4:Er^{3+}$

A series of monodisperse colloidal $NaYF_4$:15%$Er^{3+}$ UCNPs were first synthesized by an improved hydrothermal route.[83] To adjust the size of the upconversion nanoparticles, different molar amounts of sodium citrate tribasic dihydrate were used to react with a fixed amount of $Ln^{3+}$ (containing 85% $Y^{3+}$ and 15% $Er^{3+}$) and NaF. Detailed preparation process is described in the experimental section. With the rest of the synthetic parameters being identical, the amount of sodium citrate tribasic dehydrate allowed a tuning the UCNP particle dimension from 150 nm to 1000 nm. The morphology and dimension of the as-synthesized UCNPs were characterized by scanning electron microscope (SEM, **Figure 3.1** and **Figure 3.2**). Powder X-ray diffraction (XRD) confirmed that the crystal structure of all batches of UCNPs of different dimensions to be the hexagonal β phase (**Figure 3.3**), which is generally considered as the phase allowing strong fluorescence in contrast to the cubic α phase.[174] The synthesis parameters and characteristics of the samples are summarized in **Table 3.1**.

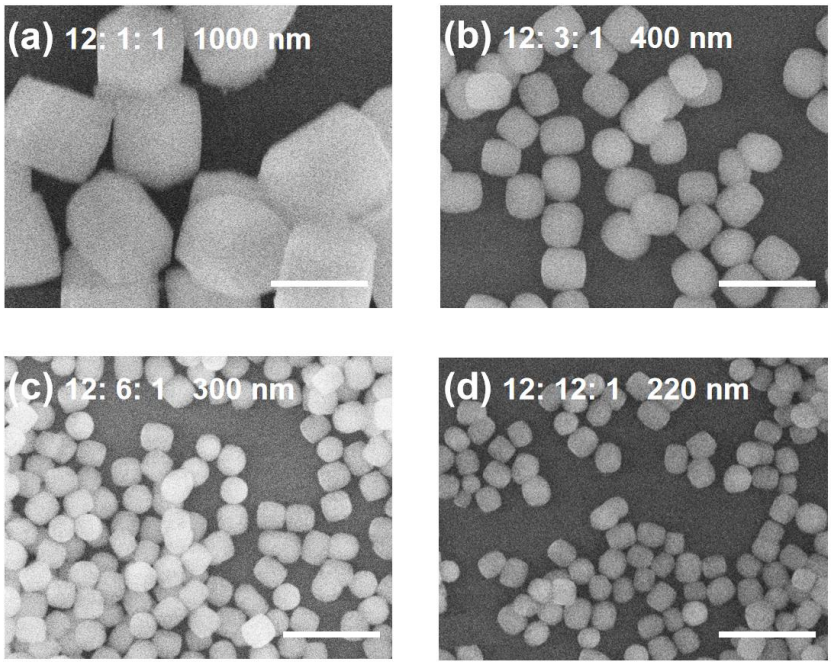


**Figure 3.1** *(a-d) SEM images of $NaYF_4$:15%$Er^{3+}$ UCNPs of different dimensions and NaF/citrate/$Ln^{3+}$ molar ratios applied in the synthesis. Scale bar = 1 μm. (a-d) correspond respectively to the sample 1, 3, 4, and 6 listed in the Table 3.1.*

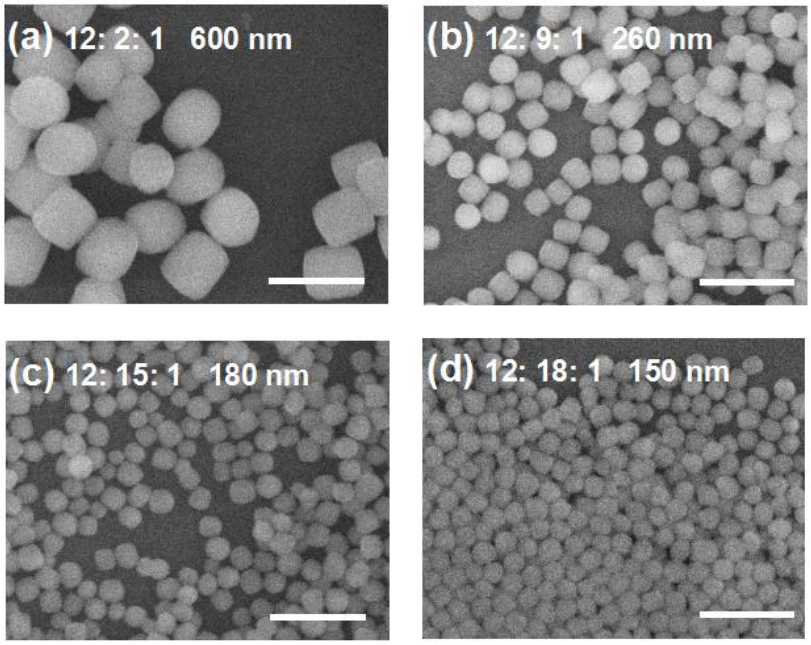


**Figure 3.2** *(a-d) SEM images of $NaYF_4$:15%$Er^{3+}$ UCNPs of different dimensions and NaF/citrate/$Ln^{3+}$ molar ratios applied in the synthesis. (a-d) correspond to the sample no. 2, 5, 7 and 8 of Table 3.1 respectively. Scale bar = 1 µm.*

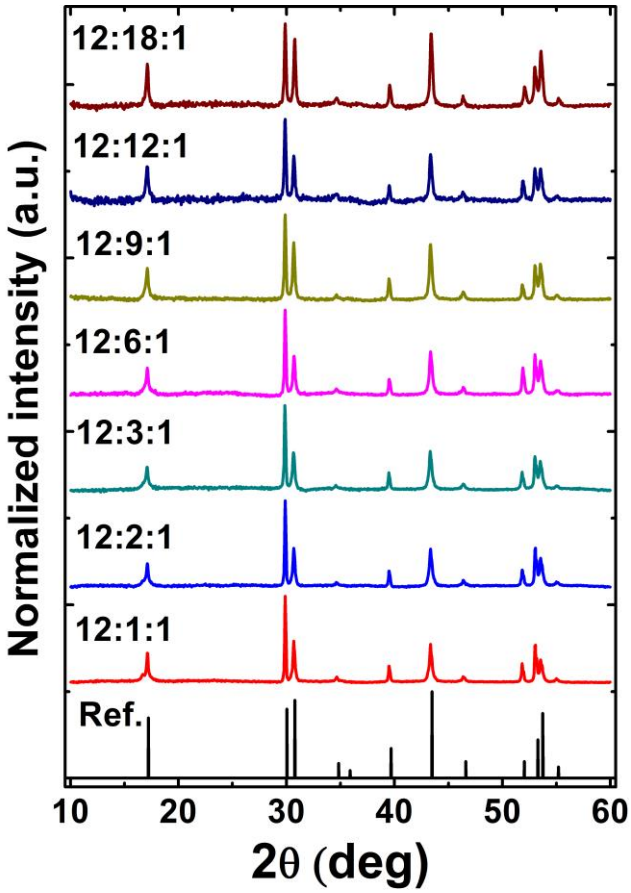


**Figure 3.3** *XRD patterns of the UCNPs synthesized with different NaF/citrate/$Ln^{3+}$ molar ratios plotted together with the reference pattern JCPDS no. 00-016-0334.*

**Table 3.1** *Synthesis conditions and characteristics of the samples.*

| Sample no. | NaF/citrate/$Ln^{3+}$ molar ratio | Phase | Morphology | Size (nm)[a)] |
|---|---|---|---|---|
| 1 | 12: 1: 1 | β | Hexagonal prism | 1050 ± 70 |
| 2 | 12: 2: 1 | β | Ellipsoid | 600 ± 37 |
| 3 | 12: 3: 1 | β | Ellipsoid | 400 ± 34 |
| 4 | 12: 6: 1 | β | Ellipsoid | 300 ± 21 |
| 5 | 12: 9: 1 | β | Ellipsoid | 260 ± 20 |
| 6 | 12: 12: 1 | β | Ellipsoid | 220 ± 23 |
| 7 | 12: 15: 1 | β | Ellipsoid | 180 ± 31 |
| 8 | 12: 18: 1 | β | Sphere | 150 ± 26 |

a) Error bars are calculated based on the measurements of 50 UCNPs from their SEM images.

## 3.3.2 Optical property of UCNPs and UCNP-organic hybrids

The obtained $NaYF_4$:15%$Er^{3+}$ UCNPs exhibited strong room-temperature fluorescence under the excitation of a λ = 1.5 μm laser. At this excitation, multiple fluorescence peaks were observed in the fluorescence spectrum, with their maximum intensity falling at the wavelength of 980 nm (infra-red), 810 nm (infra-red), 650 nm (red), 545 nm (green), and 520 nm (green) (**Figure 3.4**). Mechanisms have been proposed to explain the such photon upconversion property in similar rare-earth-doped fluoride crystals.[109,175] For instance, by a simplified picture, the red and the two green emission lines originate from a three-photon upconversion mechanism following by the de-excitations respectively from the $^4F_{9/2}$, $^4S_{3/2}$, and $^2H_{11/2}$ state to the $^4I_{15/2}$ state (Figure 3.4).

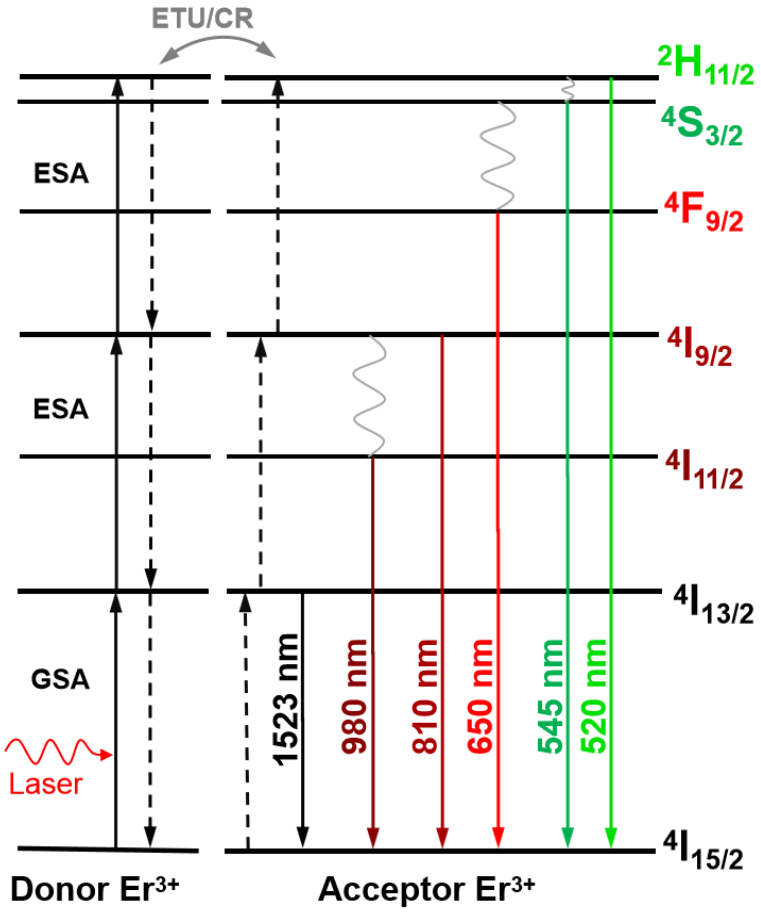


**Figure 3.4** *Schematic illustrating the energy transitions corresponding to the upconversion fluorescence observed under the excitation of a λ = 1.5 μm laser. ETU = energy-transfer upconversion, GSA = ground-state absorption, CR = cross-relaxation, ESA = excited-state absorption.*

UCNPs of other $Er^{3+}$ doping amounts were also investigated. From single-particle fluorescence experiments, a $NaYF_4$:$Er^{3+}$ UCNP with 15% $Er^{3+}$ doping appeared to exhibit the strongest upconversion fluorescence compared to a $NaYF_4$:$Er^{3+}$ UCNP with 10% or 20% of $Er^{3+}$ doping (**Figure 3.5**). 15% of $Er^{3+}$ doping was therefore chosen for the photodetector experiments described below (**Figure 3.6**). For a typical batch of $NaYF_4$:15%$Er^{3+}$ UCNPs with a particle dimension of 300 nm, the upconversion fluorescence quantum yield (under a λ = 1.5 μm laser excitation at 45 mW) was determined to be about 2% using an integrating sphere by a method established previously.[176] (Experiments set-up on the measurement of a single UCNP and the upconversion fluorescence quantum yield are shown in **Chapter 5.3 Annex III**.)

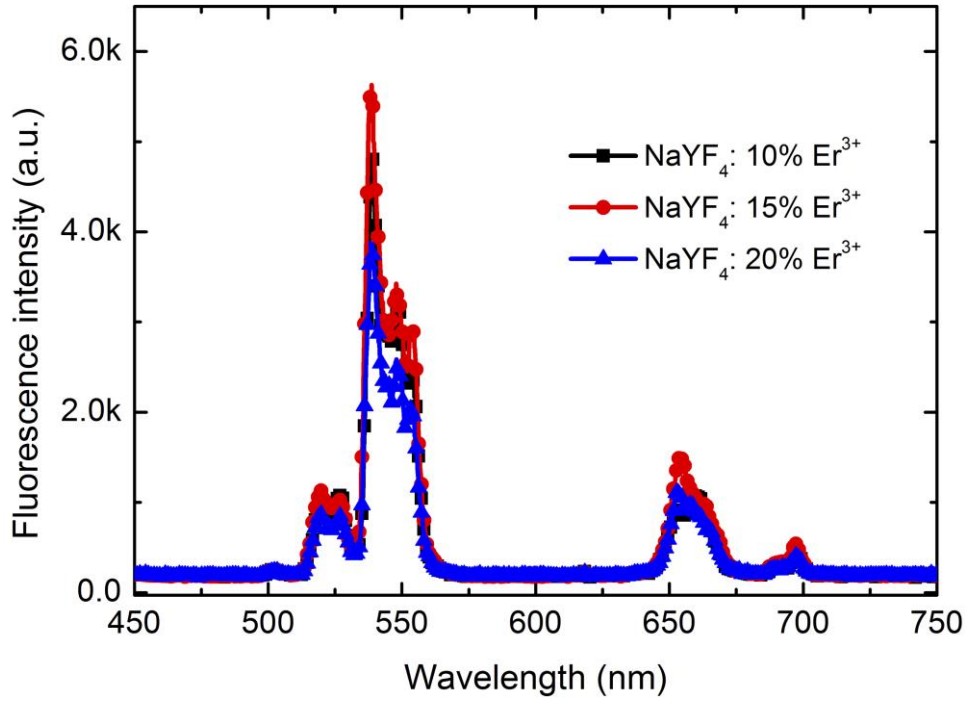


**Figure 3.5** *The upconversion fluorescence spectrum obtained on a single $NaYF_4:Er^{3+}$ NP with 10% (black), 15% (red), or 20% (blue) $Er^{3+}$ doping. Laser excitation wavelength = 1.5 μm.*

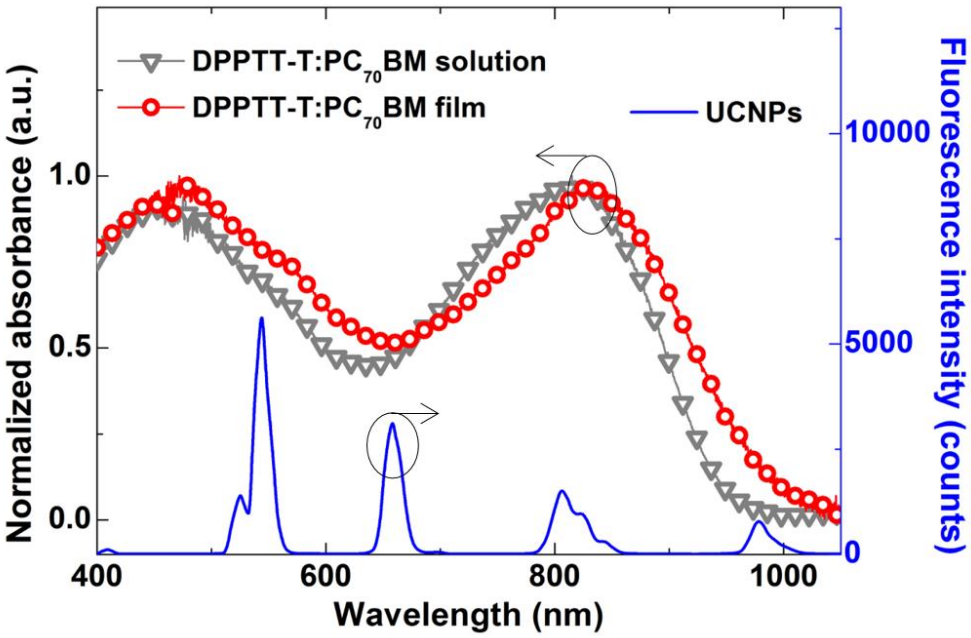


**Figure 3.6** *UV-vis absorbance spectra of a BHJ blend of DPPTT-T:$PC_{70}$BM in solution (grey) and in the form of a thin film (red). The upconversion fluorescence spectrum of the $NaYF_4:15\%Er^{3+}$ UCNPs with a dimension of 300 nm is exhibited by the blue curve with open squares (laser excitation λ = 1.5 μm, power = 25 mW).*

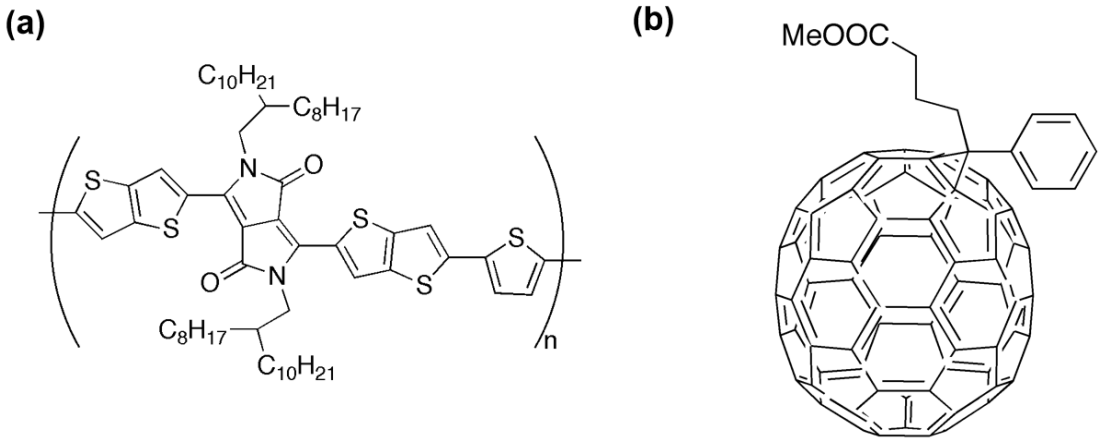


**Figure 3.7** *The molecular structure of DPPTT-T and $PC_{70}BM$ is shown in (a) and (b), respectively.*

In order to harvest the multiple upconversion fluorescence peaks from $NaYF_4$:15%$Er^{3+}$ UCNPs, a bulk-heterojunctions (BHJ) blend of poly-thieno[3,2-*b*]thiophene-diketopyrrolopyrrole-co-thio-phene (DPPTT-T) and $PC_{70}BM$ was employed as the organic host to incorporate the inorganic upconversion guest NPs in solution before the hybrid solution being spin-coated on a substrate for device fabrication (**Figure 3.7**). Such diketopyrrolopyrrole (DPP)-based copolymer DPPTT-T has been shown as a high-mobility polymer leading to high-performance field-effect transistors and photovoltaic devices.[173,177] As shown in Figure 3.6, the BHJ blend of DPPTT-T/$PC_{70}BM$ exhibited a broad optical absorption covering the whole visible and near-infrared spectrum up to the wavelength of about 1 μm. This organic blend should therefore be capable to absorb the majority the upconversion fluorescence generated by the guest particles.

## 3.3.3 Device architecture and photoresponse performance

The schematic describing the hybrid BHJ(DPPTT-T/$PC_{70}BM$)/UCNP photodetector device architecture and the device operating principle are shown in **Figure 3.8**a and 3.8b. In these hybrid photodetectors, the inorganic guest UCNPs are sensitive to $\lambda$ = 1.5 μm illumination on which the organic host has limited absorption capability. SWIR photons are upconverted by UCNPs to visible ones followed by energy transfer to the organic BHJ host, where electron-hole pairs are generated, separated and transported toward the respective transport

layers (ZnO and PEDOT:PSS), and then they are collected by the respective electrodes (Au and ITO). We first optimized the device performance by comparing the incorporation of various batches of guest UCNPs of different dimensions. Previous photovoltaic studies showed that the thickness of the active BHJ layer is typically smaller than 400 nm for efficient charge transport and extraction.[178–180]

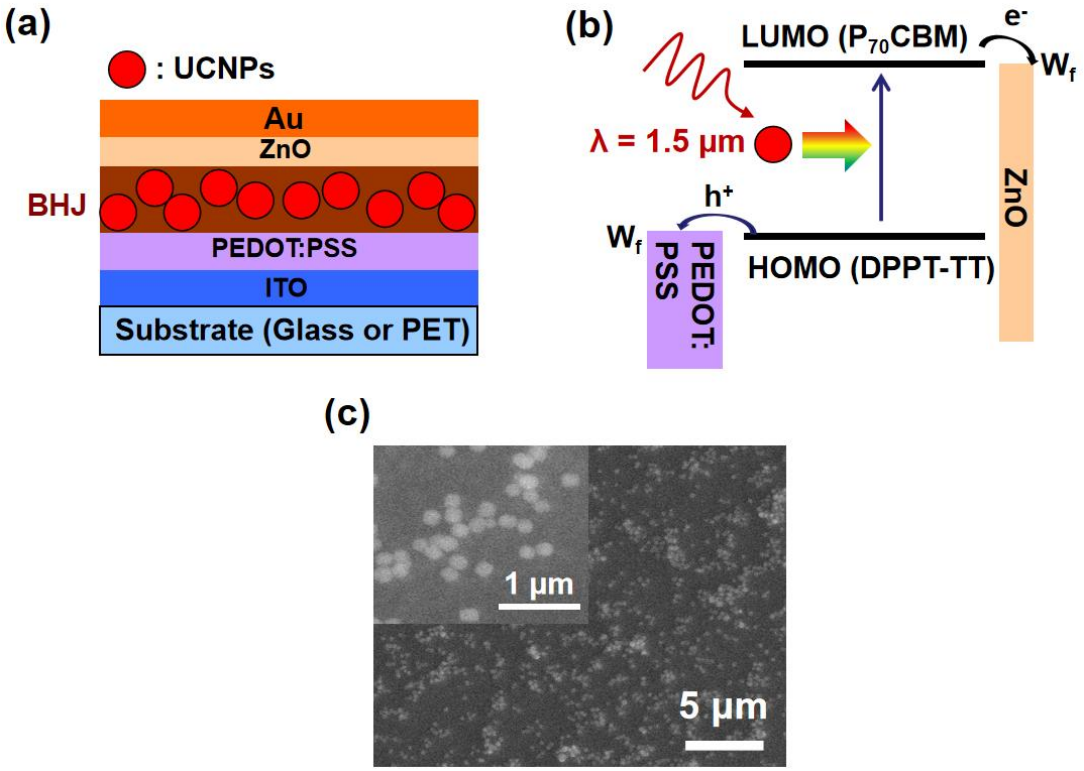


**Figure 3.8** *(a) Schematic describing the hybrid BHJ(DPPTT-T/$PC_{70}BM$)/UCNP photodetector device architecture. (b) Schematic of the operating principle of such hybrid photodetector by upconversion. (c) SEM image of a typical hybrid film containing the DPPTT-T/$PC_{70}BM$ BHJ host with the upconversion guest NPs incorporated inside. Insert shows a zoom-in SEM image of this film.*

Here, the UCNPs to be incorporated in the organic layer were thus chosen to have a dimension smaller than 400 nm in order not to drastically increasing the surface roughness of the hybrid layer, despite the observation that the fluorescence quantum efficiency increases along with the UCNP dimension. Devices containing five different batches of UCNPs of various particle dimensions ranging from 180 nm to 400 nm were compared (**Figure 3.9**).

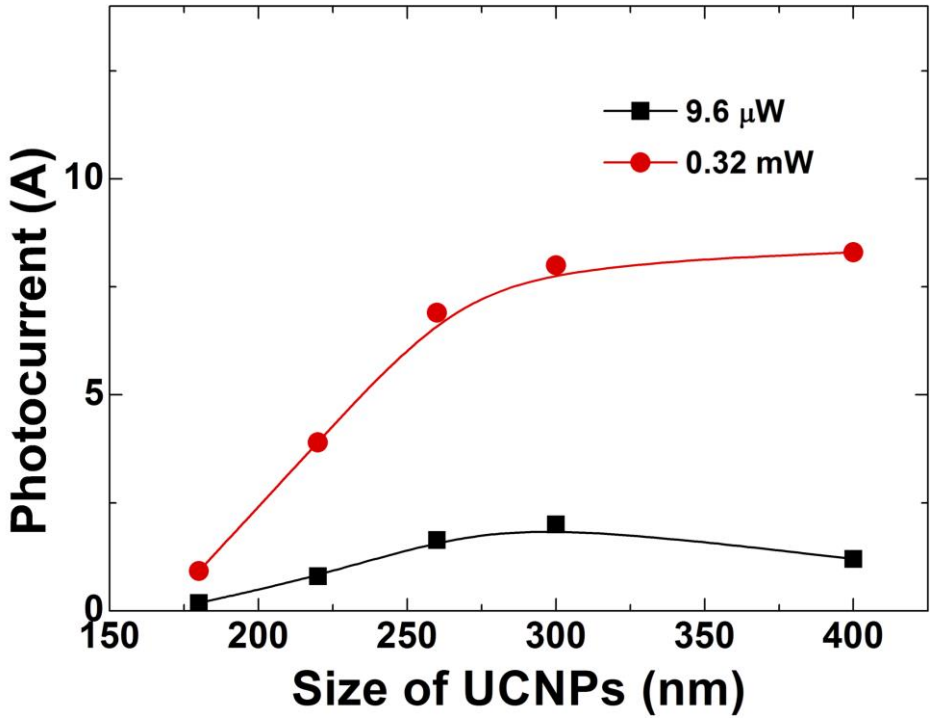


**Figure 3.9** *Comparison of the obtained photocurrent from hybrid BHJ(DPPTT-T/$PC_{70}BM$)/UCNP photodetectors fabricated with UCNPs of different particle dimensions. Photocurrents were obtained under $\lambda$ = 1.5 μm laser illumination with a laser power of 9.6 μW (black) or 0.32 mW (red).*

Among them, 300-nm UCNPs enable the largest photocurrent in these hybrid photodetectors and they were then chosen for further studies described below. Besides the UCNP dimension, the amounts of UCNPs to be incorporate into the hybrid devices are also optimized by changing the UCNP solution concentration during the device fabrication (**Figure 3.10**). The SEM characterizations of a hybrid BHJ(DPPTT-T/$PC_{70}BM$)/UCNP film fabricated by the optimized conditions are showed in Figure 3.10c, where a uniform dispersion of UCNPs in the organic layer is visible without the formation of neither large aggregates nor a compact NP layer.

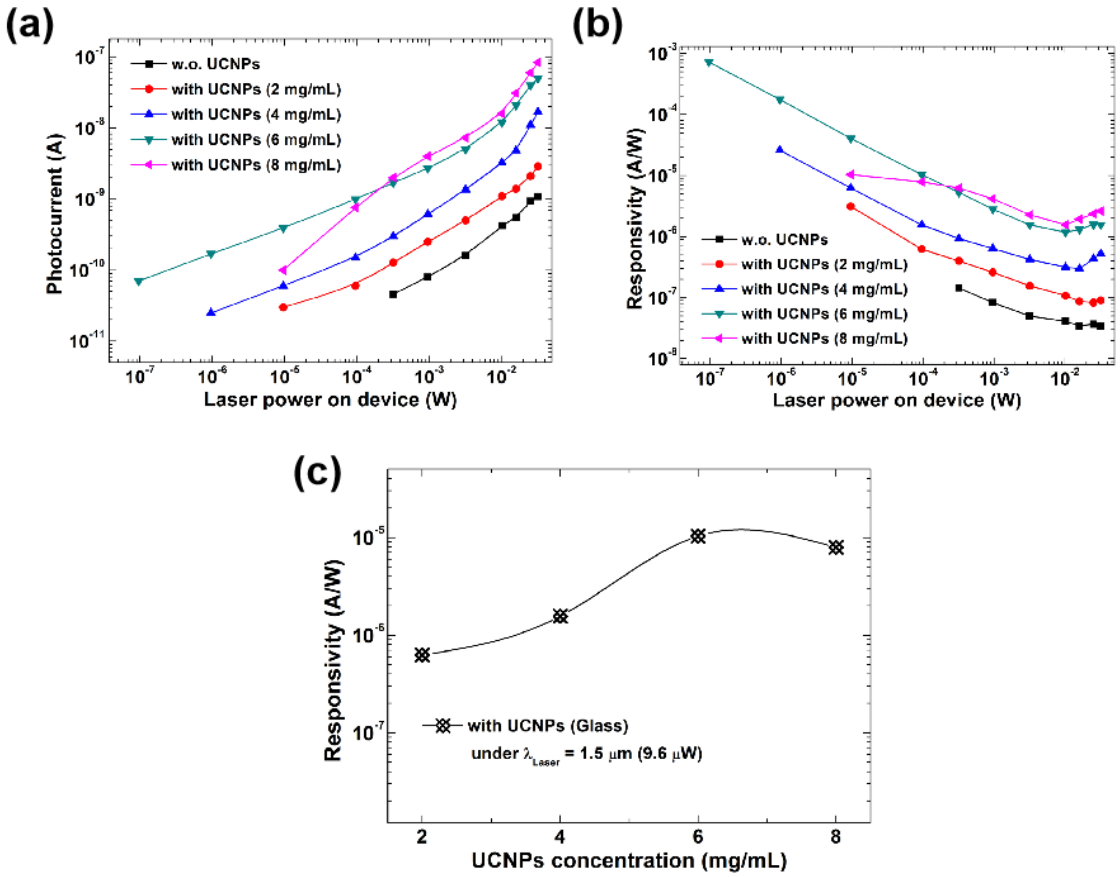


**Figure 3.10** *Comparison of the obtained photocurrent and photoresponsivity from hybrid BHJ(DPPTT-T/$PC_{70}BM$)/UCNP photodetectors fabricated by a UCNP solution of different concentrations (0 mg/mL, 2 mg/mL, 4 mg/mL, 6 mg/mL and 8 mg/mL). Photocurrents were obtained under λ = 1.5 μm laser illumination.*

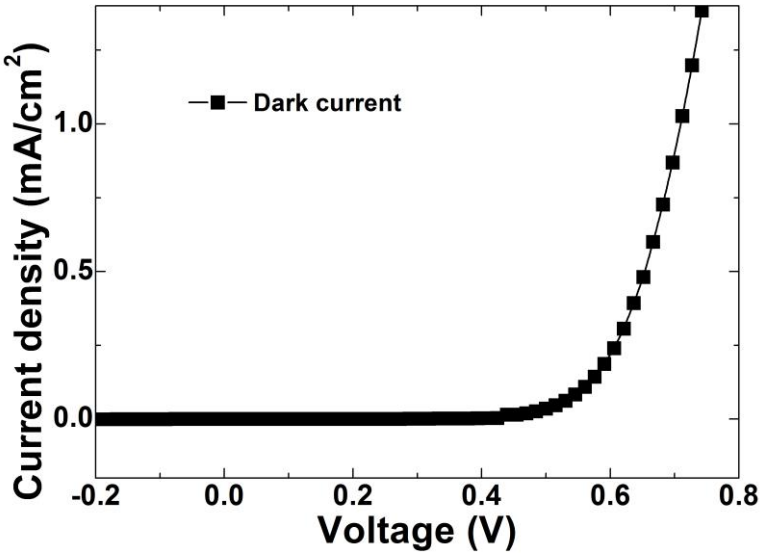


**Figure 3.11** *The current-voltage characteristic of a typical hybrid BHJ(DPPTT-T/$PC_{70}BM$)/UCNP photodetector.*

By the above-mentioned optimized conditions, hybrid photodetectors were fabricated both on rigid ITO/glass and flexible ITO/PET substrates. These hybrid photodetectors exhibit a clear rectifying behavior (**Figure 3.11**). Despite the wide band-gap and insulating nature of these UCNPs,[181] with an optimized NP concentration, their existence did not impede significantly the functioning of the BHJ photodiode. Importantly, under the illumination of a $\lambda$ = 1.5 μm laser at different laser powers, these photodetectors offered a fast rise of photocurrent without the need of any driving voltage and a low dark current on the order of $10^{-10}$ A (**Figure 3.12**a). At $\lambda$ = 1.5 μm illumination, the photoresponsivity of these hybrid photodetectors reaches 0.73 mA/W and 0.44 mA/W for rigid devices built on ITO/glass and flexible devices on ITO/PET, respectively (Figure 3.12b). By comparison to rigid devices, the slight reduction of photoresponsivity in flexible devices may originate from the differences in sheet resistance, surface roughness and optical transmission. In the organic BHJ device without any guest UCNPs, there was a weak photoresponse at $\lambda$ = 1.5 μm illumination possibly originates from the near-infrared absorption of the charge-transfer complex generated in the BHJ host (Figure 3.12b). Nevertheless, the photoresponse from such charge-transfer complex remains small by comparison to the hybrid devices, which exhibit a significantly higher photocurrent nearly by 2 orders of magnitudes. More importantly, at low laser power ($< 10^{-4}$ W) illumination, devices without any guest UCNPs are no longer capable to perform photodetection while hybrid devices generate clear photocurrent. The time-dependent photoresponse of the hybrid device under the illumination of a $\lambda$ = 1.5 μm laser at 9.6 μW modulated at 7 Hz and 1.177 kHz is shown in Figure 3.12c. The time-dependent photoresponse of the hybrid device under visible illumination ($\lambda$ = 517 nm laser, power = 1.5 μW) is shown in **Figure 3.13**. From a single representative light/dark cycle at $\lambda$ = 1.5 μm illumination (Figure 3.12d), one can analyze the response time of a typical hybrid device. Defined as the time used by the photocurrent to increase from null to 80% of the saturation level or the time used by the photocurrent to decrease from the saturation level to 20% of it, the rise ($\tau_R$) and decay time ($\tau_D$) of the hybrid device were measured as 80 μs and 120 μs, respectively. Being an important figure-of-merit for photodetectors, the response speed of these hybrid devices characterized by a short rise time is faster by more than one order of magnitude than previous photodetector studies applying $Er^{3+}$-doped upconversion systems.[165,168] The external quantum efficiencies (EQEs) of these hybrid photodetectors over the visible – SWIR spectrum are shown in Figure 3.12e, revealing an EQE up to $10^{-2}$ % at $\lambda$ = 1.5 μm.

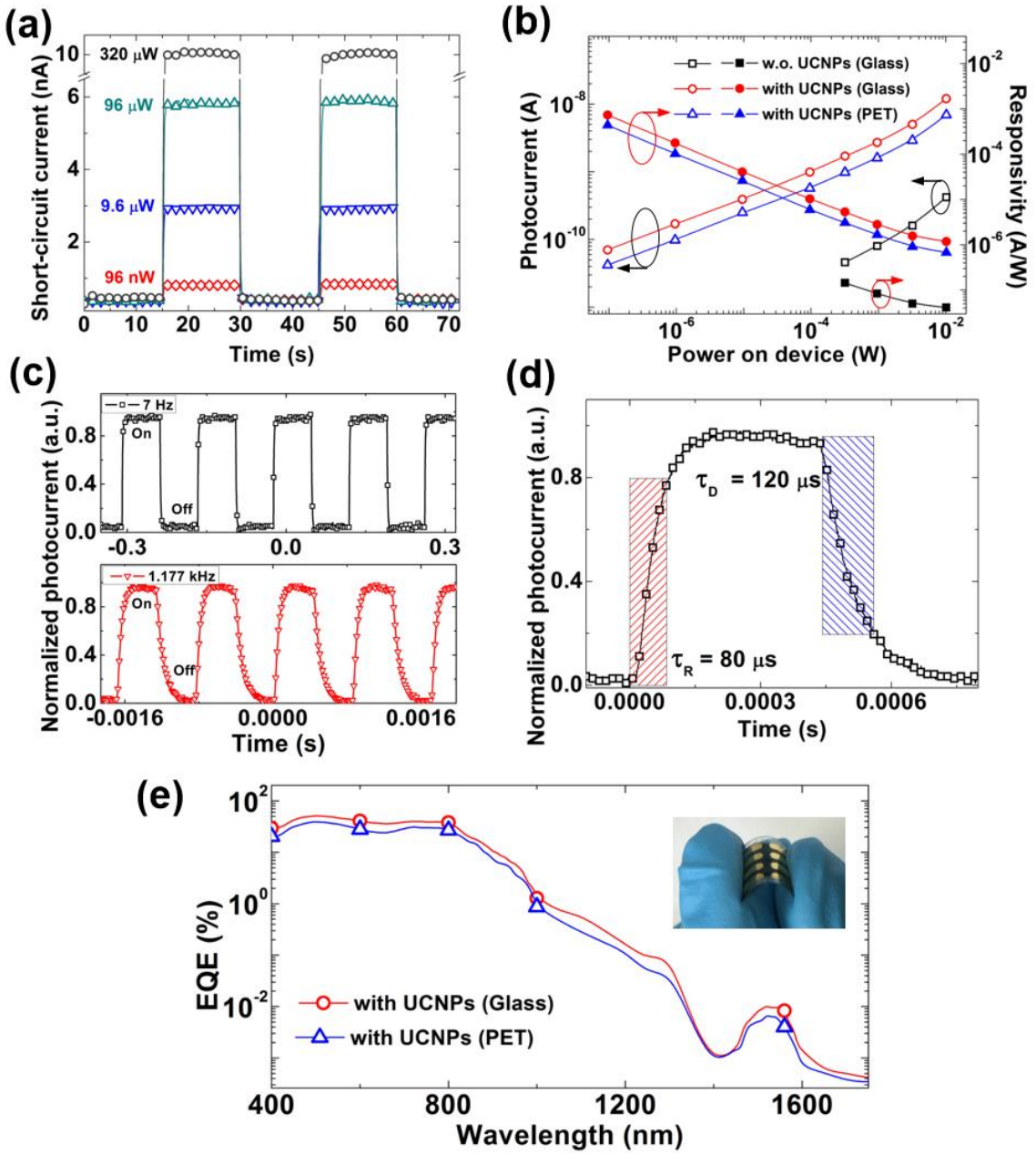


**Figure 3.12** *(a) Time-dependent short-circuit current (bias voltage = 0 V) of an optimized BHJ/UCNP photodetector under the illumination of a λ = 1.5 μm laser at different laser powers. (b) Photocurrent and photoresponsivity as a function of incident laser power of the hybrid photodetector built on a glass substrate and a flexible PET film presented together with the characteristics obtained from a device without any guest NPs incorporated. (c) Time-dependent photoresponse under the illumination of a λ = 1.5 μm laser at 9.6 μW modulated at 7 Hz and 1.177 kHz. (d) Response time study on a single representative light/dark cycle ($\tau_R$ = rise time, and $\tau_D$ = decay time). (e) External quantum efficiency (EQE) of the hybrid photodetector built on a glass substrate and a flexible PET film. Inset exhibits the optical image of a flexible hybrid photodetector.*

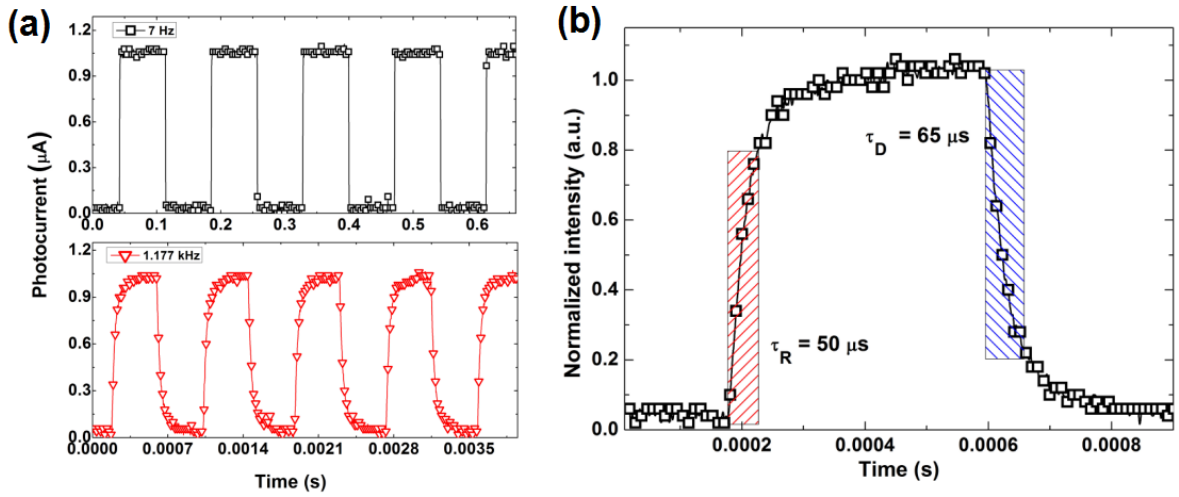


**Figure 3.13** *(a) The time-dependent photoresponse of an optimized hybrid device under the illumination of a λ = 517 nm laser (power = 1.5 μW) modulated at different frequencies. (a) photoresponse under low and high frequency. (b) Response time study on a single representative light/dark cycle under λ = 517 nm laser illumination ($\tau_R$ = rise time, and $\tau_D$ = decay time).*

## 3.3.4 Comparison with other SWIR photodetectors

Similar SWIR photodetector studies capable to detect λ = 1.5 μm illumination were summarized in **Table 3.2** together with the current results. These hybrid BHJ(DPPTT-T/$PC_{70}BM$)/UCNP photodetectors are one of the rare cases that exhibit simultaneously multiple advantages including solution-processability, flexibility, and the absence of toxic heavy metal elements together with a fast operation speed and good photoresponsivity.

**Table 3.2** *The performance of photodetectors based on different materials under λ = 1.5 μm illumination.*

| Materials | Driving voltage[a] (V) | Responsivity | Rise/Decay time | No heavy metal elements | Solution-processed | Flexible | Ref. |
|---|---|---|---|---|---|---|---|
| Monolayer graphene | 0.1 | 0.2 A/W | ~ 50 s | Y | N | N | [182] |
| Chip-integrated graphene | 0 to 1 | 0.1 A/W (@1 V)<br>15 mA/W (@0 V) | 100-200 ns[b] | Y | N | N | [19] |
| Gold NP array + graphene | 10 | 83 A/W | 600 ns | Y | N | N | [183] |
| Graphene-PbS | 5 | $5 \times 10^5$ A/W | 10 ms/<br>100 ms to 1 s | N (Pb) | N | N | [184] |
| Black phosphorus | 0.1/11 | 6 mA/W | 0.1 ms/0.3 ms | Y | N | N | [185] |
| $MoS_2$ | 10 | ~ 33 mA/W | - | Y | N | N | [186] |
| Gold grating-based hot carrier device | 0 (Self-driven) | 0.45 mA/W | - | Y | N | N | [187] |
| $Cu_2SnS_3$ Quantum Dots | | 0.93 mA/W | 4.1 s/3.8 s | Y | Y | N | [188] |
| PbS:P3HT:PCBM | -5 | 0.5 A/W | 69 μs/91 μs | N (Pb) | Y | N | [189] |
| PbS | 0 to -1 | ~ 0.1 A/W | ~ 50 μs | N (Pb) | Y | N | [190] |
| Perovskite-Erbium Silicate | 1 | 0.1 mA/W | 0.9 ms | N (Pb) | N | N | [168] |
| Graphene-$Cu_{3-x}P$ NC film | 0 (Self-driven) | 19.16 mA/W | 0.79 s/0.54 s | Y | N | Y | [191] |
| DPPTT-T/$PC_{70}BM$ / $NaYF_4:Er^{3+}$ | 0 (Self-driven) | 0.73 mA/W (glass)<br>0.44 mA/W (PET) | 80 μs/120 μs | Y | Y | Y | This work |

[a] For some studies based on field-effect transistor structures, two applied voltages are indicated: source-drain voltage $V_{ds}$ / gate voltage $V_g$

[b] Estimated from device bandwidth

## 3.3.5 Mechanical bending tests on flexible hybrid devices

Mechanical bending tests were carried out on the flexible hybrid BHJ(DPPTT-T/PC70BM)/UCNP devices built on ITO/PET substrates in order to test their robustness. Through an adjustable mechanical set-up[192,193] (shown in the insert of **Figure 3.14**a), a more than 120$^{o}$ bending angle was given on these devices and the photocurrent under λ = 1.5 μm illumination was measured after a certain bending times (Figure 3.14). Minimal photocurrent roll off (≈ 5%) was observable after five hundred bending times. As shown in Figure 3.14b, after two hundred bending times, the time-dependent photoresponse under λ = 1.5 μm illumination of the flexible hybrid device is nearly identical as that before bending, suggesting a highly reproducible photodetector functionality for flexible applications.

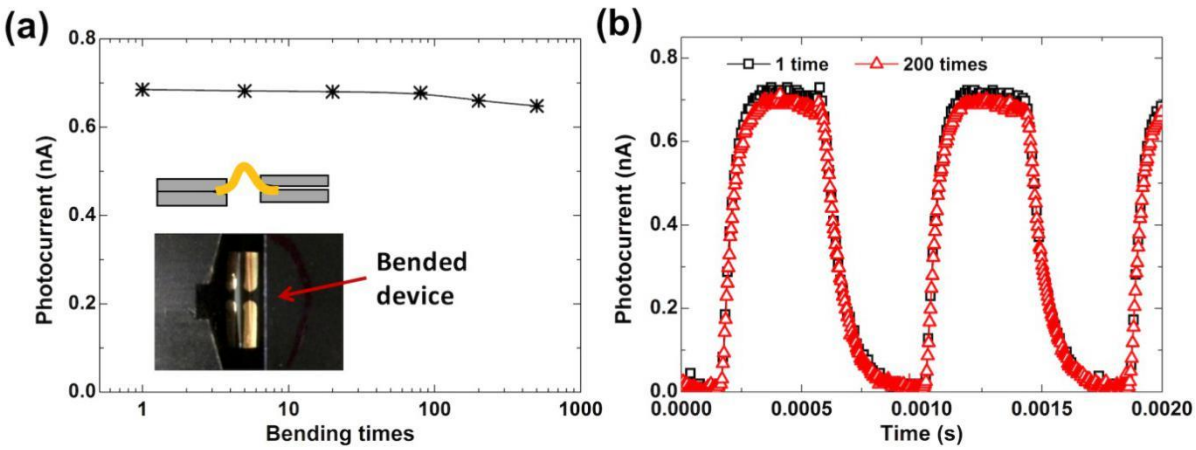


**Figure 3.14** *Bending test of a flexible hybrid BHJ(DPPTT-T/$PC_{70}BM$)/UCNP photodetector built on a ITO/PET substrate. (a) Photocurrent of this device measured after a certain bending times under the illumination of a λ = 1.5 μm laser at 96 μW. (b) Time-dependent photoresponse of the same device after 1-time-bending and 200-time-bending.*

## 3.4 Summary

In summary, high-performance heavy-metal-free flexible photodetectors sensitive to λ = 1.5 μm photons were fabricated based on the formation of a solution-processed hybrid composing of a conjugated DPP-base polymer/$PC_{70}BM$ BHJ organic host together with inorganic $NaYF_4$:15%$Er^{3+}$ upconversion guest particles. In these hybrid photodetectors, the inorganic guest UCNPs are sensitive to λ = 1.5 μm illumination on which the organic host has limited absorption. SWIR photons are upconverted by UCNPs to visible ones followed by energy transfer to the organic BHJ host, where photocurrents were generated. Under the illumination of λ = 1.5 μm SWIR photons, optimized hybrid BHJ/UCNP photodetectors exhibit a photoresponsivity of 0.73 mA/W and 0.44 mA/W respectively for devices built on rigid ITO/glass substrates and flexible ITO/PET substrates. In these devices, a fast operation speed characterized by a short photocurrent rise time down to 80 μs was observed. Mechanical bending tests revealed a highly reproducible character in these hybrid photodetectors even after hundreds of bending times for flexible applications. Exhibiting simultaneously multiple advantages including solution-processability, flexibility, and the absence of toxic heavy metal elements together with a fast operation speed and good photoresponsivity, these hybrid BHJ(DPPTT-T/$PC_{70}BM$)/UCNP photodetectors open bright opportunities for next-generation low-cost and high-performance SWIR photodetectors.

# 4. Conclusion and perspectives

In this thesis, I first introduced the current status and technological prospect of SWIR photodetectors and revealed the potential of solution-processed nanocrystals in the next-generation of photodetection with the merits of low-cost and environment considerations.

Towards the objective of SWIR photodetection, two types of colloidal nanocrystals were used into my project: 1) solution-processed colloidal gold nanorods with high aspect-ratio as well as strong plasmonic-induced photothermal effect in SWIR spectrum; 2) a series of $NaYF_4:Er^{3+}$ upconversion nanocrystals with the capacity of converting a near-infrared (1.5 μm) excitation into visible emissions.

In order to harvest the remarkable photothermal effect from the Au NRs, a hybrid device structure is formed composing NTC thermistor or a Pt microwire and the Au NRs: Au-NRs/thermistor and Au-NRs/Pt, respectively. For Au-NRs/thermistor photodetector, the plasmonic-induced photothermal effect of Au NRs (i) enables the photo-sensing capability in a hybrid Au-NRs/thermistor device structure under relatively weak illumination and (ii) boost the photo-response of the hybrid device when illumination intensity is high. The response speed of the current Au-NRs/thermistor hybrid device is as short as 2 seconds, limited by the response speed of the thermistor itself. For Au-NRs/Pt photodetector, it is able to response with a rise time of 97 μs under the illumination of a $\lambda$ = 1.5 μm laser. Even at an illumination modulation frequency of 50 kHz, such Au-NRs/Pt photodetectors are still able to generate clear photoresponse switching.

For the $NaYF_4:Er^{3+}$ upconversion nanocrystals, a new hybrid UCNPs/Polymers device structure was proposed to harvest 1.5-μm-wavelength as a low-cost and flexible SWIR photodetector. This hybrid device has a fast response time of 80 μs under the illumination of 1.5-μm-wavelength light. Owing to the effective up-conversion capability of the UCNPs, the

flexible hybrid device can possess a 0.44 mA/W responsivity at a low laser power of ~ 0.1 μW.

These results along with their characters of solution-process and absence of toxic heavy metal elements make these hybrid photodetectors promising candidates for new strategies towards a low-cost and wearable SWIR photodetection technology.

Here, we also give some ideas on the future developments for these hybrid devices. In terms of the perspectives to further improve the performance of these Au-NRs based devices, possible directions include engineering methods to load more Au-NRs or other more efficient photothermal nanomaterials onto the Pt microwire, as well as the formation of modules including multiple arrays of Au-NRs/Pt devices. In terms of the perspectives to further improve the performance of hybrid UCNPs/Polymers devices, possible directions include improving the quantum yield of UCNPs by surface modification and looking for more efficient light absorbers.

# 5. Annex

## 5.1 Annex I. supporting information for Au-NRs/thermistor

We confirmed that different concentrations of Au NRs were dropped-coating onto the surface of these NTC thermistors. The SEM images of Au NRs deposited from a solution different concentrations are shown here:

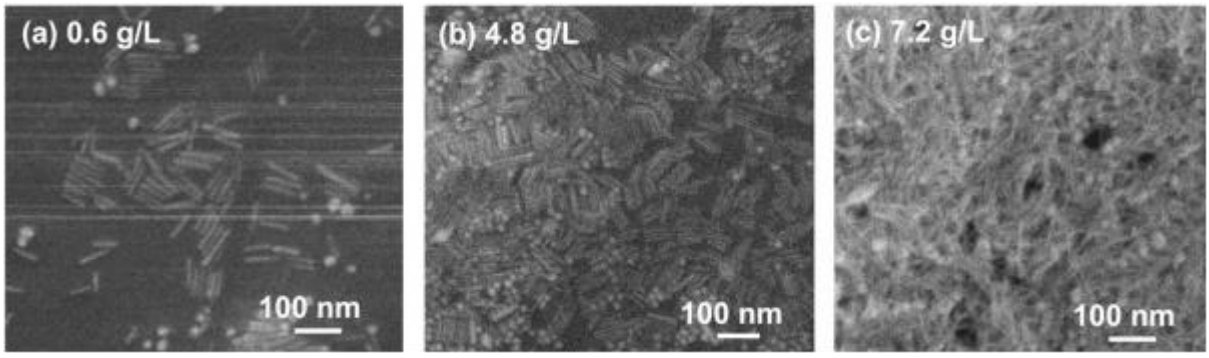


**Figure AI.1** *SEM images of Au NRs deposited on a glass substrate from 1 drop (3 L) of Au NR water solution of (a) 0.6 g/L, (b) 4.8 g/L, and (c) 7.2 g/L concentration, respectively.*

To measure the photoresponse and the resistance changes from these NTC thermistors and Au-NRs/thermistor hybrid devices, we built a measurement set-up to control the light source and collect the current signals:

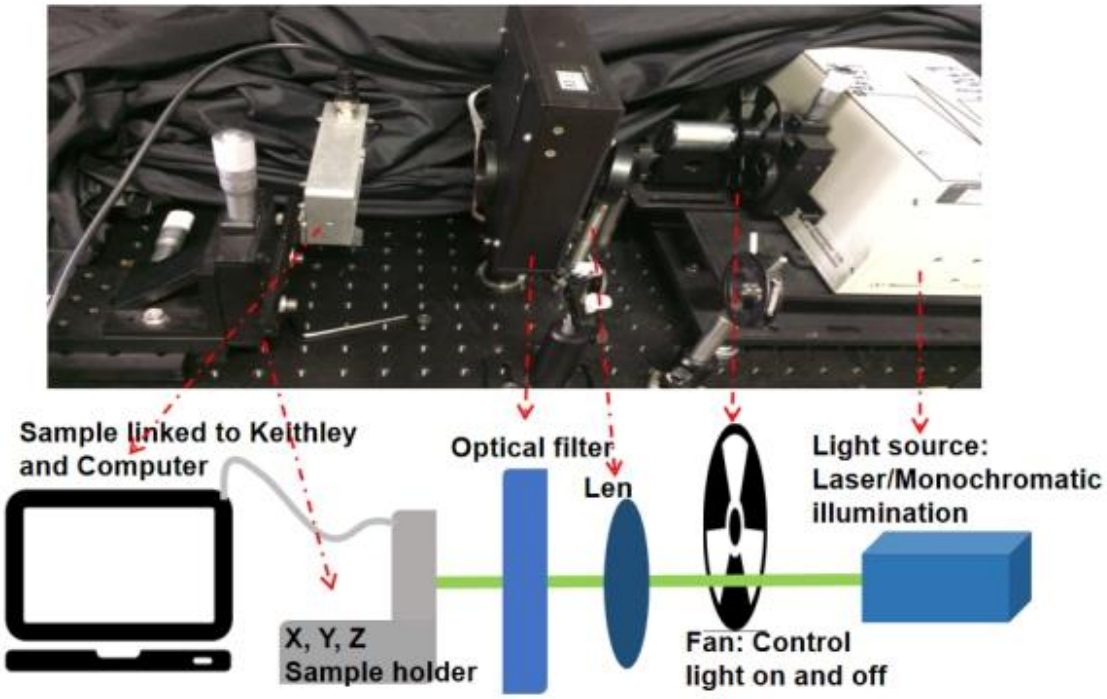


**Figure AI.2** *Experiment set-up for measuring the photorespone performance of Au-NRs/Thermistor*.

In our initial optimization process, we also measured the photorespone performance of Au NRs on some other commercial thermistors, such as NTC disc thermistor and platinum resistance Pt100 thin fill detector. They can also work, but the photoresponse was very slow, as shown on Figure AI. 3, the response time we measured in an Au-NRs/Pt100 device was larger than 15 seconds.

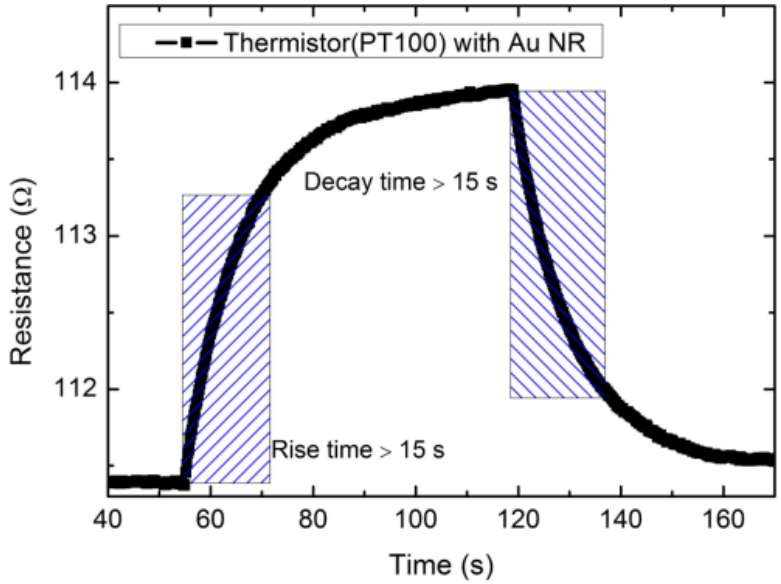


**Figure AI.3** *Response time (rise time and decay time) on an Au-NRs/Pt100 device.*

On the commercial NTC thermistors, there is a definite relation between the resistance and the temperature. Thus, in our Au-NRs/Thermistor devices, we can gain the response data and photoresponsivity on both resistance and temperature units.

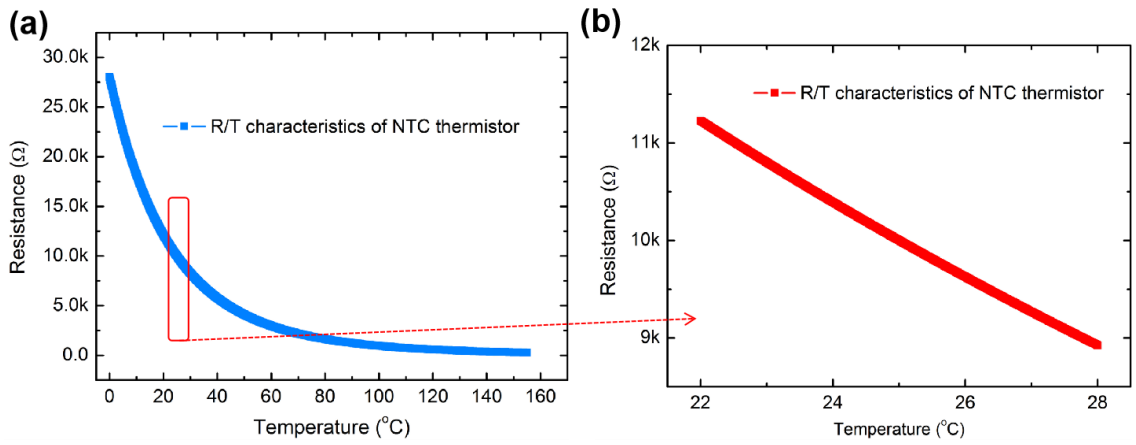


**Figure AI.4** *(a) R/T characteristics of NTC thermistor from 0 °C to 160 °C. (b) Zoom in the part of room temperature (22 °C to 28 °C), it can be regarded as a first order linear change.*

Different amounts of Au NRs can provide different photothermal capabilities, so we tried to give an optimized experiment on these Au-NRs/thermistor hybrid devices and obtain the optimal Au NRs concentration:

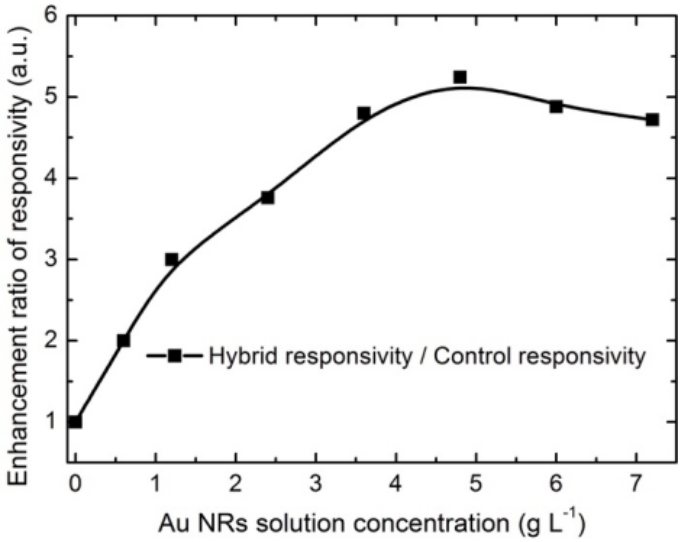


**Figure AI.5** *The enhancement ratio calculated from the photoresponsivity of an Au-NRs/thermistor hybrid device over the control device (without Au NRs) under the illumination of a laser (λ = 1.5 µm, 50 mW) for different hybrid devices fabricated by a drop (3 L) of Au NRs solution of different concentrations.*

Concerning the photothermal effect happened on all kinds of metal nanoparticles, so we fabricated a hybrid Au-NRs/thermistor device on another batch of Au NRs (sample b of Table 2.1). The obtained data is shown below. As shown in the Figure AI.6 a below, a typical hybrid device (by sample b, Table 2.1) exhibited a photoresponsivity peak from 900 nm to 1200 nm, which was in good agreement with the absorbance of this batch of nanorods drop-casted on a glass slide (shown in Figure AI.6 b). Clear photoresponse from this device was also observed under the illumination of a 975 nm laser (Figure AI.6 c). These data confirm the reproducibility of the approach of hybrid Au-NR/thermistor by the photothermal effect of Au NRs proposed in this project.

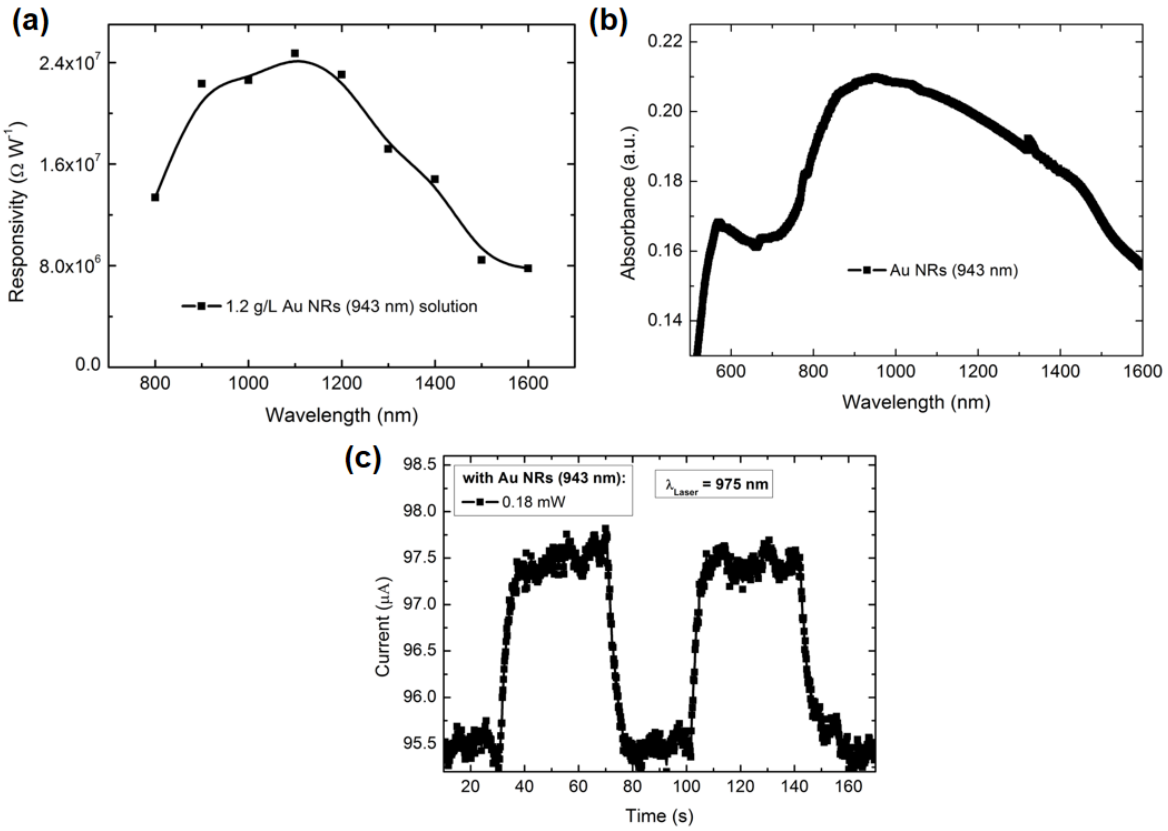


**Figure AI.6** *(a) The photoresponsivity (in Ω/W) of a typical Au-NRs/thermistor device fabricated by 1.2 g/L of Au NR solution from the batch of sample b listed in Table 2.1 (main text) over the whole wavelength window tested. All resistance was measured under a DC bias of 1 V at room-temperature. (b) Optical absorbance of this batch of Au NRs drop-casted on a glass slide. (c) Photoresponse characteristics over time of the hybrid Au-NRs/thermistor device measured in (a) under the illumination of a laser (λ = 975 nm, 0.18 mW) focused on device. The photoresponse is presented in the form of photo-induced change of measured current under a DC bias of 1V.*

Since we measured a broadband photoresponse in NIR and SWIR range, we think it is due to the near-field coupling effects, which appear when these Au NRs get very close to each other and/or in mechanical contact with each other. Thus, here we confirmed the near-field coupling effect by measuring these Au NRs in water and on glass with different concentration. As shown in Figure AI.7, when the concentration increased, the Au NRs can be more close to each other and/or more in mechanical contact with each other, so they can give a much clearer near-field coupling effect and then a broadband and red-shifted absorption.

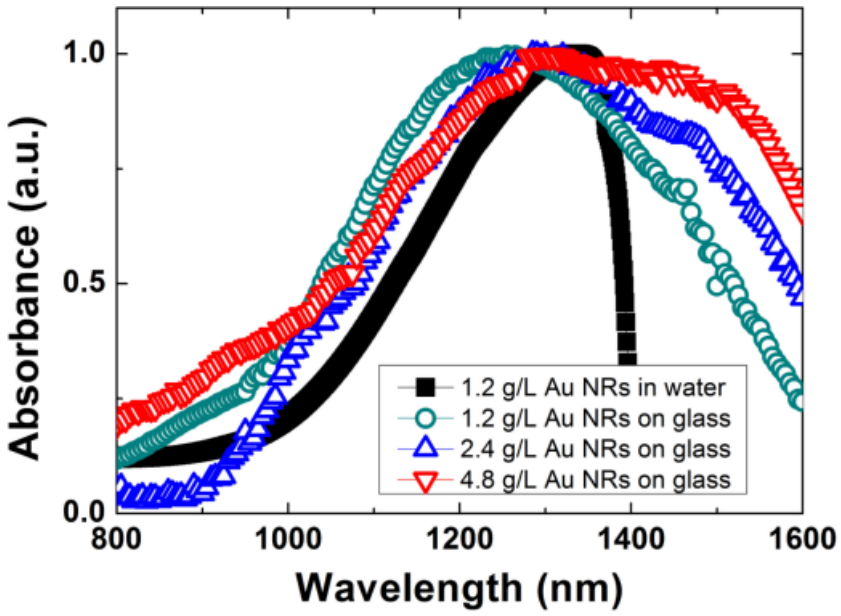


**Figure AI.7** *Absorption of Au NRs and their near-field coupling effects in water and on glass with different concentration.*

## 5.2 Annex II. Supporting information for Au-NRs/Pt device

To confirm the relationship between the resistances (ΔR) and the voltage changes (ΔV) we measured in Figure 2.25, we show here the calculation process and the formulas:

**10µm device 6_7dec2018** **AC measurements**

Lateral illumination, laser 1.537µm, laser max 380mA, spot size ≅ 10µm
We measure the resistance as a function of the laser position on the surface.

The laser is modulated. With a lock-in amplifier, we measure the voltage variations at Rdev

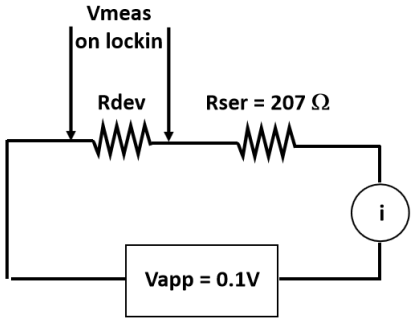


The voltage applied to the circuit is constant : Vapp = 0.1V
We have :

$$i = \frac{V_{app}}{R_{dev} + R_{ser}} \quad (1)$$

So we have:

$$V_{meas} = R_{dev} \cdot i = \frac{R_{dev} \cdot V_{app}}{R_{dev} + R_{ser}} \quad (2)$$

So :

$$R_{dev} = \frac{R_{ser} \cdot V_{meas}}{V_{app} - V_{meas}} \quad (3)$$

**Rdev= 207 x Vmeas / ( 0.1 – Vmeas )**

**Calibres:**
**220 Hz : 5 mV** **max = 4,327e-4**
**10 kHz : 5 mV**
**100 kHz : 1 mV**
**150 kHz : 1 mV**

Knowing Vmeas it is easy to calculate Rdev, in a DC mode.

In an AC mode with a lock-in amplifier, it is different.
The lock-in amplifier measures a small modulation of Vmeas.

Let us try to calculate how to convert what we measure in resistance variations.

$V_{meas} \rightarrow V_0 + \Delta V$

$R_{dev} \rightarrow R_0 + \Delta R$

So, here we gave two methods to prove the relation between the ΔR and ΔV:

## 1st method

$V_{meas} \rightarrow V_0 + \Delta V$

$R_{dev} \rightarrow R_0 + \Delta R$

With the lock-in, we measure ΔV.

**Vapp = 0,1 V**
**Rdev = R0 = 130,83 Ω**
**Rser = 207 Ω**
**I = 0,296 mA**
**V0 = 0,03873 V**

From (2), we have: $V_o + \Delta V = \frac{(R_0 + \Delta R) \cdot V_{app}}{R_0 + \Delta R + R_{ser}}$ (4)

So :

$$\Delta R = \frac{(R_{ser} + R_0) \cdot \Delta V}{V_{app} - V_0 - \Delta V}$$

$$\Delta R = \frac{337{,}83 \cdot \Delta V}{0{,}06127 - \Delta V}$$

**Rdev= 207 x Vmeas / ( 0.1 – Vmeas )**

**Calibres:**
**220 Hz : 5 mV** **max = 4,327e-4**
**10 kHz : 5 mV**
**100 kHz : 1 mV**
**150 kHz : 1 mV**

If we neglect ΔV in the bottom (small variation), we have : $\Delta R \cong 5513{,}79 \cdot \Delta V$

## 2nd method

We take the derivative of (2) $\frac{dV}{dR_{dev}} = \frac{V_{app}}{R_{dev} + R_{ser}} - \frac{R_{dev} \cdot V_{app}}{(R_{dev} + R_{ser})^2}$

$$dR_{dev} = \frac{dV}{\frac{V_{app} \cdot (R_{dev} + R_{ser})}{(R_{dev} + R_{ser})^2} - \frac{R_{dev} \cdot V_{app}}{(R_{dev} + R_{ser})^2}} = \frac{dV}{i \cdot \frac{R_{ser}}{R_{dev} + R_{ser}}}$$

We find the same relation $dR_{dev} \cong 5513{,}79 \cdot dV$

We had to take into account of the lock-in acquisition calibers.

For the device, we had : 5 mV for 220 Hz, 5mV for 50 kHz and 1mV for 100 kHz

For the control device, we had :1 mV for 220 Hz, 200µV for 10 kHz and 200µV for 100 kHz

The scales in the images above have been corrected for the different calibers used and they have been converted as if the measurements had been performed with the 5 mV caliber. So we can compare them.

**However, we have to know that : the lock-in converts the full scale of its caliber (for instance 5mV) to 10 V. That means that 1 V measured corresponds to 500µV if the caliber is 5mV.**

**To convert the above scales into Ω, we have to use the formula $dR_{dev} \cong 5513{,}79 \cdot dV$ divided by 2000.**

The scales of the above images can be converted into Ω by using : $\Delta R_{dev} \cong 2{,}7565 \cdot \Delta V$

Prior to testing these Au-NRs/Pt devices, we firstly confirmed that Au NRs can be deposited relatively uniformly on Pt microwires. From the SEM images, we can observe that the Au NRs film is well deposited on Pt microwire.

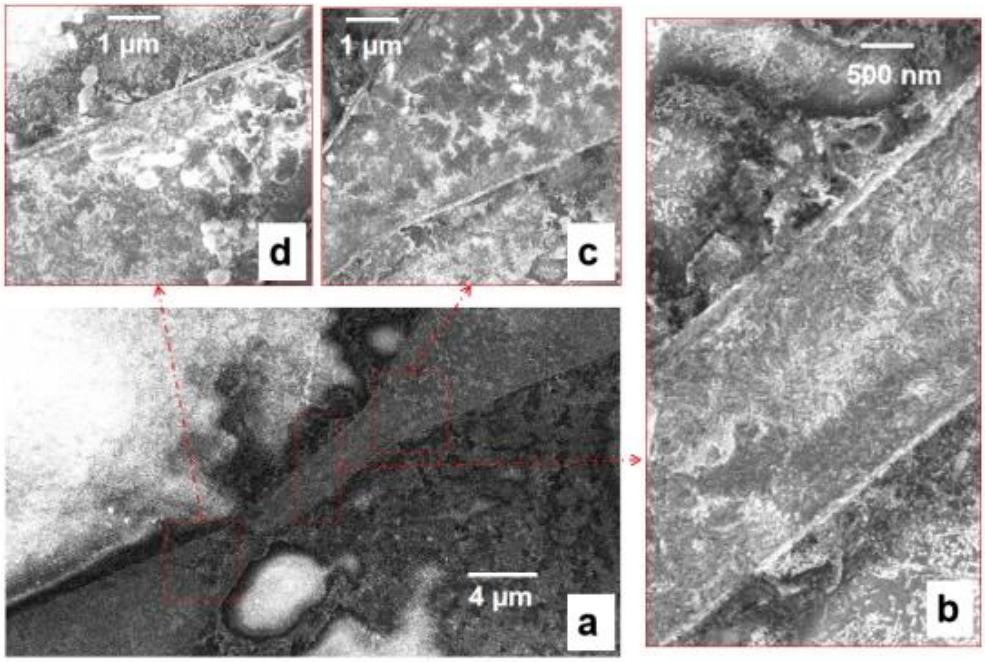


**Figure AII.1** *(a) SEM characterization of colloidal Au NRs deposited onto the Au-NR/Pt device. Three different zones (b, c and d) of the device were confirmed.*

About these thermal devices (like the devices in this work: Au-NR/Pt devices), please note that these photodetectors are resistive devices. Therefore, the presented photoresponsivity of this work is different from those of a photoconductive or photovoltaic device on which the photoresponsivity is typically given by the change of measured current (ΔI) normalized by the laser power (P), i.e. ΔI/P in the unit of A/W.

Under a laser power of 0.2 mW, the measured photoresponsivity of the current device reached 4500 /W, this is equivalent to a responsivity of 340 mA/W (under a DC bias of 1V), as shown in Figure AII.2. To facilitate comparison to other works, this figure (Photoresponsivity in terms of R/P (Ω/W) and the corresponding (ΔI)/P (mA/W) under a DC bias of 1V (P = laser power)) was put at below:

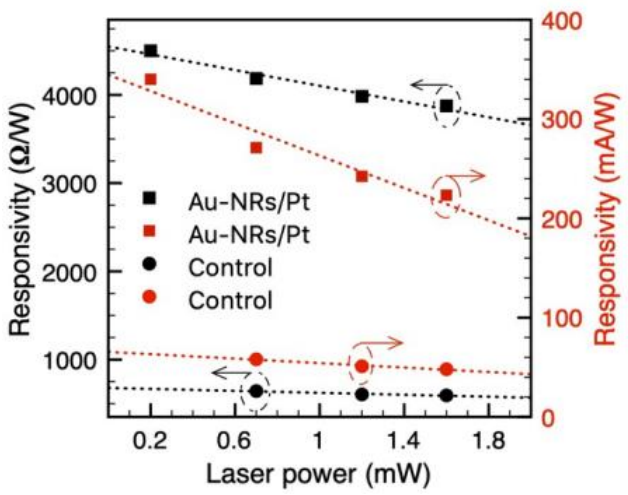


**Figure AII.2** *The photoresponsivity (in terms of R/P (Ω/W), P = laser power) and the corresponding (ΔI)/P (mA/W) under a DC bias of 1V (P = laser power) of the Au-NRs/Pt device and the control device at different laser powers. The dash lines represent the linear fit of the data.*

To confirm the contribution of the Pt structure, especially the 10 µm zone, we show here the normalized voltage drop for different frequencies:

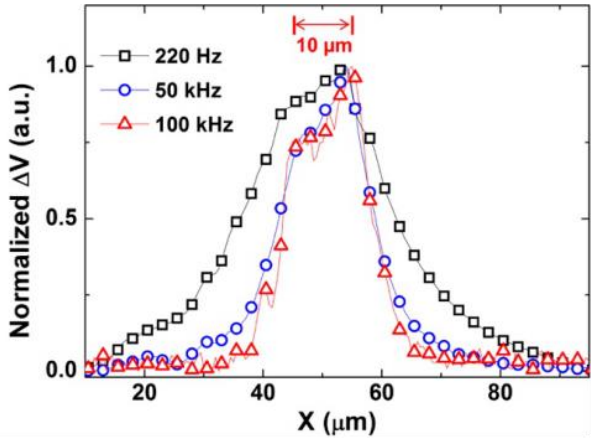


**Figure AII.3** *The normalized voltage drop for different frequencies measured on the Au-NRs/Pt device shown in Figure 4 of the main text allowing the comparison on its spatial distribution.*

We also show here the performance and characterization of other devices based on 20-µm and 30-µm sized Pt microwires. We examined the morphology and photoresponse of Au-NRs/Pt devices fabricated with a 20-µm-long and a 30-µm-long Pt microwire (Figure AII.4, AII.5 and AII.6). Similar characteristics were observed in these devices compared to the 10-µm devices described in the main text.

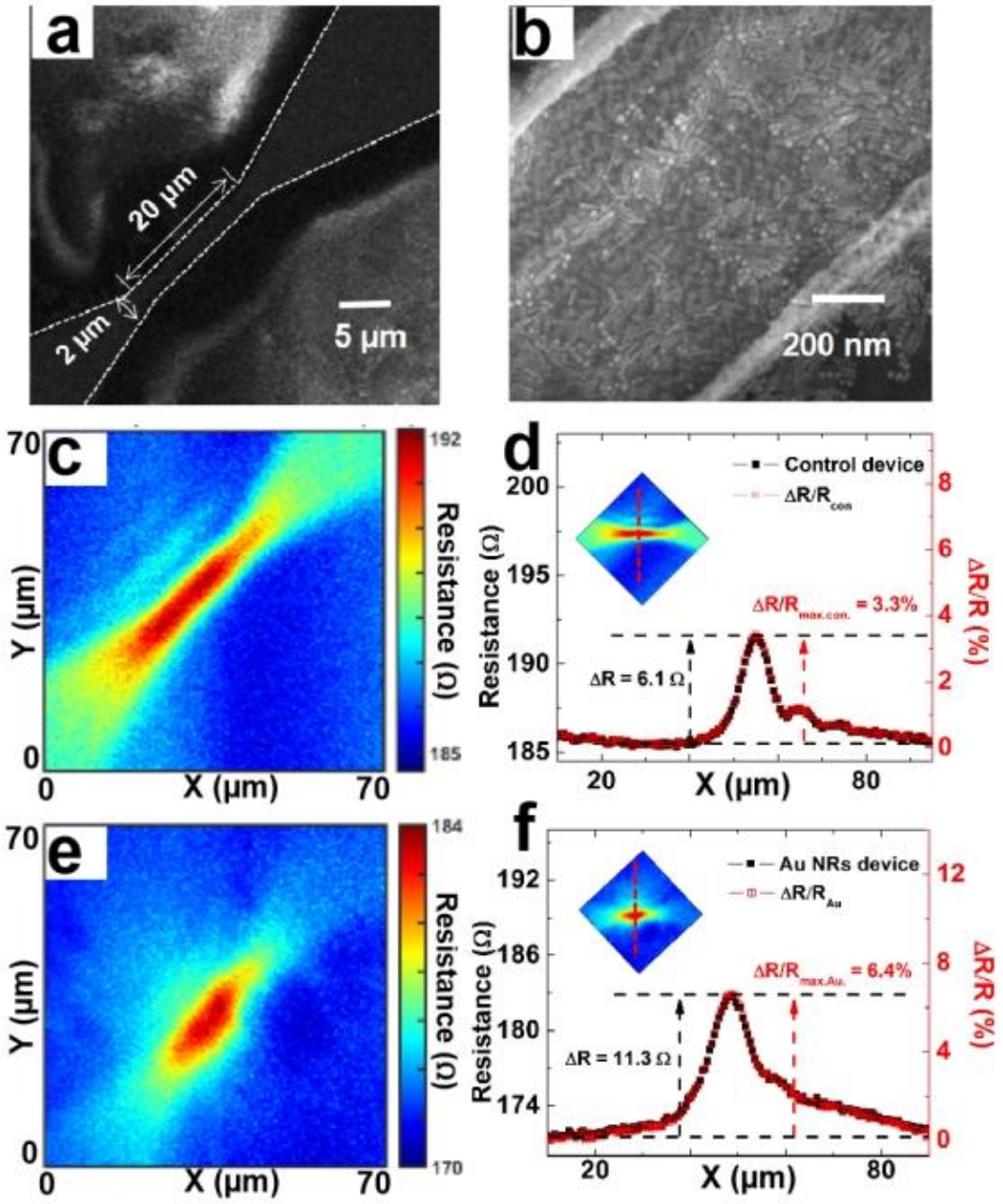


Figure AII.4 (a) SEM characterization of an Au-NRs/Pt device with a 20 µm-long and 2 µm-wide Pt microwire. (b) SEM image visualizing the Au NRs coated onto the Au-NRs/Pt device. (c) and (e) Resistance mapping of the control device (c) and the Au-NRs/Pt device (e) under a continuous 10-µm-spot laser illumination (l = 1.5 µm). (d) and (f) The cross-sectional

profiles extracted from the mapping images shown in (c) and (e) and the resultant device response in terms of ΔR or ΔR/R of the control device (d) and the Au-NRs/Pt device (f).

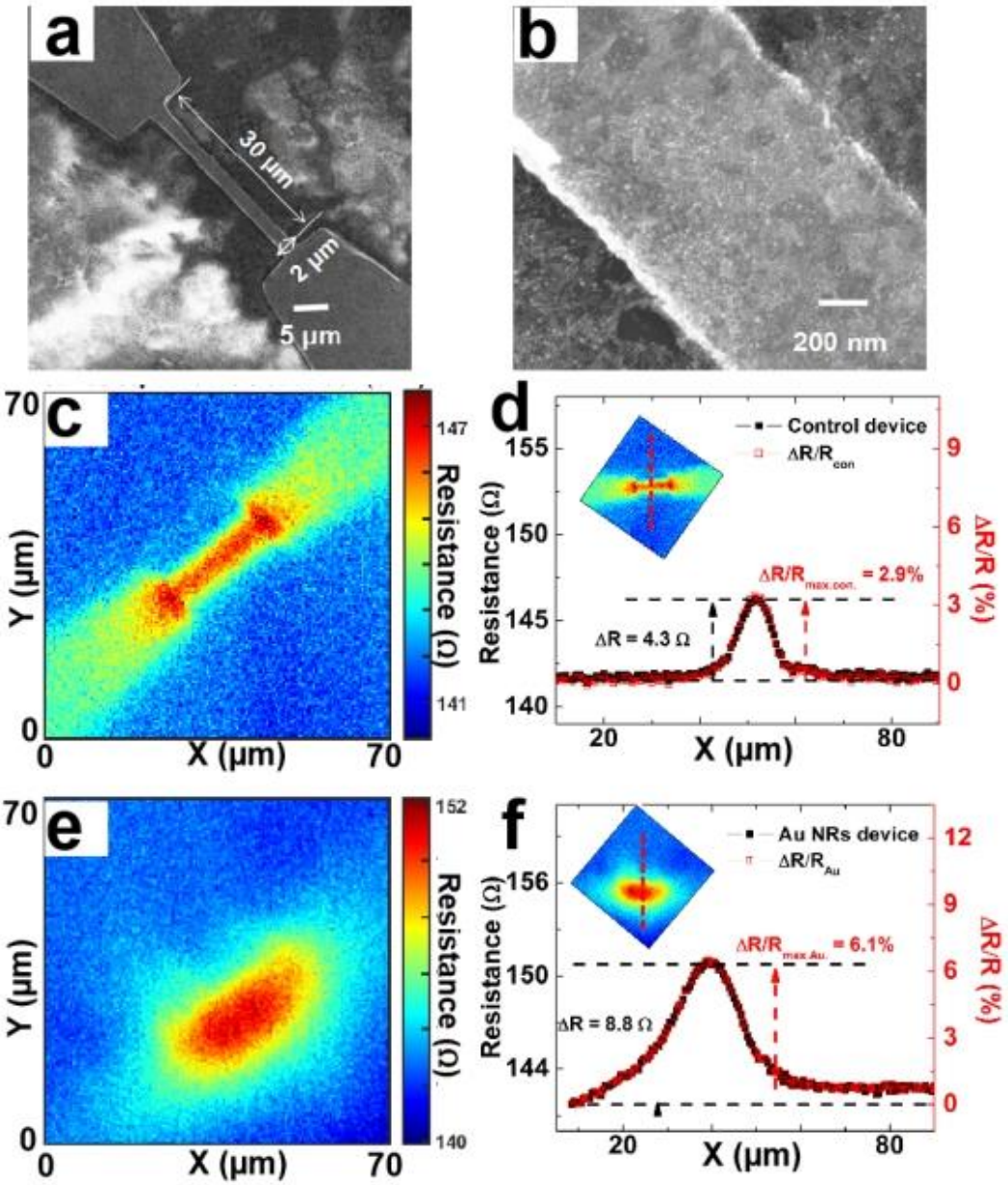


**Figure AII.5** *(a) SEM characterization of an Au-NRs/Pt device with a 30 µm-long and 2 µm-wide Pt microwire. (b) SEM image visualizing the Au NRs coated onto the Au-NRs/Pt device. (c) and (e) Resistance mapping of the control device (c) and the Au-NRs/Pt device (e) under a continuous 10-µm-spot laser illumination (l = 1.5 µm). (d) and (f) The cross-sectional profiles extracted from the mapping images shown in (c) and (e) and the resultant device response in terms of ΔR or ΔR/R of the control device (d) and the Au-NRs/Pt device (f).*

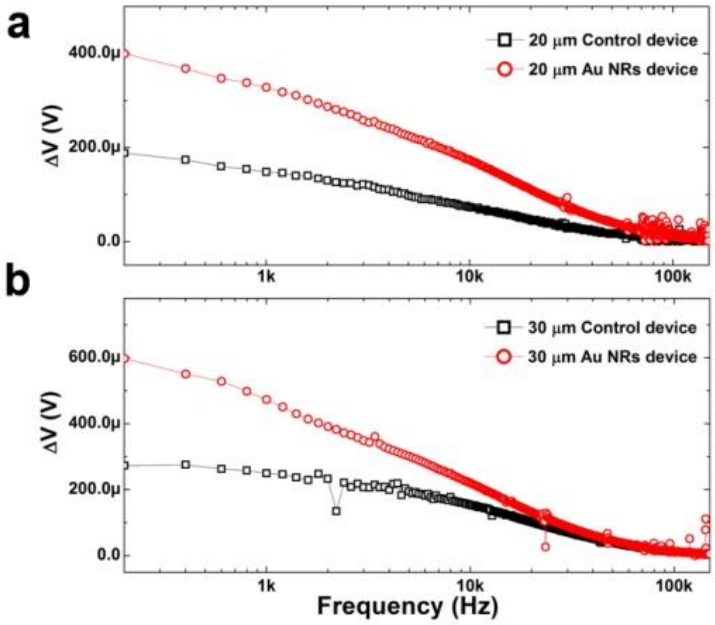


**Figure AII.6** *Evolution of the photoresponse as a function of laser modulation frequency from 200 Hz to 150 kHz for (a) the 20-um control and 20-um Au-NRs/Pt device and (b) the 30-um control and 30-um Au-NRs/Pt device.*

For this kind of photodetector based on resistance changing, like Au-NRs/thermistor and Au-NRs/Pt devices in our project, we think that a normalized metric (%/W, meaning the (ΔR/R)/P, R = resistance, P = laser power) can be used to compare their detection performance. Here we gave a comparison figure on our Au-NRs/thermistor and Au-NRs/Pt devices by using the %/W photoresponsivity as a function of laser power, as shown in Figure AII.7.

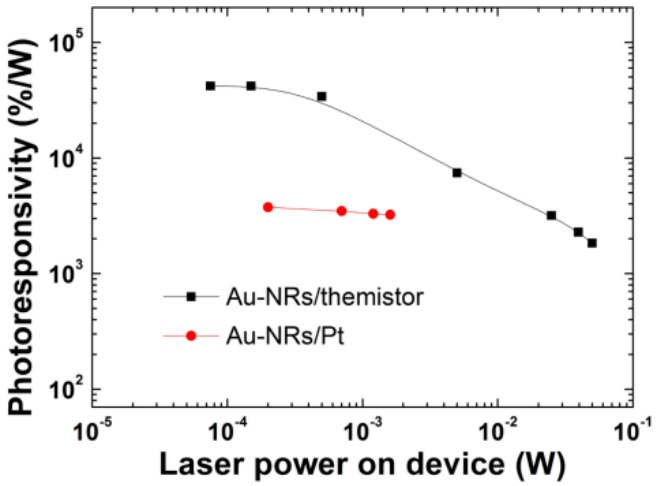


**Figure AII.7** *Comparison of their photoresponsivity (%/W) on Au-NRs/thermistor and Au-NRs/Pt devices.*

## 5.3 Annex III. Supporting information for UCNPs/Polymer device

Size and morphology of the 300 nm sized $NaYF_4:Er^{3+}$ UNCPs measured by TEM:

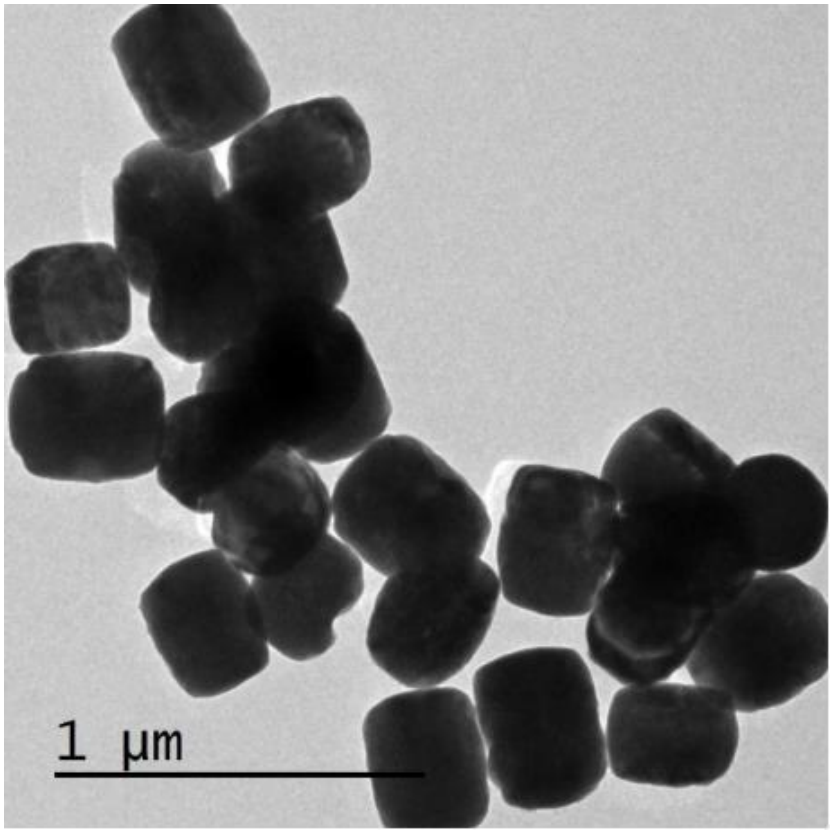


**Figure AIII.1** *TEM image of the 300 nm sized $NaYF_4:Er^{3+}$ UNCPs.*

Here we gave a diagram showing that the citrate concentration can tune the UCNPs size very effectively.

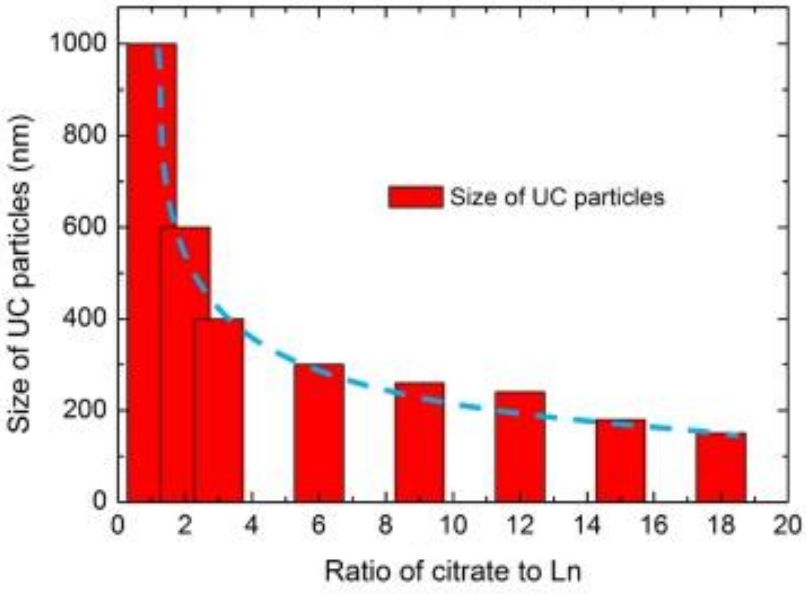


**Figure AIII.2** *Relationship between citrate concentration and UCNPs size.*

For the measurement of the upconversion fluorescence quantum yield (QY), we built a set-up (Figure AIII.3) based on an integrating sphere by following a method established in Ref.

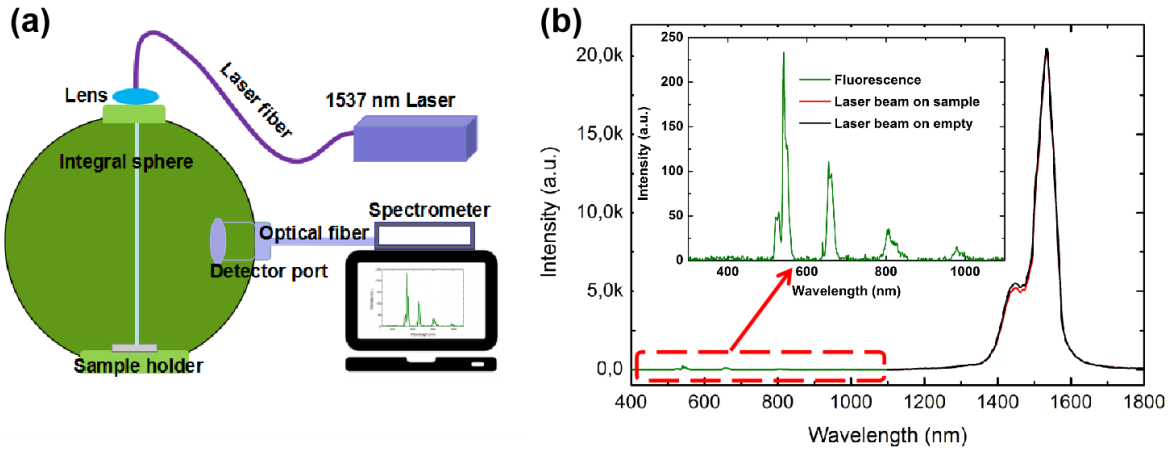


**Figure AIII.3** *(a) Schematic diagram for the measurement of the upconversion fluorescence QY. (b) A fluorescence intensity of exciting light and emitting lights from 300 nm sized UCNPs.*

After collecting the fluorescence intensity of these exciting and emitting lights, we can calculate the QY (ŋ) by the following formula.

$$\eta = P_b/(L_a - L_b)$$

Here, the spectrum is multiplied at each value by the wavelength and then the peaks are integrated to yield values proportional to the number of photons in the excitation peak, L, and photo luminescence peak, P.

To measure the upconversion fluorescence spectrum on a single NaYF4:Er3+ NP, we built a set-up linking to a CCD camera coupled with a monochromator (HORIBA Jobin Yvon). The set-up and the single NP were shown in Figure AIII.4.

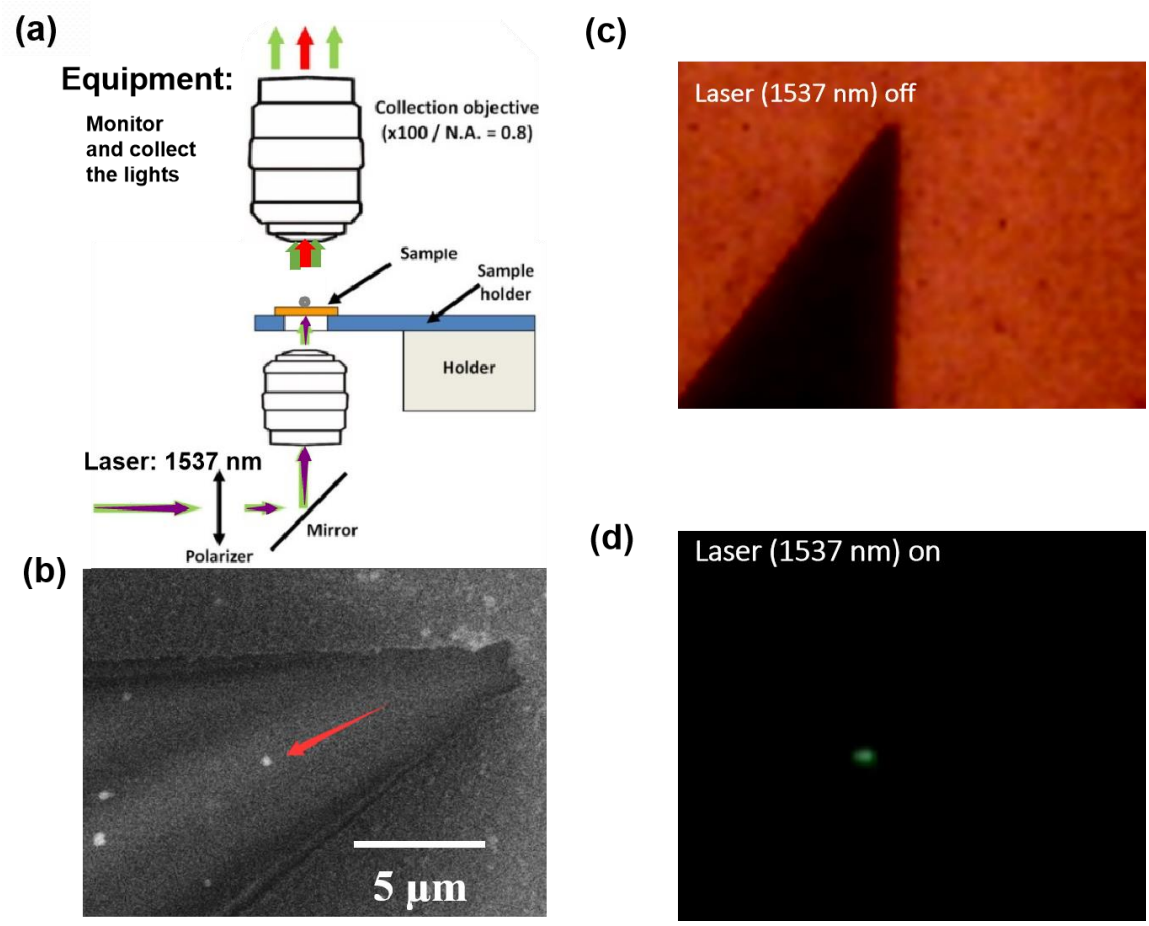


**Figure AIII.4** *(a) Schematic diagram for the measurement of the upconversion fluorescence from a single UCNP. (b) SEM image of 300 nm sized UCNPs. (c) A dark single UCNP under the microscope with the laser (1537 nm) off. (d) A luminous single UCNP under the microscope with the laser (1537 nm) on.*

We confirmed that different concentrations of Au NRs were introduced into the organic films in these photodetectors. The SEM images of these hybrid films with different concentrations of UCNPs are shown here:

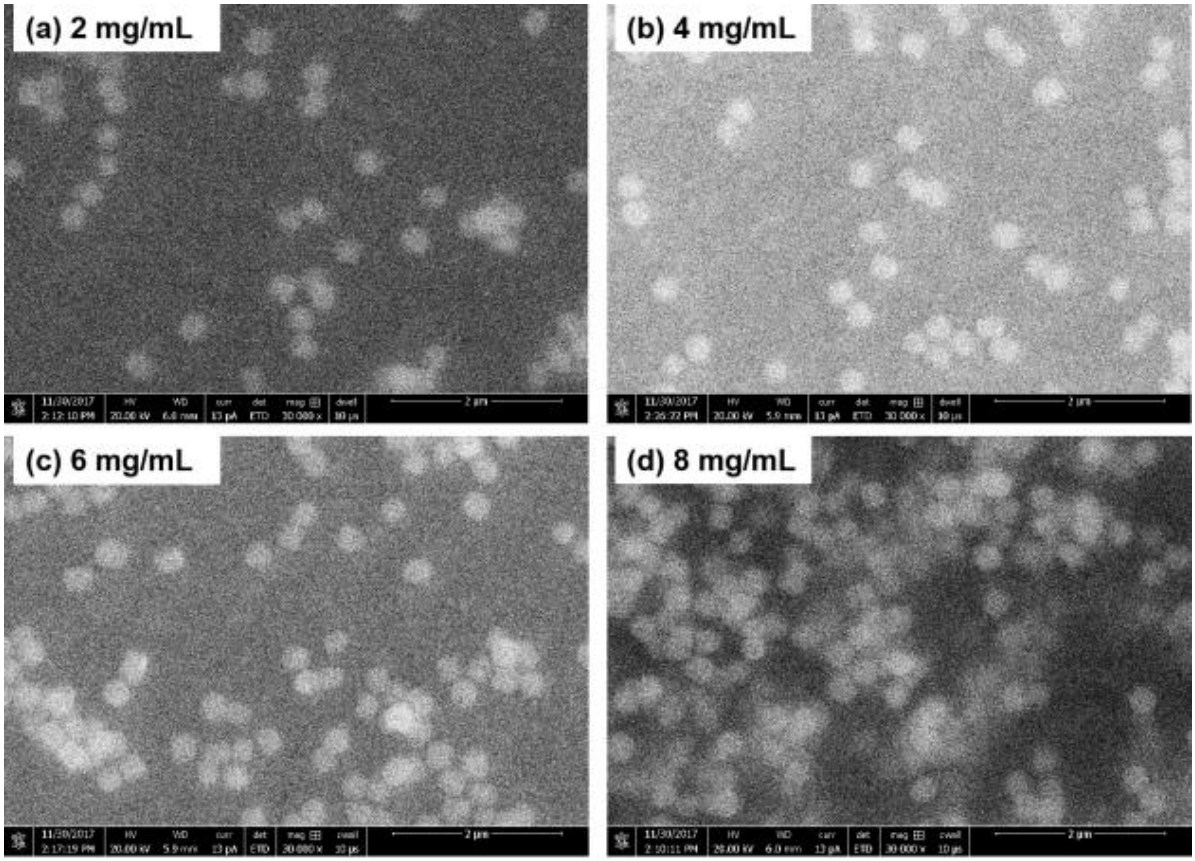


**Figure AIII.5** *SEM images of UCNPs/Polymer films with different concentrations: a) 2 g/L, b) 4 g/L, c) 6 g/L and d) 8 g/L. The scale bar is 2 µm.*

Here, we also confrimed that there is a linear relationship between the emitting fluorescence intensity and the laser power, as shown in Figure AIII.6:

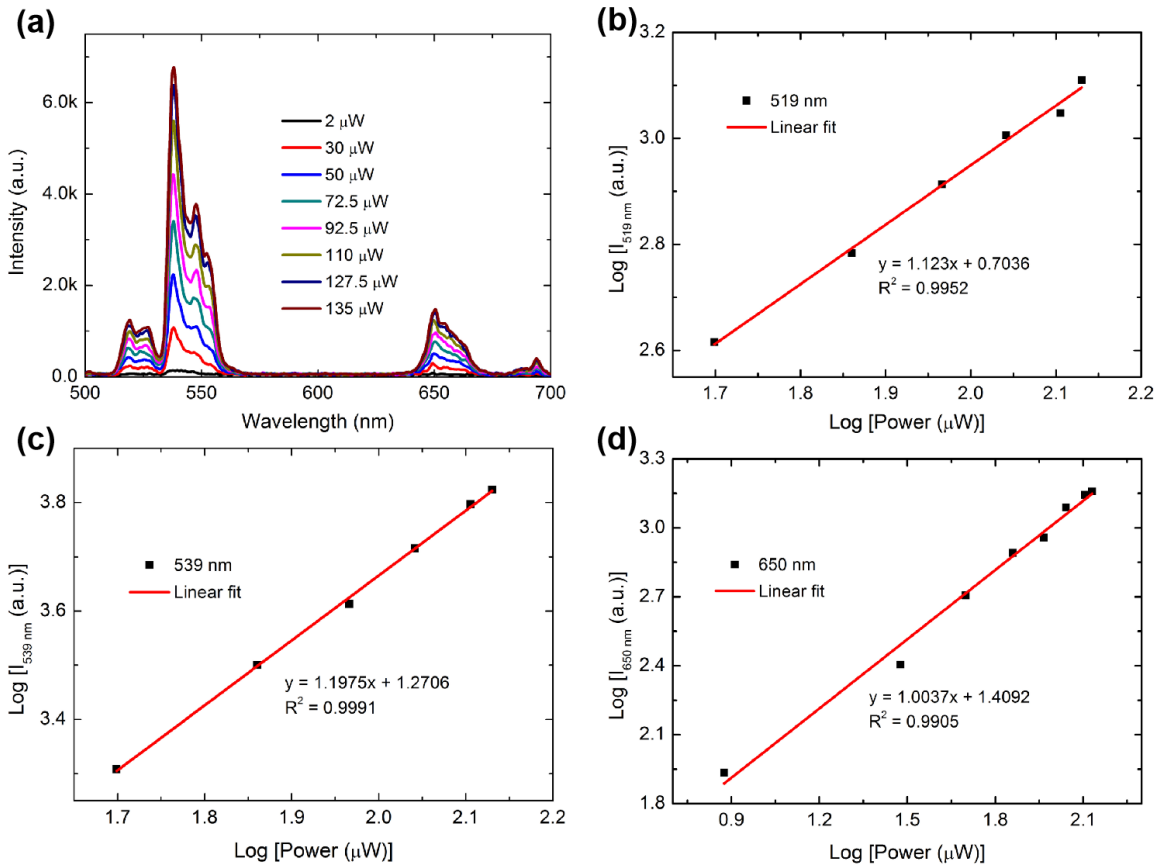


**Figure AIII.6** *(a) Upconversion fluorescence intensity from a single UCNP as a function of laser power. (b) Linear relationship between the 519 nm (emitting peak) fluorescence intensity and the laser power. (c) Linear relationship between the 539 nm (emitting peak) fluorescence intensity and the laser power. (d) Linear relationship between the 650 nm (emitting peak) fluorescence intensity and the laser power.*

# 6. Publications

*1)* **Hengyang Xiang**, Tingting Niu, Mathilde Schoenauer Sebag, Zhelu Hu, Xiangzhen Xu, Laurent Billot, Lionel Aigouy and Zhuoying Chen, *"Short-Wave Infrared Sensor by the Photothermal Effect of Colloidal Gold Nanorods"*, **Small 2018**, 14(16), 1704013.

2) **Hengyang Xiang**, Hungju Lin, Tingting Niu, Zhuoying Chen and Lionel Aigouy, *"Nanoscale thermal characterization of high aspect ratio gold nanorods for photothermal applications at λ = 1.5 μ m",* **Journal of Applied Physics 2019**, 125(16):163101.

*3)* **Hengyang Xiang**, Hungju Lin, Laurent Billot, Lionel Aigouy and Zhuoying Chen, *"Hybrid Plasmonic Gold-Nanorod-Platinum Short-Wave Infrared Photodetectors with Fast Response",* **Nanoscale 2019, online.**

*4)* **Hengyang Xiang**, Zhelu Hu, Laurent Billot, Lionel Aigouy, Weiming Zhang, Iain Mcculloch, and Zhuoying Chen, *"Heavy-Metal-Free Flexible Hybrid Organic-Nanocrystal Photodetectors Sensitive to 1.5-μm-wavelength",* **ACS Applied Materials & Interfaces 2019, in submitted.**

*5)* **Hengyang Xiang**, Chenghao Xin, Laurent Billot, Zhuoying Chen and Lionel Aigouy, *"Fast Thermal Response Behavior of Submicron Platinum Stripe",* **in manuscript.**

6) Zhelu Hu, **Hengyang Xiang**, Mathilde Schoenauer Sebag, Laurent Billot, Lionel Aigouy, and Zhuoying Chen. *"Compact layer free mixed-cation lead mixed-halide perovskite solar cells"*. **Chemical Communications, 2018**, vol. 54, no 21, p. 2623-2626.

7) Mathilde Schoenauer Sebag, Zhelu Hu, Karmel de Oliveira Lima, **Hengyang Xiang**, Patrick Gredin, Michel Mortier, Laurent Billot, Lionel Aigouy, and Zhuoying Chen. *"Microscopic Evidence of Upconversion-Induced Near-Infrared Light Harvest in Hybrid Perovskite Solar Cells"*. **ACS Applied Energy Materials, 2018**.

8) David Becker-Koch, Boris Rivkin, Fabian Paulus, **Hengyang Xiang**, Yifan Dong, Zhuoying Chen, Artem A Bakulin and Yana Vaynzof. *"Probing charge transfer states at organic and hybrid internal interfaces by photothermal deflection spectroscopy"*. **Journal of Physics: Condensed Matter, 2018**.

# 7. References


(1) Sicard, M.; Thome, K. J.; Crowther, B. G.; Smith, M. W. Shortwave Infrared Spectroradiometer for Atmospheric Transmittance Measurements. *J. Atmos. Ocean. Technol.* **1998**, *15* (1), 174–183. https://doi.org/10.1175/1520-0426(1998)015<0174:SISFAT>2.0.CO;2.

(2) Vidot, J.; Landgraf, J.; Hasekamp, O. P.; Butz, A.; Galli, A.; Tol, P.; Aben, I. Carbon Monoxide from Shortwave Infrared Reflectance Measurements: A New Retrieval Approach for Clear Sky and Partially Cloudy Atmospheres. *Remote Sens. Environ.* **2012**, *120*, 255–266. https://doi.org/10.1016/j.rse.2011.09.032.

(3) Hong, G.; Antaris, A. L.; Dai, H. Near-Infrared Fluorophores for Biomedical Imaging. *Nat. Biomed. Eng.* **2017**, *1* (1), 0010. https://doi.org/10.1038/s41551-016-0010.

(4) Hansen, M. P.; Malchow, D. S. Overview of SWIR Detectors, Cameras, and Applications. In *Proc.SPIE*; 2008; Vol. 6939, p 69390I.

(5) Steven R.J. Brueck. *Seeing Photons: Progress and Limits of Visible and Infrared Sensor Arrays*; 2010.

(6) Du, H.; Lin, X.; Xu, Z.; Chu, D. Recent Developments in Black Phosphorus Transistors. *J. Mater. Chem. C* **2015**, *3* (34), 8760–8775. https://doi.org/10.1039/C5TC01484K.

(7) Youngblood, N.; Chen, C.; Koester, S. J.; Li, M. Waveguide-Integrated Black Phosphorus Photodetector with High Responsivity and Low Dark Current. *Nat. Photonics* **2015**, *9* (4), 247. https://doi.org/10.1038/nphoton.2015.23.

(8) Xia, F.; Mueller, T.; Lin, Y.; Valdes-Garcia, A.; Avouris, P. Ultrafast Graphene Photodetector. *Nat. Nanotechnol.* **2009**, *4* (12), 839.

(9) Mueller, T.; Xia, F.; Avouris, P. Graphene Photodetectors for High-Speed Optical Communications. *Nat. Photonics* **2010**, *4* (5), 297. https://doi.org/10.1038/nphoton.2010.40.

(10) Cakmakyapan, S.; Lu, P. K.; Navabi, A.; Jarrahi, M. Gold-Patched Graphene Nano-Stripes for High-Responsivity and Ultrafast Photodetection from the Visible to Infrared Regime. *Light Sci. Appl.* **2018**, *7* (1), 20. https://doi.org/10.1038/s41377-018-0020-2.

(11) Xie, Y.; Zhang, B.; Wang, S.; Wang, D.; Wang, A.; Wang, Z.; Yu, H.; Zhang, H.; Chen, Y.; Zhao, M.; et al. Ultrabroadband MoS2 Photodetector with Spectral Response from 445 to 2717 Nm. *Adv. Mater.* **2017**, *29* (17), 1605972. https://doi.org/10.1002/adma.201605972.

(12) Saran, R.; Curry, R. J. Lead Sulphide Nanocrystal Photodetector Technologies. *Nat. Photonics* **2016**, *10* (2), 81. https://doi.org/10.1038/nphoton.2015.280.

(13) Kufer, D.; Nikitskiy, I.; Lasanta, T.; Navickaite, G.; Koppens, F. H. L.; Konstantatos, G. Hybrid 2D-0D MoS2-PbS Quantum Dot Photodetectors. *Adv. Mater.* **2015**, *27* (1), 176–180. https://doi.org/10.1002/adma.201402471.

(14) Clavero, C. Plasmon-Induced Hot-Electron Generation at Nanoparticle/Metal-Oxide Interfaces for Photovoltaic and Photocatalytic Devices. *Nat. Photonics* **2014**, *8* (2), 95.

(15) Mas-Ballesté, R.; Gómez-Navarro, C.; Gómez-Herrero, J.; Zamora, F. 2D Materials: To Graphene and Beyond. *Nanoscale* **2011**, *3* (1), 20–30. https://doi.org/10.1039/c0nr00323a.

(16) Avouris, P. Graphene: Electronic and Photonic Properties and Devices. *Nano Lett.* **2010**, *10* (11), 4285–4294. https://doi.org/10.1021/nl102824h.

(17) Bonaccorso, F.; Sun, Z.; Hasan, T.; Ferrari, A. C. Graphene Photonics and Optoelectronics. *Nat. Photonics* **2010**, *4* (9), 611.

(18) Pospischil, A.; Humer, M.; Furchi, M. M.; Bachmann, D.; Guider, R.; Fromherz, T.; Mueller, T. CMOS-Compatible Graphene Photodetector Covering All Optical Communication Bands. *Nat. Photonics* **2013**, *7* (11), 892.

(19) Gan, X.; Shiue, R.-J.; Gao, Y.; Meric, I.; Heinz, T. F.; Shepard, K.; Hone, J.; Assefa, S.; Englund, D. Chip-Integrated Ultrafast Graphene Photodetector with High Responsivity. *Nat. Photonics* **2013**, *7* (11), 883.

(20) Tan, C. L.; Hooman, M. Emerging Technologies for High Performance Infrared Detectors. *Nanophotonics*. 2018, p 169. https://doi.org/10.1515/nanoph-2017-0061.

(21) Li, W.; Valentine, J. Metamaterial Perfect Absorber Based Hot Electron Photodetection. *Nano Lett.* **2014**, *14* (6), 3510–3514. https://doi.org/10.1021/nl501090w.

(22) Geng, Y.; Wang, S. J.; Kim, J. K. Preparation of Graphite Nanoplatelets and Graphene Sheets. *J. Colloid Interface Sci.* **2009**, *336* (2), 592–598. https://doi.org/10.1016/j.jcis.2009.04.005.

(23) Giustino, F.; Snaith, H. J. Toward Lead-Free Perovskite Solar Cells. *ACS Energy Lett.* **2016**, *1* (6), 1233–1240. https://doi.org/10.1021/acsenergylett.6b00499.

(24) Noel, N. K.; Stranks, S. D.; Abate, A.; Wehrenfennig, C.; Guarnera, S.; Haghighirad, A.

A.; Sadhanala, A.; Eperon, G. E.; Pathak, S. K.; Johnston, M. B.; et al. Lead-Free Organic-Inorganic Tin Halide Perovskites for Photovoltaic Applications. *Energy Environ. Sci.* **2014**, *7* (9), 3061–3068. https://doi.org/10.1039/c4ee01076k.

(25) Konstantatos, G. Current Status and Technological Prospect of Photodetectors Based on Two-Dimensional Materials. *Nat. Commun.* **2018**, *9* (1), 5266. https://doi.org/10.1038/s41467-018-07643-7.

(26) Chen, H.; Shao, L.; Li, Q.; Wang, J. Gold Nanorods and Their Plasmonic Properties. *Chem. Soc. Rev.* **2013**, *42* (7), 2679-2724. https://doi.org/10.1039/c2cs35367a.

(27) Sharma, V.; Park, K.; Srinivasarao, M. Colloidal Dispersion of Gold Nanorods: Historical Background, Optical Properties, Seed-Mediated Synthesis, Shape Separation and Self-Assembly. *Mater. Sci. Eng. R Reports* **2009**, *65* (1), 1–38. https://doi.org/https://doi.org/10.1016/j.mser.2009.02.002.

(28) Amendola, V.; Pilot, R.; Frasconi, M.; Maragò, O. M.; Iatì, M. A. Surface Plasmon Resonance in Gold Nanoparticles: A Review. *J. Phys. Condens. Matter* **2017**, *29* (20), 203002. https://doi.org/10.1088/1361-648x/aa60f3.

(29) Cao, J.; Sun, T.; Grattan, K. T. V. Gold Nanorod-Based Localized Surface Plasmon Resonance Biosensors: A Review. *Sensors Actuators B Chem.* **2014**, *195*, 332–351. https://doi.org/https://doi.org/10.1016/j.snb.2014.01.056.

(30) Yang, P.; Zheng, J.; Xu, Y.; Zhang, Q.; Jiang, L. Colloidal Synthesis and Applications of Plasmonic Metal Nanoparticles. *Adv. Mater.* **2016**, *28* (47), 10508–10517. https://doi.org/10.1002/adma.201601739.

(31) Christopher, P.; Xin, H.; Linic, S. Visible-Light-Enhanced Catalytic Oxidation Reactions on Plasmonic Silver Nanostructures. *Nat. Chem.* **2011**, *3* (6), 467. https://doi.org/10.1038/nchem.1032.

(32) Cao, L.; Barsic, D. N.; Guichard, A. R.; Brongersma, M. L. Plasmon-Assisted Local Temperature Control to Pattern Individual Semiconductor Nanowires and Carbon Nanotubes. *Nano Lett.* **2007**, *7* (11), 3523–3527. https://doi.org/10.1021/nl0722370.

(33) Wang, F.; Li, C.; Chen, H.; Jiang, R.; Sun, L. D.; Li, Q.; Wang, J.; Yu, J. C.; Yan, C. H. Plasmonic Harvesting of Light Energy for Suzuki Coupling Reactions. *J. Am. Chem. Soc.* **2013**, *135* (15), 5588–5601. https://doi.org/10.1021/ja310501y.

(34) Xiong, Y.; Long, R.; Liu, D.; Zhong, X.; Wang, C.; Li, Z. Y.; Xie, Y. Solar Energy Conversion with Tunable Plasmonic Nanostructures for Thermoelectric Devices. *Nanoscale* **2012**, *4* (15), 4416–4420. https://doi.org/10.1039/c2nr30208j.

(35) Quint, M. T.; Delgado, S.; Paredes, J. H.; Nuno, Z. S.; Linda, S.; Ghosh, S. All-Optical

Switching of Nematic Liquid Crystal Films Driven by Localized Surface Plasmons. *Opt. Express* **2015**, *23* (5), 6888–6895. https://doi.org/10.4231/D3G73746M.

(36) Espinosa, A.; Bugnet, M.; Radtke, G.; Neveu, S.; Botton, G. A.; Wilhelm, C.; Abou-Hassan, A. Can Magneto-Plasmonic Nanohybrids Efficiently Combine Photothermia with Magnetic Hyperthermia? *Nanoscale* **2015**, *7* (45), 18872–18877. https://doi.org/10.1039/C5NR06168G.

(37) Jaque, D.; Martínez Maestro, L.; del Rosal, B.; Haro-Gonzalez, P.; Benayas, A.; Plaza, J. L.; Martín Rodríguez, E.; García Solé, J. Nanoparticles for Photothermal Therapies. *Nanoscale* **2014**, *6* (16), 9494–9530. https://doi.org/10.1039/C4NR00708E.

(38) Ju, Y.; Zhang, H.; Yu, J.; Tong, S.; Tian, N.; Wang, Z.; Wang, X.; Su, X.; Chu, X.; Lin, J.; et al. Monodisperse Au-Fe2C Janus Nanoparticles: An Attractive Multifunctional Material for Triple-Modal Imaging-Guided Tumor Photothermal Therapy. *ACS Nano* **2017**, *11* (9), 9239–9248. https://doi.org/10.1021/acsnano.7b04461.

(39) Sun, Q.; You, Q.; Pang, X.; Tan, X.; Wang, J.; Liu, L.; Guo, F.; Tan, F.; Li, N. A Photoresponsive and Rod-Shape Nanocarrier: Single Wavelength of Light Triggered Photothermal and Photodynamic Therapy Based on AuNRs-Capped & Ce6-Doped Mesoporous Silica Nanorods. *Biomaterials* **2017**, *122*, 188–200. https://doi.org/10.1016/j.biomaterials.2017.01.021.

(40) Alkilany, A. M.; Thompson, L. B.; Boulos, S. P.; Sisco, P. N.; Murphy, C. J. Gold Nanorods: Their Potential for Photothermal Therapeutics and Drug Delivery, Tempered by the Complexity of Their Biological Interactions. *Adv. Drug Deliv. Rev.* **2012**, *64* (2), 190–199. https://doi.org/10.1016/j.addr.2011.03.005.

(41) Brongersma, M. L.; Halas, N. J.; Nordlander, P. Plasmon-Induced Hot Carrier Science and Technology. *Nat. Nanotechnol.* **2015**, *10* (1), 25.

(42) Zhang, Y.; He, S.; Guo, W.; Hu, Y.; Huang, J.; Mulcahy, J. R.; Wei, W. D. Surface-Plasmon-Driven Hot Electron Photochemistry. *Chem. Rev.* **2017**, *118* (6), 2927–2954.

(43) Huang, X.; El-Sayed, M. A. Gold Nanoparticles: Optical Properties and Implementations in Cancer Diagnosis and Photothermal Therapy. *J. Adv. Res.* **2010**, *1* (1), 13–28. https://doi.org/https://doi.org/10.1016/j.jare.2010.02.002.

(44) Auzel, F. Upconversion and Anti-Stokes Processes with f and d Ions in Solids. *Chem. Rev.* **2004**, *104* (1), 139–174. https://doi.org/10.1021/cr020357g.

(45) Suyver, J. F.; Aebischer, A.; Biner, D.; Gerner, P.; Grimm, J.; Heer, S.; Krämer, K. W.; Reinhard, C.; Güdel, H. U. Novel Materials Doped with Trivalent Lanthanides and

Transition Metal Ions Showing Near-Infrared to Visible Photon Upconversion. *Opt. Mater. (Amst).* **2005**, *27* (6), 1111–1130. https://doi.org/https://doi.org/10.1016/j.optmat.2004.10.021.

(46) Zhou, B.; Shi, B.; Jin, D.; Liu, X. Controlling Upconversion Nanocrystals for Emerging Applications. *Nat. Nanotechnol.* **2015**, *10* (11), 924.

(47) Li, D.; Ågren, H.; Chen, G. Near Infrared Harvesting Dye-Sensitized Solar Cells Enabled by Rare-Earth Upconversion Materials. *Dalt. Trans.* **2018**, *47* (26), 8526–8537. https://doi.org/10.1039/c7dt04461e.

(48) Ye, X.; Zheng, C.; Chen, J.; Gao, Y.; Murray, C. B. Using Binary Surfactant Mixtures To Simultaneously Improve the Dimensional Tunability and Monodispersity in the Seeded Growth of Gold Nanorods. *Nano Lett.* **2013**, *13* (2), 765–771. https://doi.org/10.1021/nl304478h.

(49) Sau, T. K.; Murphy, C. J. Seeded High Yield Synthesis of Short Au Nanorods in Aqueous Solution. *Langmuir* **2004**, *20* (15), 6414–6420. https://doi.org/10.1021/la049463z.

(50) Ye, X.; Jin, L.; Caglayan, H.; Chen, J.; Xing, G.; Zheng, C.; Doan-Nguyen, V.; Kang, Y.; Engheta, N.; Kagan, C. R.; et al. Improved Size-Tunable Synthesis of Monodisperse Gold Nanorods through the Use of Aromatic Additives. *ACS Nano* **2012**, *6* (3), 2804–2817. https://doi.org/10.1021/nn300315j.

(51) Nikoobakht, B.; Wang, Z. L.; El-Sayed, M. A. Self-Assembly of Gold Nanorods. *J. Phys. Chem. B* **2000**, *104* (36), 8635–8640. https://doi.org/10.1021/jp001287p.

(52) Hu, X.; Cheng, W.; Wang, T.; Wang, Y.; Wang, E.; Dong, S. Fabrication, Characterization, and Application in SERS of Self-Assembled Polyelectrolyte−Gold Nanorod Multilayered Films. *J. Phys. Chem. B* **2005**, *109* (41), 19385–19389. https://doi.org/10.1021/jp052706r.

(53) Hamon, C.; Postic, M.; Mazari, E.; Bizien, T.; Dupuis, C.; Even-Hernandez, P.; Jimenez, A.; Courbin, L.; Gosse, C.; Artzner, F.; et al. Three-Dimensional Self-Assembling of Gold Nanorods with Controlled Macroscopic Shape and Local Smectic B Order. *ACS Nano* **2012**, *6* (5), 4137–4146. https://doi.org/10.1021/nn3006027.

(54) M., F. A.; J., D. T.; Carolina, N.; Paul, M. Coupling Modes of Gold Trimer Superstructures. *Philos. Trans. R. Soc. A Math. Phys. Eng. Sci.* **2011**, *369* (1950), 3472–3482. https://doi.org/10.1098/rsta.2011.0012.

(55) Slaughter, L. S.; Wu, Y.; Willingham, B. A.; Nordlander, P.; Link, S. Effects of

Symmetry Breaking and Conductive Contact on the Plasmon Coupling in Gold Nanorod Dimers. *ACS Nano* **2010**, *4* (8), 4657–4666. https://doi.org/10.1021/nn1011144.

(56) Pramod, P.; Thomas, K. G. Plasmon Coupling in Dimers of Au Nanorods. *Adv. Mater.* **2008**, *20* (22), 4300–4305. https://doi.org/10.1002/adma.200703057.

(57) Aizpurua, J.; Bryant, G. W.; Richter, L. J.; García de Abajo, F. J.; Kelley, B. K.; Mallouk, T. Optical Properties of Coupled Metallic Nanorods for Field-Enhanced Spectroscopy. *Phys. Rev. B* **2005**, *71* (23), 235420. https://doi.org/10.1103/PhysRevB.71.235420.

(58) Lien, M.-B.; Kim, J.-Y.; Han, M.-G.; Chang, Y.-C.; Chang, Y.-C.; Ferguson, H. J.; Zhu, Y.; Herzing, A. A.; Schotland, J. C.; Kotov, N. A.; et al. Optical Asymmetry and Nonlinear Light Scattering from Colloidal Gold Nanorods. *ACS Nano* **2017**, *11* (6), 5925–5932. https://doi.org/10.1021/acsnano.7b01665.

(59) Jain, P. K.; Huang, X.; El-Sayed, I. H.; El-Sayed, M. A. Noble Metals on the Nanoscale: Optical and Photothermal Properties and Some Applications in Imaging, Sensing, Biology, and Medicine. *Acc. Chem. Res.* **2008**, *41* (12), 1578–1586. https://doi.org/10.1021/ar7002804.

(60) Ali, M. R. K.; Rahman, M. A.; Wu, Y.; Han, T.; Peng, X.; Mackey, M. A.; Wang, D.; Shin, H. J.; Chen, Z. G.; Xiao, H.; et al. Efficacy, Long-Term Toxicity, and Mechanistic Studies of Gold Nanorods Photothermal Therapy of Cancer in Xenograft Mice. *Proc. Natl. Acad. Sci.* **2017**, *114* (15), E3110–E3118. https://doi.org/10.1073/pnas.1619302114.

(61) von Maltzahn, G.; Park, J.-H.; Agrawal, A.; Bandaru, N. K.; Das, S. K.; Sailor, M. J.; Bhatia, S. N. Computationally Guided Photothermal Tumor Therapy Using Long-Circulating Gold Nanorod Antennas. *Cancer Res.* **2009**, *69* (9), 3892 LP – 3900. https://doi.org/10.1158/0008-5472.CAN-08-4242.

(62) Chen, Q.; Chen, Q.; Qi, H.; Ruan, L.; Ren, Y. Experimental Comparison of Photothermal Conversion Efficiency of Gold Nanotriangle and Nanorod in Laser Induced Thermal Therapy. *Nanomaterials*. 2017, p 416. https://doi.org/10.3390/nano7120416.

(63) Neupane, B.; Zhao, L.; Wang, G. Up-Conversion Luminescence of Gold Nanospheres When Excited at Nonsurface Plasmon Resonance Wavelength by a Continuous Wave Laser. *Nano Lett.* **2013**, *13* (9), 4087–4092. https://doi.org/10.1021/nl401505p.

(64) Carattino, A.; Caldarola, M.; Orrit, M. Gold Nanoparticles as Absolute

Nanothermometers. *Nano Lett.* **2018**, *18* (2), 874–880. https://doi.org/10.1021/acs.nanolett.7b04145.

(65) Fu, L.; Liu, Y.; Wang, W.; Wang, M.; Bai, Y.; Chronister, E. L.; Zhen, L.; Yin, Y. A Pressure Sensor Based on the Orientational Dependence of Plasmonic Properties of Gold Nanorods. *Nanoscale* **2015**, *7* (34), 14483–14488. https://doi.org/10.1039/C5NR03450G.

(66) Zhang, L.; Xia, K.; Lu, Z.; Li, G.; Chen, J.; Deng, Y.; Li, S.; Zhou, F.; He, N. Efficient and Facile Synthesis of Gold Nanorods with Finely Tunable Plasmonic Peaks from Visible to Near-IR Range. *Chem. Mater.* **2014**, *26* (5), 1794–1798. https://doi.org/10.1021/cm403109k.

(67) Horstmann, M.; Marso, M.; Fox, A.; Rüders, F.; Hollfelder, M.; Hardtdegen, H.; Kordos, P.; Lüth, H. InP/InGaAs Photodetector Based on a High Electron Mobility Transistor Layer Structure: Its Response at 1.3 Mm Wavelength. *Appl. Phys. Lett.* **1995**, *67* (1), 106–108. https://doi.org/10.1063/1.115497.

(68) Xu, S. J.; Chua, S. J.; Mei, T.; Wang, X. C.; Zhang, X. H.; Karunasiri, G.; Fan, W. J.; Wang, C. H.; Jiang, J.; Wang, S.; et al. Characteristics of InGaAs Quantum Dot Infrared Photodetectors. *Appl. Phys. Lett.* **1998**, *73* (21), 3153–3155. https://doi.org/10.1063/1.122703.

(69) Kimukin, I.; Biyikli, N.; Ozbay, E. InSb High-Speed Photodetectors Grown on GaAs Substrate. *J. Appl. Phys.* **2003**, *94* (8), 5414–5416. https://doi.org/10.1063/1.1611286.

(70) Indrea, E.; Barbu, A. Indirect Photon Interaction in PbS Photodetectors. *Appl. Surf. Sci.* **1996**, *106*, 498–501. https://doi.org/https://doi.org/10.1016/S0169-4332(96)00394-7.

(71) Itsuno, A. M.; Phillips, J. D.; Velicu, S. Mid-Wave Infrared HgCdTe NBn Photodetector. *Appl. Phys. Lett.* **2012**, *100* (16), 161102. https://doi.org/10.1063/1.4704359.

(72) Wang, L.; Li, Y.-F.; Zhou, L.; Liu, Y.; Meng, L.; Zhang, K.; Wu, X.; Zhang, L.; Li, B.; Chen, C. Characterization of Gold Nanorods in Vivo by Integrated Analytical Techniques: Their Uptake, Retention, and Chemical Forms. *Anal. Bioanal. Chem.* **2010**, *396* (3), 1105–1114. https://doi.org/10.1007/s00216-009-3302-y.

(73) Durr, N. J.; Larson, T.; Smith, D. K.; Korgel, B. A.; Sokolov, K.; Ben-Yakar, A. Two-Photon Luminescence Imaging of Cancer Cells Using Molecularly Targeted Gold Nanorods. *Nano Lett.* **2007**, *7* (4), 941–945. https://doi.org/10.1021/nl062962v.

(74) Murphy, C. J.; Gole, A. M.; Stone, J. W.; Sisco, P. N.; Alkilany, A. M.; Goldsmith, E. C.; Baxter, S. C. Gold Nanoparticles in Biology: Beyond Toxicity to Cellular Imaging.

*Acc. Chem. Res.* **2008**, *41* (12), 1721–1730. https://doi.org/10.1021/ar800035u.

(75) Hou, H.; Chen, L.; He, H.; Chen, L.; Zhao, Z.; Jin, Y. Fine-Tuning the LSPR Response of Gold Nanorod–Polyaniline Core–Shell Nanoparticles with High Photothermal Efficiency for Cancer Cell Ablation. *J. Mater. Chem. B* **2015**, *3* (26), 5189–5196. https://doi.org/10.1039/C5TB00556F.

(76) Deng, H.; Zhong, Y.; Du, M.; Liu, Q.; Fan, Z.; Dai, F.; Zhang, X. Theranostic Self-Assembly Structure of Gold Nanoparticles for NIR Photothermal Therapy and X-Ray Computed Tomography Imaging. *Theranostics* **2014**, *4* (9), 904–918. https://doi.org/10.7150/thno.9448.

(77) Dembereldorj, U.; Choi, S. Y.; Ganbold, E.-O.; Song, N. W.; Kim, D.; Choo, J.; Lee, S. Y.; Kim, S.; Joo, S.-W. Gold Nanorod-Assembled PEGylated Graphene-Oxide Nanocomposites for Photothermal Cancer Therapy. *Photochem. Photobiol.* **2014**, *90* (3), 659–666. https://doi.org/10.1111/php.12212.

(78) Wang, S.; Riedinger, A.; Li, H.; Fu, C.; Liu, H.; Li, L.; Liu, T.; Tan, L.; Barthel, M. J.; Pugliese, G.; et al. Plasmonic Copper Sulfide Nanocrystals Exhibiting Near-Infrared Photothermal and Photodynamic Therapeutic Effects. *ACS Nano* **2015**, *9* (2), 1788–1800. https://doi.org/10.1021/nn506687t.

(79) Shibu, E. S.; Varkentina, N.; Cognet, L.; Lounis, B. Small Gold Nanorods with Tunable Absorption for Photothermal Microscopy in Cells. *Adv. Sci.* **2017**, *4* (2), 1600280. https://doi.org/10.1002/advs.201600280.

(80) Niidome, T.; Yamagata, M.; Okamoto, Y.; Akiyama, Y.; Takahashi, H.; Kawano, T.; Katayama, Y.; Niidome, Y. PEG-Modified Gold Nanorods with a Stealth Character for in Vivo Applications. *J. Control. Release* **2006**, *114* (3), 343–347. https://doi.org/https://doi.org/10.1016/j.jconrel.2006.06.017.

(81) Ekici, O.; Harrison, R. K.; Durr, N. J.; Eversole, D. S.; Lee, M.; Ben-Yakar, A. Thermal Analysis of Gold Nanorods Heated with Femtosecond Laser Pulses. *J. Phys. D. Appl. Phys.* **2008**, *41* (18), 185501. https://doi.org/10.1088/0022-3727/41/18/185501.

(82) Baida, H.; Mongin, D.; Christofilos, D.; Bachelier, G.; Crut, A.; Maioli, P.; Del Fatti, N.; Vallée, F. Ultrafast Nonlinear Optical Response of a Single Gold Nanorod near Its Surface Plasmon Resonance. *Phys. Rev. Lett.* **2011**, *107* (5), 57402. https://doi.org/10.1103/PhysRevLett.107.057402.

(83) Zhao, J.; Sun, Y.; Kong, X.; Tian, L.; Wang, Y.; Tu, L.; Zhao, J.; Zhang, H. Controlled Synthesis, Formation Mechanism, and Great Enhancement of Red Upconversion

Luminescence of NaYF4:Yb3+, Er3+ Nanocrystals/Submicroplates at Low Doping Level. *J. Phys. Chem. B* **2008**, *112* (49), 15666–15672. https://doi.org/10.1021/jp805567k.

(84) Huang, X.; Neretina, S.; El-Sayed, M. A. Gold Nanorods: From Synthesis and Properties to Biological and Biomedical Applications. *Adv. Mater.* **2009**, *21* (48), 4880–4910. https://doi.org/10.1002/adma.200802789.

(85) Sau, T. K.; Rogach, A. L.; Jäckel, F.; Klar, T. A.; Feldmann, J. Properties and Applications of Colloidal Nonspherical Noble Metal Nanoparticles. *Adv. Mater.* **2010**, *22* (16), 1805–1825. https://doi.org/10.1002/adma.200902557.

(86) Murphy, C. J.; Thompson, L. B.; Alkilany, A. M.; Sisco, P. N.; Boulos, S. P.; Sivapalan, S. T.; Yang, J. A.; Chernak, D. J.; Huang, J. The Many Faces of Gold Nanorods. *J. Phys. Chem. Lett.* **2010**, *1* (19), 2867–2875. https://doi.org/10.1021/jz100992x.

(87) Long, N. N.; Vu, L. Van; Kiem, C. D.; Doanh, S. C.; Nguyet, C. T.; Hang, P. T.; Thien, N. D.; Quynh, L. M. Synthesis and Optical Properties of Colloidal Gold Nanoparticles. *J. Phys. Conf. Ser.* **2009**, *187* (1), 12026. https://doi.org/10.1088/1742-6596/187/1/012026.

(88) Chang, H.-H.; Murphy, C. J. Mini Gold Nanorods with Tunable Plasmonic Peaks beyond 1000 Nm. *Chem. Mater.* **2018**, *30* (4), 1427–1435. https://doi.org/10.1021/acs.chemmater.7b05310.

(89) Jana, N. R. Gram-Scale Synthesis of Soluble, Near-Monodisperse Gold Nanorods and Other Anisotropic Nanoparticles. *Small* **2005**, *1* (8-9), 875–882. https://doi.org/10.1002/smll.200500014.

(90) Lal, S.; Clare, S. E.; Halas, N. J. Nanoshell-Enabled Photothermal Cancer Therapy: Impending Clinical Impact. *Acc. Chem. Res.* **2008**, *41* (12), 1842–1851. https://doi.org/10.1021/ar800150g.

(91) Skrabalak, S. E.; Chen, J.; Sun, Y.; Lu, X.; Au, L.; Cobley, C. M.; Xia, Y. Gold Nanocages: Synthesis, Properties, and Applications. *Acc. Chem. Res.* **2008**, *41* (12), 1587–1595. https://doi.org/10.1021/ar800018v.

(92) Huang, X.; Jain, P. K.; El-Sayed, I. H.; El-Sayed, M. A. Gold Nanoparticles: Interesting Optical Properties and Recent Applications in Cancer Diagnostics and Therapy. *Nanomedicine* **2007**, *2* (5), 681–693. https://doi.org/10.2217/17435889.2.5.681.

(93) Jain, P. K.; Huang, X.; El-Sayed, I. H.; El-Sayed, M. A. Review of Some Interesting

Surface Plasmon Resonance-Enhanced Properties of Noble Metal Nanoparticles and Their Applications to Biosystems. *Plasmonics* **2007**, *2* (3), 107–118. https://doi.org/10.1007/s11468-007-9031-1.

(94) Huang, X.; Jain, P. K.; El-Sayed, I. H.; El-Sayed, M. A. Plasmonic Photothermal Therapy (PPTT) Using Gold Nanoparticles. *Lasers Med. Sci.* **2007**, *23* (3), 217. https://doi.org/10.1007/s10103-007-0470-x.

(95) Link, S.; El-Sayed, M. A. Optical Properties and Ultrafast Dynamics of Metallic Nanocrystals. *Annu. Rev. Phys. Chem.* **2003**, *54* (1), 331–366. https://doi.org/10.1146/annurev.physchem.54.011002.103759.

(96) Link, S.; El-Sayed, M. A. Shape and Size Dependence of Radiative, Non-Radiative and Photothermal Properties of Gold Nanocrystals. *Int. Rev. Phys. Chem.* **2000**, *19* (3), 409–453. https://doi.org/10.1080/01442350050034180.

(97) Link, S.; El-Sayed, M. A. Spectral Properties and Relaxation Dynamics of Surface Plasmon Electronic Oscillations in Gold and Silver Nanodots and Nanorods. *J. Phys. Chem. B* **1999**, *103* (40), 8410–8426. https://doi.org/10.1021/jp9917648.

(98) Pescaglini, A.; Martín, A.; Cammi, D.; Juska, G.; Ronning, C.; Pelucchi, E.; Iacopino, D. Hot-Electron Injection in Au Nanorod–ZnO Nanowire Hybrid Device for Near-Infrared Photodetection. *Nano Lett.* **2014**, *14* (11), 6202–6209. https://doi.org/10.1021/nl5024854.

(99) Guerrero, A.; Hassan, N.; Escobar, C.; Albericio, F.; Kogan, M.; Araya, E. Gold Nanoparticles for Photothermally Controlled Drug Release. *Nanomedicine* **2014**, *9* (13), 2023–2039. https://doi.org/10.2217/nnm.14.126.

(100) Ma, H.; Bendix, P. M.; Oddershede, L. B. Large-Scale Orientation Dependent Heating from a Single Irradiated Gold Nanorod. *Nano Lett.* **2012**, *12* (8), 3954–3960. https://doi.org/10.1021/nl3010918.

(101) Vásquez Mazzotti, D.; Alvarado, L.; Puga, R.; Loro, H. Calibration of Remote Nanothermometers Using Nanoparticles of NaYF4: Er3+, Yb3+, Nd3+. *J. Phys. Conf. Ser.* **2018**, *1143*, 12023. https://doi.org/10.1088/1742-6596/1143/1/012023.

(102) Balabhadra, S.; Debasu, M. L.; Brites, C. D. S.; Ferreira, R. A. S.; Carlos, L. D. Upconverting Nanoparticles Working As Primary Thermometers In Different Media. *J. Phys. Chem. C* **2017**, *121* (25), 13962–13968. https://doi.org/10.1021/acs.jpcc.7b04827.

(103) Ananias, D.; Paz, F. A. A.; Yufit, D. S.; Carlos, L. D.; Rocha, J. Photoluminescent Thermometer Based on a Phase-Transition Lanthanide Silicate with Unusual Structural

Disorder. *J. Am. Chem. Soc.* **2015**, *137* (8), 3051–3058. https://doi.org/10.1021/ja512745y.

(104) Wang, Z.; Ananias, D.; Carné-Sánchez, A.; Brites, C. D. S.; Imaz, I.; Maspoch, D.; Rocha, J.; Carlos, L. D. Lanthanide–Organic Framework Nanothermometers Prepared by Spray-Drying. *Adv. Funct. Mater.* **2015**, *25* (19), 2824–2830. https://doi.org/10.1002/adfm.201500518.

(105) Brites, C. D. S.; Lima, P. P.; Silva, N. J. O.; Millán, A.; Amaral, V. S.; Palacio, F.; Carlos, L. D. Ratiometric Highly Sensitive Luminescent Nanothermometers Working in the Room Temperature Range. Applications to Heat Propagation in Nanofluids. *Nanoscale* **2013**, *5* (16), 7572–7580. https://doi.org/10.1039/C3NR02335D.

(106) Cadiau, A.; Brites, C. D. S.; Costa, P. M. F. J.; Ferreira, R. A. S.; Rocha, J.; Carlos, L. D. Ratiometric Nanothermometer Based on an Emissive Ln3+-Organic Framework. *ACS Nano* **2013**, *7* (8), 7213–7218. https://doi.org/10.1021/nn402608w.

(107) Lumerical Inc. Https://Www.Lumerical.Com (Accessed September 2018). *Vancouver, BC V6E 2M6*, **2018**, *9*.

(108) Funston, A. M.; Novo, C.; Davis, T. J.; Mulvaney, P. Plasmon Coupling of Gold Nanorods at Short Distances and in Different Geometries. *Nano Lett.* **2009**, *9* (4), 1651–1658. https://doi.org/10.1021/nl900034v.

(109) Ivanova, S.; Pellé, F. Strong 1.53 Mm to NIR-VIS-UV Upconversion in Er-Doped Fluoride Glass for High-Efficiency Solar Cells. *J. Opt. Soc. Am. B* **2009**, *26* (10), 1930–1938. https://doi.org/10.1364/JOSAB.26.001930.

(110) Suyver, J. F.; Aebischer, A.; García-Revilla, S.; Gerner, P.; Güdel, H. U. Anomalous Power Dependence of Sensitized Upconversion Luminescence. *Phys. Rev. B* **2005**, *71* (12), 125123. https://doi.org/10.1103/PhysRevB.71.125123.

(111) Chen, G.; Ohulchanskyy, T. Y.; Kachynski, A.; Ågren, H.; Prasad, P. N. Intense Visible and Near-Infrared Upconversion Photoluminescence in Colloidal LiYF4:Er3+ Nanocrystals under Excitation at 1490 Nm. *ACS Nano* **2011**, *5* (6), 4981–4986. https://doi.org/10.1021/nn201083j.

(112) Brites, C. D. S.; Lima, P. P.; Silva, N. J. O.; Millán, A.; Amaral, V. S.; Palacio, F.; Carlos, L. D. Thermometry at the Nanoscale. *Nanoscale* **2012**, *4* (16), 4799–4829. https://doi.org/10.1039/C2NR30663H.

(113) Huang, Y.; Skripka, A.; Labrador-Páez, L.; Sanz-Rodríguez, F.; Haro-González, P.; Jaque, D.; Rosei, F.; Vetrone, F. Upconverting Nanocomposites with Combined Photothermal and Photodynamic Effects. *Nanoscale* **2018**, *10* (2), 791–799.

https://doi.org/10.1039/C7NR05499H.

(114) Rodríguez-Sevilla, P.; Zhang, Y.; Haro-González, P.; Sanz-Rodríguez, F.; Jaque, F.; Solé, J. G.; Liu, X.; Jaque, D. Thermal Scanning at the Cellular Level by an Optically Trapped Upconverting Fluorescent Particle. *Adv. Mater.* **2016**, *28* (12), 2421–2426. https://doi.org/10.1002/adma.201505020.

(115) Aigouy, L.; Tessier, G.; Mortier, M.; Charlot, B. Scanning Thermal Imaging of Microelectronic Circuits with a Fluorescent Nanoprobe. *Appl. Phys. Lett.* **2005**, *87* (18), 184105. https://doi.org/10.1063/1.2123384.

(116) Brites, C. D. S.; Lima, P. P.; Silva, N. J. O.; Millán, A.; Amaral, V. S.; Palacio, F.; Carlos, L. D. Lanthanide-Based Luminescent Molecular Thermometers. *New J. Chem.* **2011**, *35* (6), 1177–1183. https://doi.org/10.1039/C0NJ01010C.

(117) Vetrone, F.; Naccache, R.; Zamarrón, A.; Juarranz de la Fuente, A.; Sanz-Rodríguez, F.; Martinez Maestro, L.; Martín Rodriguez, E.; Jaque, D.; García Solé, J.; Capobianco, J. A. Temperature Sensing Using Fluorescent Nanothermometers. *ACS Nano* **2010**, *4* (6), 3254–3258. https://doi.org/10.1021/nn100244a.

(118) Wickberg, A.; Mueller, J. B.; Mange, Y. J.; Fischer, J.; Nann, T.; Wegener, M. Three-Dimensional Micro-Printing of Temperature Sensors Based on up-Conversion Luminescence. *Appl. Phys. Lett.* **2015**, *106* (13), 133103. https://doi.org/10.1063/1.4916222.

(119) Aigouy, L.; De Wilde, Y.; Mortier, M.; Giérak, J.; Bourhis, E. Fabrication and Characterization of Fluorescent Rare-Earth-Doped Glass-Particle-Based Tips for near-Field Optical Imaging Applications. *Appl. Opt.* **2004**, *43* (19), 3829–3837. https://doi.org/10.1364/AO.43.003829.

(120) Baffou, G.; Quidant, R.; García de Abajo, F. J. Nanoscale Control of Optical Heating in Complex Plasmonic Systems. *ACS Nano* **2010**, *4* (2), 709–716. https://doi.org/10.1021/nn901144d.

(121) Baffou, G. *Thermoplasmonics: Heating Metal Nanoparticles Using Light*; Cambridge University Press., 2017.

(122) Sarthou, J.; Duquesne, J.-Y.; Becerra, L.; Gredin, P.; Mortier, M. Thermal Conductivity Measurements of Yb:CaF2 Transparent Ceramics Using the 3 ω Method. *J. Appl. Phys.* **2017**, *121* (24), 245108. https://doi.org/10.1063/1.4990282.

(123) Gomès, S.; Assy, A.; Chapuis, P.-O. Scanning Thermal Microscopy: A Review. *Phys. status solidi* **2015**, *212* (3), 477–494. https://doi.org/10.1002/pssa.201400360.

(124) Baffou, G.; Berto, P.; Bermúdez Ureña, E.; Quidant, R.; Monneret, S.; Polleux, J.;

Rigneault, H. Photoinduced Heating of Nanoparticle Arrays. *ACS Nano* **2013**, *7* (8), 6478–6488. https://doi.org/10.1021/nn401924n.

(125) Setoura, K.; Okada, Y.; Werner, D.; Hashimoto, S. Observation of Nanoscale Cooling Effects by Substrates and the Surrounding Media for Single Gold Nanoparticles under CW-Laser Illumination. *ACS Nano* **2013**, *7* (9), 7874–7885. https://doi.org/10.1021/nn402863s.

(126) Govorov, A. O.; Richardson, H. H. Generating Heat with Metal Nanoparticles. *Nano Today* **2007**, *2* (1), 30–38. https://doi.org/https://doi.org/10.1016/S1748-0132(07)70017-8.

(127) Maity, S.; Wu, W.-C.; Xu, C.; Tracy, J. B.; Gundogdu, K.; Bochinski, J. R.; Clarke, L. I. Spatial Temperature Mapping within Polymer Nanocomposites Undergoing Ultrafast Photothermal Heating via Gold Nanorods. *Nanoscale* **2014**, *6* (24), 15236–15247. https://doi.org/10.1039/C4NR05179C.

(128) Nigoghossian, K.; Ouellet, S.; Plain, J.; Messaddeq, Y.; Boudreau, D.; Ribeiro, S. J. L. Upconversion Nanoparticle-Decorated Gold Nanoshells for near-Infrared Induced Heating and Thermometry. *J. Mater. Chem. B* **2017**, *5* (34), 7109–7117. https://doi.org/10.1039/C7TB01621B.

(129) Huang, Y.; Rosei, F.; Vetrone, F. A Single Multifunctional Nanoplatform Based on Upconversion Luminescence and Gold Nanorods. *Nanoscale* **2015**, *7* (12), 5178–5185. https://doi.org/10.1039/C4NR07369J.

(130) Baffou, G.; Kreuzer, M. P.; Kulzer, F.; Quidant, R. Temperature Mapping near Plasmonic Nanostructures Using Fluorescence Polarization Anisotropy. *Opt. Express* **2009**, *17* (5), 3291–3298. https://doi.org/10.1364/OE.17.003291.

(131) Lovell, J. F.; Liu, T. W. B.; Chen, J.; Zheng, G. Activatable Photosensitizers for Imaging and Therapy. *Chem. Rev.* **2010**, *110* (5), 2839–2857. https://doi.org/10.1021/cr900236h.

(132) Chu, S.-W.; Wu, H.-Y.; Huang, Y.-T.; Su, T.-Y.; Lee, H.; Yonemaru, Y.; Yamanaka, M.; Oketani, R.; Kawata, S.; Shoji, S.; et al. Saturation and Reverse Saturation of Scattering in a Single Plasmonic Nanoparticle. *ACS Photonics* **2014**, *1* (1), 32–37. https://doi.org/10.1021/ph4000218.

(133) Elim, H. I.; Yang, J.; Lee, J.-Y.; Mi, J.; Ji, W. Observation of Saturable and Reverse-Saturable Absorption at Longitudinal Surface Plasmon Resonance in Gold Nanorods. *Appl. Phys. Lett.* **2006**, *88* (8), 83107. https://doi.org/10.1063/1.2177366.

(134) Xiang, H.; Niu, T.; Schoenauer Sebag, M.; Hu, Z.; Xu, X.; Billot, L.; Aigouy, L.; Chen,

Z. Short-Wave Infrared Sensor by the Photothermal Effect of Colloidal Gold Nanorods. *Small* **2018**, *14* (16), 1704013. https://doi.org/10.1002/smll.201704013.

(135) FOSTER, G. C. Platinum Resistance-Thermometers. *Nature* **1894**, *50*, 399.

(136) Barber, C. R. Platinum Resistance Thermometers of Small Dimensions. *J. Sci. Instrum.* **1950**, *27* (2), 47–49. https://doi.org/10.1088/0950-7671/27/2/306.

(137) Batagelj, V.; Bojkovski, J.; Drnovšek, J. Methods of Reducing the Uncertainty of the Self-Heating Correction of a Standard Platinum Resistance Thermometer in Temperature Measurements of the Highest Accuracy. *Meas. Sci. Technol.* **2003**, *14* (12), 2151.

(138) Miyakawa, N.; Legner, W.; Ziemann, T.; Telitschkin, D.; Fecht, H.-J.; Friedberger, A. MEMS-Based Microthruster with Integrated Platinum Thin Film Resistance Temperature Detector (RTD), Heater Meander and Thermal Insulation for Operation up to 1,000°C. *Microsyst. Technol.* **2012**, *18* (7), 1077–1087. https://doi.org/10.1007/s00542-012-1441-0.

(139) Kim, K.-J.; Lee, J.-C.; Choe, S.-B.; Shin, K.-H. Joule Heating in Ferromagnetic Nanowires: Prediction and Observation. *Appl. Phys. Lett.* **2008**, *92* (19), 192509. https://doi.org/10.1063/1.2926374.

(140) Aigouy, L.; Lalanne, P.; Hugonin, J. P.; Julié, G.; Mathet, V.; Mortier, M. Near-Field Analysis of Surface Waves Launched at Nanoslit Apertures. *Phys. Rev. Lett.* **2007**, *98* (15), 153902. https://doi.org/10.1103/PhysRevLett.98.153902.

(141) Saïdi, E.; Babinet, N.; Lalouat, L.; Lesueur, J.; Aigouy, L.; Volz, S.; Labéguerie-Egéa, J.; Mortier, M. Tuning Temperature and Size of Hot Spots and Hot-Spot Arrays. *Small* **2011**, *7* (2), 259–264. https://doi.org/10.1002/smll.201001476.

(142) Mukherjee, S.; Libisch, F.; Large, N.; Neumann, O.; Brown, L. V.; Cheng, J.; Lassiter, J. B.; Carter, E. A.; Nordlander, P.; Halas, N. J. Hot Electrons Do the Impossible: Plasmon-Induced Dissociation of H 2 on Au. *Nano Lett.* **2013**, *13* (1), 240–247. https://doi.org/10.1021/nl303940z.

(143) Lee, J.; Mubeen, S.; Ji, X.; Stucky, G. D.; Moskovits, M. Plasmonic Photoanodes for Solar Water Splitting with Visible Light. *Nano Lett.* **2012**, *12* (9), 5014–5019. https://doi.org/10.1021/nl302796f.

(144) Chen, Z. H.; Tang, Y. B.; Liu, C. P.; Leung, Y. H.; Yuan, G. D.; Chen, L. M.; Wang, Y. Q.; Bello, I.; Zapien, J. A.; Zhang, W. J.; et al. Vertically Aligned ZnO Nanorod Arrays Sentisized with Gold Nanoparticles for Schottky Barrier Photovoltaic Cells. *J. Phys. Chem. C* **2009**, *113* (30), 13433–13437. https://doi.org/10.1021/jp903153w.

(145) Hoang, C. V; Hayashi, K.; Ito, Y.; Gorai, N.; Allison, G.; Shi, X.; Sun, Q.; Cheng, Z.; Ueno, K.; Goda, K.; et al. Interplay of Hot Electrons from Localized and Propagating Plasmons. *Nat. Commun.* **2017**, *8* (1), 771. https://doi.org/10.1038/s41467-017-00815-x.

(146) Sobhani, A.; Lauchner, A.; Najmaei, S.; Ayala-Orozco, C.; Wen, F.; Lou, J.; Halas, N. J. Enhancing the Photocurrent and Photoluminescence of Single Crystal Monolayer MoS 2 with Resonant Plasmonic Nanoshells. *Appl. Phys. Lett.* **2014**, *104* (3), 031112. https://doi.org/10.1063/1.4862745.

(147) Sun, Z.; Aigouy, L.; Chen, Z. Plasmonic-Enhanced Perovskite–Graphene Hybrid Photodetectors. *Nanoscale* **2016**, *8* (14), 7377–7383. https://doi.org/10.1039/C5NR08677A.

(148) Pelayo García de Arquer, F.; Beck, F. J.; Bernechea, M.; Konstantatos, G. Plasmonic Light Trapping Leads to Responsivity Increase in Colloidal Quantum Dot Photodetectors. *Appl. Phys. Lett.* **2012**, *100* (4), 043101. https://doi.org/10.1063/1.3678039.

(149) Amann, M.-C.; Bosch, T. M.; Lescure, M.; Myllylae, R. A.; Rioux, M. Laser Ranging: A Critical Review of Unusual Techniques for Distance Measurement. *Opt. Eng.* **2001**, *40* (1), 10–20.

(150) Introduction. In *Computational Photonics: An Introduction with MATLAB*; Wartak, M. S., Ed.; Cambridge University Press: Cambridge, 2013; pp 1–16. https://doi.org/DOI: 10.1017/CBO9780511794247.002.

(151) Myers, M. J.; Myers, J. D.; Sarracino, J. T.; Hardy, C. R.; Guo, B.; Christian, S. M.; Myers, J. A.; Roth, F.; Myers, A. G. LIBS System with Compact Fiber Spectrometer, Head Mounted Spectra Display and Hand Held Eye-Safe Erbium Glass Laser Gun. In *Proc.SPIE*; 2010; Vol. 7578.

(152) Schäfer, H.; Ptacek, P.; Eickmeier, H.; Haase, M. Synthesis of Hexagonal Yb3+,Er3+-Doped NaYF4 Nanocrystals at Low Temperature. *Adv. Funct. Mater.* **2009**, *19*, 3091–3097. https://doi.org/10.1002/adfm.200900642.

(153) Ghosh, P.; Patra, A. Tuning of Crystal Phase and Luminescence Properties of Eu3+ Doped Sodium Yttrium Fluoride Nanocrystals. *J. Phys. Chem. C* **2008**, *112*, 3223–3231. https://doi.org/10.1021/jp7099114.

(154) Wang, F.; Han, Y.; Lim, C. S.; Lu, Y.; Wang, J.; Xu, J.; Chen, H.; Zhang, C.; Hong, M.; Liu, X. Simultaneous Phase and Size Control of Upconversion Nanocrystals through Lanthanide Doping. *Nature* **2010**, *463* (7284), 1061–1065.

https://doi.org/10.1038/nature08777.

(155) Idris, N. M.; Jayakumar, M. K. G.; Bansal, A.; Zhang, Y. Upconversion Nanoparticles as Versatile Light Nanotransducers for Photoactivation Applications. *Chem. Soc. Rev.* **2015**, *44* (6), 1449–1478. https://doi.org/10.1039/C4CS00158C.

(156) Sedlmeier, A.; Gorris, H. H. Surface Modification and Characterization of Photon-Upconverting Nanoparticles for Bioanalytical Applications. *Chem. Soc. Rev.* **2015**, *44* (6), 1526–1560. https://doi.org/10.1039/c4cs00186a.

(157) Wang, F.; Banerjee, D.; Liu, Y.; Chen, X.; Liu, X. Upconversion Nanoparticles in Biological Labeling, Imaging, and Therapy. *Analyst* **2010**, *135* (8), 1839–1854. https://doi.org/10.1039/c0an00144a.

(158) Webster, J. G.; Kazemi, A.; Zamiri, M.; Kim, J. O.; Schuler-Sandy, T.; Krishna, S. Colloidal and Epitaxial Quantum Dot Infrared Photodetectors: Growth, Performance, and Comparison. *Wiley Encycl. Electr. Electron. Eng.* **2014**, No. September 2014, 1–26. https://doi.org/10.1002/047134608x.w8225.

(159) Xiang, H.; Lin, H.-J.; Niu, T.; Chen, Z.; Aigouy, L. Nanoscale Thermal Characterization of High Aspect Ratio Gold Nanorods for Photothermal Applications at $\lambda = 1.5$ $\mu$ M. *J. Appl. Phys.* **2019**, *125* (16), 163101. https://doi.org/10.1063/1.5088944.

(160) Van Der Ende, B. M.; Aarts, L.; Meijerink, A. Lanthanide Ions as Spectral Converters for Solar Cells. *Phys. Chem. Chem. Phys.* **2009**, *11* (47), 11081–11095. https://doi.org/10.1039/b913877c.

(161) Goldschmidt, J. C.; Fischer, S. Upconversion for Photovoltaics – a Review of Materials, Devices and Concepts for Performance Enhancement. *Adv. Opt. Mater.* **2015**, *3* (4), 510–535. https://doi.org/10.1002/adom.201500024.

(162) Schoenauer Sebag, M.; Hu, Z.; de Oliveira Lima, K.; Xiang, H.; Gredin, P.; Mortier, M.; Billot, L.; Aigouy, L.; Chen, Z. Microscopic Evidence of Upconversion-Induced Near-Infrared Light Harvest in Hybrid Perovskite Solar Cells. *ACS Appl. Energy Mater.* **2018**, *1* (8), 3537–3543. https://doi.org/10.1021/acsaem.8b00518.

(163) Yu, J.; Yang, Y.; Fan, R.; Liu, D.; Wei, L.; Chen, S.; Li, L.; Yang, B.; Cao, W. Enhanced Near-Infrared to Visible Upconversion Nanoparticles of Ho(3)(+)-Yb(3)(+)-F(-) Tri-Doped TiO(2) and Its Application in Dye-Sensitized Solar Cells with 37% Improvement in Power Conversion Efficiency. *Inorg Chem* **2014**, *53*, 8045–8053. https://doi.org/10.1021/ic501041h.

(164) Kataria, M.; Yadav, K.; Haider, G.; Liao, Y. M.; Liou, Y. R.; Cai, S. Y.; Lin, H. I.;

Chen, Y. H.; Paul Inbaraj, C. R.; Bera, K. P.; et al. Transparent, Wearable, Broadband, and Highly Sensitive Upconversion Nanoparticles and Graphene-Based Hybrid Photodetectors. *ACS Photonics* **2018**, *5* (6), 2336–2347. https://doi.org/10.1021/acsphotonics.8b00141.

(165) Zhao, X.; Song, L.; Zhao, R.; Tan, M. C. High-Performance and Flexible Shortwave Infrared Photodetectors Using Composites of Rare Earth-Doped Nanoparticles. *ACS Appl. Mater. Interfaces* **2019**, *11* (2), 2344–2351. https://doi.org/10.1021/acsami.8b16978.

(166) Wu, J.; Yang, Z.; Qiu, C.; Zhang, Y.; Wu, Z.; Yang, J.; Lu, Y.; Li, J.; Yang, D.; Hao, R.; et al. Enhanced Performance of a Graphene/GaAs Self-Driven near-Infrared Photodetector with Upconversion Nanoparticles. *Nanoscale* **2018**, *10* (17), 8023–8030. https://doi.org/10.1039/c8nr00594j.

(167) Fu, Y.; Qi, Z.; Xu, X.; Li, L.; Wang, X.; Zhu, X.; Zhuang, X.; Pan, A. Near-Infrared Photodetection Based on Erbium Chloride Borate Nanobelts. *Appl. Phys. Express* **2019**, *12* (3), 035001. https://doi.org/10.7567/1882-0786/ab00e3.

(168) Zhang, X.; Yang, S.; Zhou, H.; Liang, J.; Liu, H.; Xia, H.; Zhu, X.; Jiang, Y.; Zhang, Q.; Hu, W.; et al. Perovskite–Erbium Silicate Nanosheet Hybrid Waveguide Photodetectors at the Near-Infrared Telecommunication Band. *Adv. Mater.* **2017**, *29* (21), 1604431. https://doi.org/10.1002/adma.201604431.

(169) Ma, L.; Hu, W.; Zhang, Q.; Ren, P.; Zhuang, X.; Zhou, H.; Xu, J.; Li, H.; Shan, Z.; Wang, X.; et al. Room-Temperature Near-Infrared Photodetectors Based on Single Heterojunction Nanowires. *Nano Lett.* **2014**, *14* (2), 694–698. https://doi.org/10.1021/nl403951f.

(170) Wang, X.; Wang, P.; Wang, J.; Hu, W.; Zhou, X.; Guo, N.; Huang, H.; Sun, S.; Shen, H.; Lin, T.; et al. Ultrasensitive and Broadband MoS 2 Photodetector Driven by Ferroelectrics. *Adv. Mater.* **2015**, *27* (42), 6575–6581. https://doi.org/10.1002/adma.201503340.

(171) Liu, W.; Lee, J.-S.; Talapin, D. V. III–V Nanocrystals Capped with Molecular Metal Chalcogenide Ligands: High Electron Mobility and Ambipolar Photoresponse. *J. Am. Chem. Soc.* **2013**, *135* (4), 1349–1357. https://doi.org/10.1021/ja308200f.

(172) Tan, H.; Fan, C.; Ma, L.; Zhang, X.; Fan, P.; Yang, Y.; Hu, W.; Zhou, H.; Zhuang, X.; Zhu, X.; et al. Single-Crystalline InGaAs Nanowires for Room-Temperature High-Performance Near-Infrared Photodetectors. *Nano-Micro Lett.* **2016**, *8* (1), 29–35. https://doi.org/10.1007/s40820-015-0058-0.

(173) Bronstein, H.; Chen, Z.; Ashraf, R. S.; Zhang, W.; Du, J.; Durrant, J. R.; Shakya Tuladhar, P.; Song, K.; Watkins, S. E.; Geerts, Y.; et al. Thieno[3,2-b]Thiophene-Diketopyrrolopyrrole-Containing Polymers for High-Performance Organic Field-Effect Transistors and Organic Photovoltaic Devices. *J. Am. Chem. Soc.* **2011**, *133* (10), 3272–3275. https://doi.org/10.1021/ja110619k.

(174) Liu, D.; Jing, Y.; Wang, K.; Wang, Y.; Luo, G. Reaction Study of α-Phase NaYF 4 :Yb,Er Generation via a Tubular Microreactor: Discovery of an Efficient Synthesis Strategy. *Nanoscale* **2019**, *11* (17), 8363–8371. https://doi.org/10.1039/c8nr09957j.

(175) Ivaturi, A.; Macdougall, S. K. W.; Martín-Rodríguez, R.; Quintanilla, M.; Marques-Hueso, J.; Krämer, K. W.; Meijerink, A.; Richards, B. S. Optimizing Infrared to near Infrared Upconversion Quantum Yield of β-NaYF 4 :Er 3+ in Fluoropolymer Matrix for Photovoltaic Devices. *J. Appl. Phys.* **2013**, *114* (1), 013505. https://doi.org/10.1063/1.4812578.

(176) Faulkner, D. O.; Mcdowell, J. J.; Price, A. J.; Perovic, D. D.; Kherani, N. P.; Ozin, G. A. Measurement of Absolute Photoluminescence Quantum Yields Using Integrating Spheres - Which Way to Go? *Laser Photonics Rev.* **2012**, *6* (6), 802–806. https://doi.org/10.1002/lpor.201200077.

(177) Bronstein, H.; Collado-Fregoso, E.; Hadipour, A.; Soon, Y. W.; Huang, Z.; Dimitrov, S. D.; Ashraf, R. S.; Rand, B. P.; Watkins, S. E.; Tuladhar, P. S.; et al. Thieno[3,2-b]Thiophene-Diketopyrrolopyrrole Containing Polymers for Inverted Solar Cells Devices with High Short Circuit Currents. *Adv. Funct. Mater.* **2013**, *23* (45), 5647–5654. https://doi.org/10.1002/adfm.201300287.

(178) Guo, X.; Zhou, N.; Lou, S. J.; Smith, J.; Tice, D. B.; Hennek, J. W.; Ortiz, R. P.; Navarrete, J. T. L.; Li, S.; Strzalka, J.; et al. Polymer Solar Cells with Enhanced Fill Factors. *Nat. Photonics* **2013**, *7* (10), 825. https://doi.org/10.1038/nphoton.2013.207.

(179) Nguyen, T. L.; Choi, H.; Ko, S. J.; Uddin, M. A.; Walker, B.; Yum, S.; Jeong, J. E.; Yun, M. H.; Shin, T. J.; Hwang, S.; et al. Semi-Crystalline Photovoltaic Polymers with Efficiency Exceeding 9% in a ∼300 Nm Thick Conventional Single-Cell Device. *Energy Environ. Sci.* **2014**, *7* (9), 3040–3051. https://doi.org/10.1039/c4ee01529k.

(180) Li, W.; Roelofs, W. S. C.; Wienk, M. M.; Janssen, R. A. J. Enhancing the Photocurrent in Diketopyrrolopyrrole-Based Polymer Solar Cells via Energy Level Control. *J. Am. Chem. Soc.* **2012**, *134* (33), 13787–13795. https://doi.org/10.1021/ja305358z.

(181) Huang, B.; Dong, H.; Wong, K.-L.; Sun, L.-D.; Yan, C.-H. Fundamental View of Electronic Structures of β-NaYF4, β-NaGdF4, and β-NaLuF4. *J. Phys. Chem. C* **2016**,

*120*, 18858–18870. https://doi.org/10.1021/acs.jpcc.6b05261.

(182) Zhang, B. Y.; Liu, T.; Meng, B.; Li, X.; Liang, G.; Hu, X.; Wang, Q. J. Broadband High Photoresponse from Pure Monolayer Graphene Photodetector. *Nat. Commun.* **2013**, *4* (May), 1811. https://doi.org/10.1038/ncomms2830.

(183) Chen, Z.; Li, X.; Wang, J.; Tao, L.; Long, M.; Liang, S. J.; Ang, L. K.; Shu, C.; Tsang, H. K.; Xu, J. Bin. Synergistic Effects of Plasmonics and Electron Trapping in Graphene Short-Wave Infrared Photodetectors with Ultrahigh Responsivity. *ACS Nano* **2017**, *11* (1), 430–437. https://doi.org/10.1021/acsnano.6b06172.

(184) Konstantatos, G.; Badioli, M.; Gaudreau, L.; Osmond, J.; Bernechea, M.; de Arquer, F. P. G.; Gatti, F.; Koppens, F. H. L. Hybrid Graphene–Quantum Dot Phototransistors with Ultrahigh Gain. *Nat. Nanotechnol.* **2012**, *7* (6), 363–368. https://doi.org/10.1038/nnano.2012.60.

(185) Na, J.; Park, K.; Kim, J. T.; Choi, W. K.; Song, Y. W. Air-Stable Few-Layer Black Phosphorus Phototransistor for near-Infrared Detection. *Nanotechnology* **2017**, *28* (8), 085201. https://doi.org/10.1088/1361-6528/aa55e4.

(186) Xie, Y.; Zhang, B.; Wang, S.; Wang, D.; Wang, A.; Wang, Z.; Yu, H.; Zhang, H.; Chen, Y.; Zhao, M.; et al. Ultrabroadband MoS 2 Photodetector with Spectral Response from 445 to 2717 Nm. *Adv. Mater.* **2017**, *29* (17), 1605972. https://doi.org/10.1002/adma.201605972.

(187) Sobhani, A.; Knight, M. W.; Wang, Y.; Zheng, B.; King, N. S.; Brown, L. V; Fang, Z.; Nordlander, P.; Halas, N. J. Narrowband Photodetection in the Near-Infrared with a Plasmon-Induced Hot Electron Device. *Nat. Commun.* **2013**, *4*, 1643.

(188) Dias, S.; Kumawat, K.; Biswas, S.; Krupanidhi, S. B. Solvothermal Synthesis of Cu 2 SnS 3 Quantum Dots and Their Application in Near-Infrared Photodetectors. *Inorg. Chem.* **2017**, *56* (4), 2198–2203. https://doi.org/10.1021/acs.inorgchem.6b02832.

(189) Rauch, T.; Böberl, M.; Tedde, S. F.; Fürst, J.; Kovalenko, M. V.; Hesser, G.; Lemmer, U.; Heiss, W.; Hayden, O. Near-Infrared Imaging with Quantum-Dot-Sensitized Organic Photodiodes. *Nat. Photonics* **2009**, *3* (6), 332–336. https://doi.org/10.1038/nphoton.2009.72.

(190) Clifford, J. P.; Konstantatos, G.; Johnston, K. W.; Hoogland, S.; Levina, L.; Sargent, E. H. Fast, Sensitive and Spectrally Tuneable Colloidal-Quantum-Dot Photodetectors. *Nat. Nanotechnol.* **2009**, *4* (1), 40–44. https://doi.org/10.1038/nnano.2008.313.

(191) Sun, T.; Wang, Y.; Yu, W.; Wang, Y.; Dai, Z.; Liu, Z.; Shivananju, B. N.; Zhang, Y.; Fu, K.; Shabbir, B.; et al. Flexible Broadband Graphene Photodetectors Enhanced by

Plasmonic Cu3−xP Colloidal Nanocrystals. *Small* **2017**, *13* (42), 1–9. https://doi.org/10.1002/smll.201701881.

(192) Li, Y.; Meng, L.; Yang, Y.; Xu, G.; Hong, Z.; Chen, Q.; You, J.; Li, G.; Yang, Y.; Li, Y. High-Efficiency Robust Perovskite Solar Cells on Ultrathin Flexible Substrates. *Nat. Commun.* **2016**, *7*, 10214. https://doi.org/10.1038/ncomms10214.

(193) Gerardo, C. D.; Cretu, E.; Rohling, R. Fabrication of Circuits on Flexible Substrates Using Conductive SU-8 for Sensing Applications. *Sensors (Switzerland)* **2017**, *17* (6), 1420. https://doi.org/10.3390/s17061420.